Royal College of Surgeons in Ireland

repository@rcsi.com

Modelling Metastasis in Neuroblastoma: 3D Culture Assays of Local Tumour Invasion

AUTHOR(S)

Cian Gavin

CITATION

Gavin, Cian (2022): Modelling Metastasis in Neuroblastoma: 3D Culture Assays of Local Tumour Invasion. Royal College of Surgeons in Ireland. Thesis. https://doi.org/10.25419/rcsi.13050401.v1

DOI

10.25419/rcsi.13050401.v1

LICENCE

CC BY 4.0

This work is made available under the above open licence by RCSI and has been printed from https://repository.rcsi.com. For more information please contact repository@rcsi.com

URL

https://repository.rcsi.com/articles/thesis/Modelling_Metastasis_in_Neuroblastoma_3D_Culture_Assays_of_Local_Tumour_Invasion/13050401/1

RCSI UNIVERSITY OF MEDICINE AND HEALTH SCIENCES

Modelling Metastasis in Neuroblastoma: 3D Culture Assays of Local Tumour Invasion

Cian Gavin
Department of Anatomy and Regenerative Medicine

A thesis submitted to the School of Postgraduate Studies, Faculty of Medicine and Health Sciences, RCSI University of Medicine and Health Sciences, in fulfilment of the degree Master of Science (MSc)

Supervisors: Dr Olga Piskareva
Dr Ciara Murphy

2020

I declare that this thesis, which I submit to RCSI for examination in consideration of the award of a higher degree Master of Science (MSc) is my own personal effort. Where any of the content presented is the result of input or data from a related collaborative research programme this is duly acknowledged in the text such that it is possible to ascertain how much of the work is my own. I have not already obtained a degree in RCSI or elsewhere on the basis of this work. Furthermore, I took reasonable care to ensure that the work is original, and, to the best of my knowledge, does not breach copyright law, and has not been taken from other sources except where such work has been cited and acknowledged within the text.

Signed Cian Gavin

Scholar Number 19104260

Date 29.09.2020

Table of Contents

List of Figures

List of Tables

Standard Abbreviations

ALK	Anaplastic lymphoma kinase
bFGF	Basic fibroblast growth factor
BM	Basement membrane
BME	Basement membrane extract
BMPs	Bone morphogenetic proteins
BSA	Bovine serum albumin
C	Collagen type I
CI	Confidence interval
CLX	Cell line xenograft
DIC	Differential interference contrast
DMEM	Dulbecco's Modified Eagle's medium
ECM	Extracellular Matrix
EHD	Ethidium Homodimer
EMT	Epithelial-mesenchymal transition
EtOH	Ethanol
FBS	Fetal bovine serum
GF	Growth factor
ITH	Intra tumour heterogeneity
M	Growth Factor Reduced Matrigel®
MC	Growth factor reduced Matrigel:Collagen type I (1:1)
MCYN-OFF	MYCN transcription OFF
MMPs	Matrix metalloproteinases
MNA	MYCN amplified
MYCN-ON	MYCN transcription ON
NB	Neuroblastoma
NC	Neural crest
NCC	Neural crest cells
NSE	Neuron specific enolase
PBS	Phosphate buffered saline
PDX	Patient-derived xenograft
PHOX-2B	paired-like homeobox 2B
SA	Sympathoadrenal
TBS	Tris buffered saline
TBS-T	Tris buffered saline-Tween
TERT	Telomerase
TME	Tumour microenvironment
WT	Wild type

Acknowledgements

I would like to thank Dr Olga Piskareva for the opportunity to join her research group and for her continuous support and guidance throughout my project. I would also like to thank her for trusting me with the data she gathered while on her fullbright fellowship in Professor Ewald's research group at Johns Hopkins School of Medicine.

I am also grateful to Dr Brenton Cavanagh for his assistance and training in image processing.

I would like to thank John, Tom, Ciara, Catherine and Roisin from the cancer bioengineering research group for their support and encouragement.

The project was supported by the Fulbright-HRB Health Impact Scholar Award and Science Foundation Ireland (SFI/18/TIDA/6003).

Summary

Neuroblastoma (NB) is a highly heterogenous paediatric malignancy of the developing sympathetic nervous system. Approximately half of patients have metastatic disease at the time of diagnosis, coinciding with a survival rate of less than 50%. Therefore, elucidating the molecular basis of the metastatic process may guide novel strategies for drug discovery and therapy. With this in mind, we aimed to explore the invasion of NB in an *ex vivo* culture system. To this end, we isolated NB organoids from patient-derived xenografts (PDXs) and embedded them in 3D extracellular matrix (ECM) hydrogels. We also cultured clonal clusters of NB cell lines as well as organoids isolated from cell line xenografts to compare their behaviour to that of PDX organoids. We used 3D culture assays to directly observe local invasion under different microenvironmental conditions in high-resolution and real-time. We found that the invasion of NB organoids was dependent on the composition of the matrix, where Matrigel was the preferred substratum. Based on organoid morphologies, we have identified and characterised four distinct invasive phenotypes used by NB cells to overcome environmental challenges. Culturing organoids in medium supplemented with FBS and bFGF induced the most aggressive cellular behaviour and the widest range of phenotypes. Unlike organoids isolated from PDXs, we found that NB cell lines were phenotypically confined during ECM invasion and while organoids isolated from cell line xenografts displayed a broader range of phenotypes compared to clonal cell line clusters, they could not recapitulate the diversity seen in PDX organoids. We also used 3D invasion assays to show that repression of the prognostic marker *MYCN,* resulted in less aggressive cellular behaviour in a NB cell line. Overall, we propose the pairing of PDX organoid culture and 3D invasion assays as a valuable tool to discover the molecular mechanisms controlling local invasion in NB.

1.Introduction

1.1 Neuroblastoma: an overview

In both adults and children, cancer is among the most common causes of mortality (1, 2). That being said, malignancies are rare in the paediatric population and in terms of characteristics such as aetiology, biology, response to treatment and outcome, they differ vastly to cancers that are found in adults. This contrast is particularly evident in neuroblastoma (NB); a cancer of the developing sympathetic nervous system that is almost exclusively (90% of cases) diagnosed in children under the age of five (3). NB is the most common solid extracranial tumour in children and is characterised by a remarkable heterogeneity that is both biologically and clinically unique. The outcome of NB ranges drastically from spontaneous regression with little or no treatment to multi drug-resistant, metastatic disease.

Prognosis for a proportion of NB patients has greatly improved over the past 50 years, largely as a result of more accurate treatment stratification. Children with NB are now classified as either low-, intermediate-, or high-risk based on a range of prognostic factors including age at diagnosis, tumour grade, cytogenetics and tumour histopathology (Table 1.1). While 5-year survival rates for patients with low- and intermediate-risk NB are extremely promising, greater than 95% and between 90 and 95% respectively, treatment of high-risk patients is still a challenge, resulting in a 5-year survival rate of less than 50% (4, 5). Current treatment strategies for this cohort of patients are rigorous, involving a combination of surgery, chemotherapy, radiation therapy, retinoic acid, immunotherapy and autologous stem cell rescue (6). Despite this intensive multimodal treatment regime, 50-60% of high-risk patients will relapse and in approximately 80% of these cases relapse occurs within two years of diagnosis (7). Quality of life is therefore drastically reduced for these young patients who undergo long lasting treatment programmes. Furthermore, children that survive this intensive treatment are left at risk of therapy-related morbidities in later life (8), highlighting the need for further research into alternative treatments.

In terms of embryonal cancers, NB is the most common in Europe and has the worst 5-year relative survival rate. The overall cure rate for embryonal malignancies in Europe is approximately 80%, however for NB this drops below 70% (9). This disparity is primarily due to the fact that more than half of patients will present with metastatic disease at the time of diagnosis and are hence classified as high-risk. The most common metastatic sites being bone marrow (70.5%), bone (55.7%), liver (29.6%), intracranial and orbital locations (18.2%), lung (3.3%) and the central nervous system (0.6%) respectively (10). Therefore, elucidating the molecular basis of this metastatic process may guide novel strategies for drug discovery and more effective treatment.

Table 1.1. The International Neuroblastoma Risk Group (INRG) Classification System (11, 12).

INRG Stage	Age (months)	Histologic Category	Grade of Tumor Differentiation	*MYCN*	11q Aberration	Ploidy	Pretreatment Risk Group
L1/L2		GN maturing; GNB intermixed					A Very low
L1		Any, except GN maturing or GNB intermixed		NA			B Very low
				Amp			K High
L2	< 18	Any, except GN maturing or GNB intermixed		NA	No		D Low
					Yes		G Intermediate
	≥ 18	GNB nodular; neuroblastoma	Differentiating	NA	No		E Low
					Yes		H Intermediate
			Poorly differentiated or undifferentiated	NA			
				Amp			N High
M	< 18			NA		Hyperdiploid	F Low
	< 12			NA		Diploid	I Intermediate
	12 to < 18			NA		Diploid	J Intermediate
	< 18			Amp			O High
	≥ 18						P High
MS	< 18			NA	No		C Very low
					Yes		Q High
				Amp			R High

L1; localised tumour that does not involve vital structures (based on image-defined risk factors) confined to one body compartment. L2; locoregional tumour with one or more image-defined risk-factors present. M; distant metastatic site (except stage MS). MS; children <18months with metastatic disease confined to skin, bone marrow and/or liver. Details of INRG staging described in (12). 5-year event free survival (EFS) rates for each risk group are as follows, very low risk; >85%, low risk; > 75 to ≤ 85, intermediate risk; ≥ 50 ≤ 75, high-risk < 50. Blank field = "any", GN = ganglioneuroma, GNB = ganglioneuroblastoma, Amp = amplified, NA = non amplified. Image taken from (11).

1.2 The origin of neuroblastoma

NB is a malignancy that is thought to occur as a result of aberrant development of the autonomic nervous system. Specifically, sympathoadrenal (SA) precursors derived from neural crest cells (NCCs) are widely accepted as the cells of origin. There is a plethora of evidence to support this (reviewed in (13)), including the fact that the majority of primary NBs are either located in the adrenal medulla or along the sympathetic chain (14). NCCs undergo an epithelial to mesenchymal transition (EMT), delaminate from the dorsal neural tube, migrate long distances in the embryo and differentiate into a variety of different cell types. Trunk NCCs specifically, give rise to the sympathetic ganglia, sensory ganglia, chromaffin cells of the adrenal medulla, as well as melanocytes. SA progenitor cells are a distinct population of trunk NCCs that arise between somite pairs 18 to 24 and migrate ventrally to colonise specific sites around the dorsal aorta (DA). These cells acquire a neuronal fate and begin to express neuronal markers such as neuron specific enolase (NSE) and peripherin as well as enzymes required to produce noradrenaline, namely tyrosine hydroxylase and dopamine beta hydroxylase (15, 16). These autonomic neuronal precursors subsequently diverge into sympathetic ganglia or adrenal medulla lineages in response to signals from the DA, particularly bone morphogenetic proteins (BMPs)(17, 18). (Figure 1.2)

NC development is temporally controlled throughout embryogenesis by signalling molecules such as BMP, FGF, Notch, retinoic acid and Wnt. First, the induction of NC development triggers the expression of a group of transcription factors known as border specifier genes (Msx1, Msx2, Pax3, Pax7 and Zic1). Together with signalling molecules these transcription factors regulate the expression of NC specifier genes (AP-2, FoxD3, Snail2, Sox9 and Sox10) which in turn modulate the expression of NC effector genes (Sox9, Sox10, Cad7, Col IIa, Ngn1 etc.) that are responsible for NCC migration and differentiation (19). Many of these genes are implicated in NB pathogenesis providing further evidence for SA NCCs as the cells of origin (reviewed in(20)). For instance, the NC specifier gene and potential tumour suppressor; Forkhead box D3 (FOXD3) is downregulated in NB (21). Low expression levels of the transcription factor AP-2 in NB are associated with poor prognostic markers and adverse patient outcome (22) and downregulation of the border specifier gene PAX3 in NB cells inhibits cell growth and migration (23).

Amplification of the *MYCN* oncogene, present in approximately 50% of high-risk tumours, is the most common genetic alteration in NB and correlates with more aggressive disease and worse outcome (24). During normal sympathoadrenal development, MYCN is expressed at high levels in the early post-migratory neural crest and plays a key role in regulating ventral migration, maintenance of a proliferative capacity and neuronal differentiation (25). In migrating murine NCCs, targeted overexpression of MYCN under the tyrosine hydroxylase (TH) promoter results in spontaneous tumours that closely resemble human NB (26). This transgenic mouse model, known as TH-*MYCN*, provides evidence for *MYCN* as a developmental driver of NB tumorigenesis. Furthermore, primary mouse NCCs can be transformed to recapitulate human NB when engineered to overexpress MYCN (27). Therefore, continuous overexpression of MYCN in the neural crest is sufficient for NB development.

NB generally occurs sporadically, however in 1-2% of cases mutations are inherited. Most hereditary cases (~90%) have activating mutations in anaplastic lymphoma kinase (*ALK*); a receptor tyrosine kinase that is specifically expressed during the development of the nervous system (28). Most of the remaining hereditary cases of NB (~10%) have mutations in the paired-like homeobox 2B (*PHOX2B*) gene. Somatic mutations in *ALK* are also seen in about 8% of sporadic NBs and are negatively associated with prognosis (29). ALK is also involved during NC development, where it promotes migration of NCCs through tyrosine phosphorylation of glycogen synthase kinase 3 beta (GSK-3β) (30). Sporadic mutations in the *PHOX2B* gene are rare, however they do occur in a small number of NB cases (1-2%)(31). PHOX2B controls the expression of genes that encode for noradrenaline-producing enzymes and hence is crucial for the differentiation of sympathoadrenal precursors (32). Interestingly, both MYCN (33) and PHOX2B (34) are regulators of *ALK* transcription in NB, providing a link between these important prognostic factors.

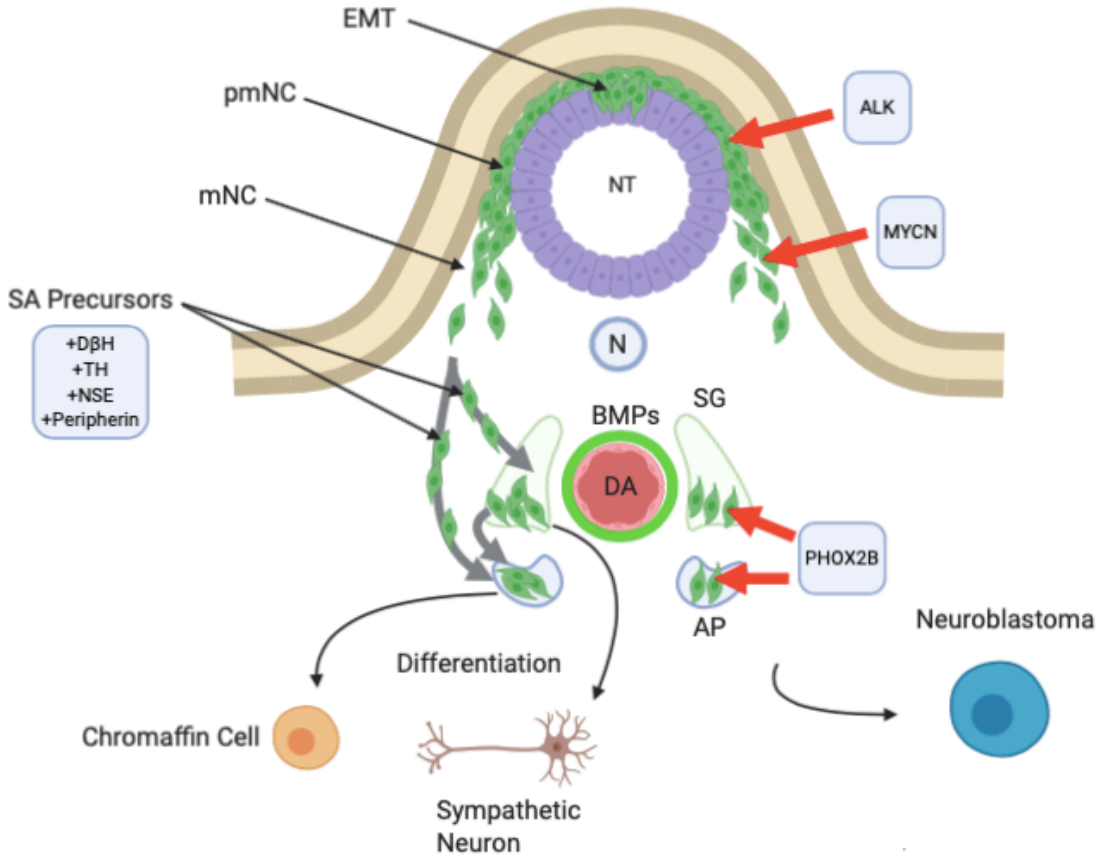

Figure 1.2 The developmental origin of neuroblastoma. During normal development, cells of the neural tube undergo an EMT (pre-migratory NC) and delaminate (migratory NC). Sympathoadrenal precursors begin to express neuronal markers and migrate as a group toward the dorsal aorta in response to environmental stimuli (BMPs). NCCs populate the sympathetic ganglion and adrenal primordia and differentiate to become sympathetic neurons and chromaffin cells respectively. Genomic insults (red arrows) can occur at any stage during this developmental process and result in aberrant migration and differentiation, and death resistance, leading to neuroblastoma development. SA; sympathoadrenal, SG; sympathetic ganglion, DA; dorsal aorta, NC; neural crest, pm; pre-migratory, N; notochord, NT; neural tube, DβH; Dopamine-β-Hydroxylase, TH; Tyrosine hydroxylase, NSE; Neuron specific-enolase

1.3 Metastasis

Metastasis, the process by which cancer cells disseminate from the primary tumour and colonise distant sites, is responsible for an estimated 90% of cancer-related deaths (35, 36). While it is clinically related to late-stage disease, when and how the spread of cancer occurs is not known. In 1889 Stephen Paget suggested that the metastasis of cancer cells was not random and that certain tumour cells would only form secondary neoplasms in a favourable microenvironment (37). This is known as the 'seed and soil' hypothesis, whereby cancer cells act as seeds and the host microenvironment represents the soil. This theory was challenged by Ewing in 1919 who suggested that the location of metastatic sites was purely determined by the anatomy of the lymphatic and circulatory systems (38). It wasn't until the 1970s that Fidler confirmed Paget's theory by demonstrating that metastatic colonisation could only be successful in certain organ locations (39, 40). That being said, Ewing's theory still warrants merit as the circulation is extremely important for the establishment of metastases. However, recent evidence suggests that the unique microenvironment found in each organ is primarily responsible for the specificity of the metastatic process. Tropism toward a particular organ occurs when cancer cells display the ability to adapt to, or evolve fitness toward, a specific microenvironment (41). This non-random distribution of metastatic sites is referred to as "organotropism" and is evident in NB which preferentially metastasises to the bone marrow and bone (6). In more recent years the 'metastatic niche model' has been proposed and is an expansion of Paget's theory. The metastatic niche is proposed as a location that has been primed to facilitate and support tumour cells once they extravasate. The priming of these distant sites is known as pre-metastatic niche formation and relies on primary-tumour secreted factors, tumour-mobilised bone marrow derived cells and the stromal environment of the receptive site. Together these components promote secondary tumour growth by enabling anchorage, providing pro-survival signals, increasing angiogenesis and lymphangiogenesis and providing protection from immune cell detection, induced differentiation and therapy-induced apoptosis (42, 43).

Thus, the dissemination of malignant cells from the primary tumour and subsequent colonization of distant tissues is a heterogenous multistep process (Figure 1.3). The metastatic cascade begins when cancer cells penetrate the basement membrane (BM),

invade their surrounding stroma and disseminate from the primary tumour mass [Step 1]. Once free these cells enter the circulation by intravasation or through the lymphatic system [Step 2]. Tumour cells then must survive shear and oxidative stress and avoid immune detection in the blood stream [Step 3] until they become trapped in a capillary bed and extravasate [Step 4]. Once they have reached their destination, disseminated cancer cells colonize supportive niches to form secondary tumours [Step 5]. The complexity of the metastatic cascade means that it is impossible to model in its entirety, hence for the purpose of this study we aimed to model only the first step of this process; local tumour invasion.

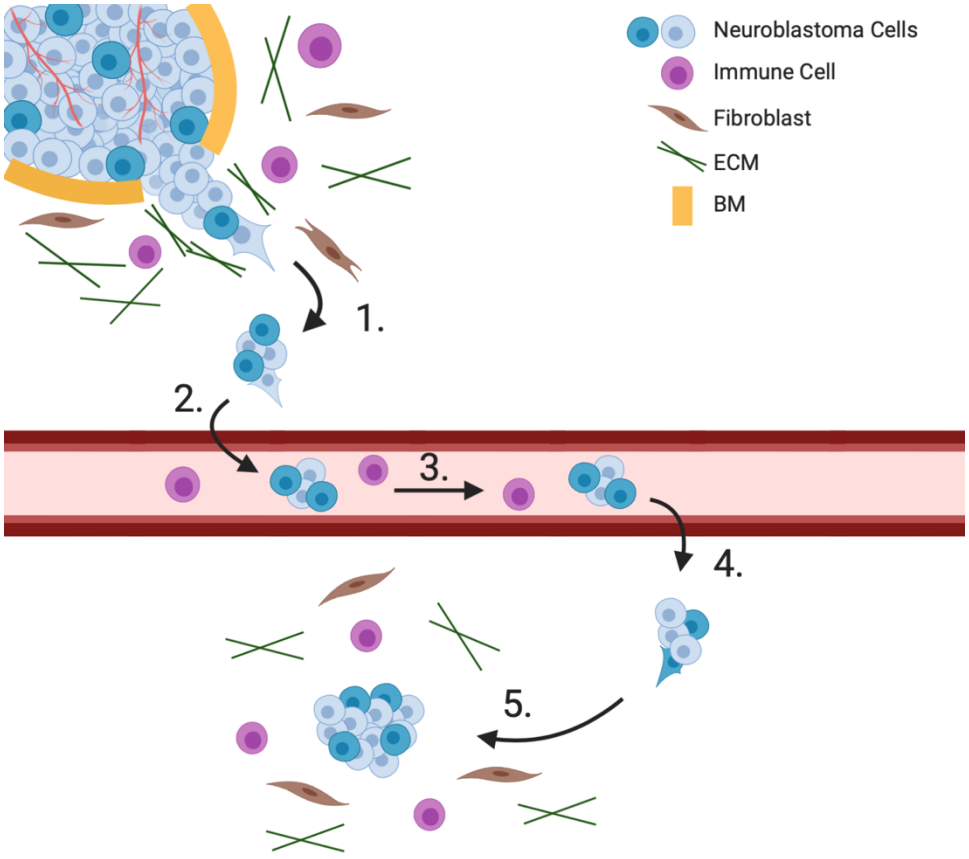

Figure 1.3 Schematic illustration of the metastatic cascade. The spread of cancer from its primary site to distant metastatic locations is a multistep process. 1) Local tumour invasion; tumour cells must penetrate the epithelial basement membrane, invade surrounding stroma and disseminate from the tumour mass. 2) Intravasation; tumour cells must enter the circulation through the bloodstream or lymphatic system by invading endothelial basement membrane. 3) Survival; cancer cells must avoid detection by the immune system and protect themselves from shear and oxidative stress. 4) Extravasation; malignant cells become trapped in a capillary bed and leave the circulation by invading through endothelial basement membrane once more. 5) Colonisation; tumour cells populate supportive pre-metastatic niches to form secondary tumours. BM; Basement membrane, ECM; Extracellular matrix.

1.4 Local tumour invasion

Tumour development occurs as a result of cancer cells collaborating with their surrounding cellular, molecular and physical stroma to establish ectopic organ-like structures. The cellular component of the tumour microenvironment (TME) contains many different cell types, including cancer cells, immune cells, fibroblasts and endothelial cells. The TME also has an extracellular component comprising of extracellular matrix (ECM) proteins and secreted factors such as cytokines, chemokines, growth factors (GFs) and hormones. To invade this surrounding stroma, malignant cells are believed to hijack migratory programs that are important during normal physiological processes such as development and wound healing (44).

The conversion of epithelial cells to a more migratory mesenchymal cell phenotype is known as the epithelial to mesenchymal transition (EMT) and is thought to play a role in many aspects of cancer progression, including local tumour invasion (45). EMT is a reversible process that involves the loss of apical-basal polarity, reorganisation of the cytoskeleton, release of cell-cell contacts and expression of proteins that can degrade components of the ECM. This process is initiated by EMT-inducing transcription factors (EMT-TFs) such as those belonging to the SNAIL superfamily, the zinc finger and E-box binding (ZEB) family as well as TWIST basic helix-loop-helix proteins. These EMT-TFs are activated through signalling pathways that respond to extracellular cues including WNT, Notch, TGF-β, BMPs and HIF (46, 47). Although EMT has been portrayed as a 'binary switch' in the past, it has become evident that this is a highly dynamic and plastic process that has a wide range of intermediate states (48, 49) and in fact the majority of circulating tumour cells express both epithelial (E-cadherin, cytokeratins, occludins) and mesenchymal (N-cadherin, vimentin, fibronectin) markers (50, 51). Furthermore, the high levels of cellular plasticity exhibited by intermediate EMT phenotypes is important for metastasis, where an epithelial phenotype must be regained in order for proliferation to occur at distant sites (52). Therefore, tumour cell invasion itself can be considered heterogenous and migration strategies depend on the degree of EMT that occurs.

Cancer cells can employ a variety of migration strategies to overcome environmental challenges. A full EMT causes migrating cancer cells lose cell-cell adhesion molecules, such as E-cadherin, allowing them to dissociate from the primary tumour. Depending on environmental conditions, single tumour cells can then migrate using either an amoeboid or an elongated-mesenchymal mode. Amoeboid migration depends on cytoskeletal contractility, whereby cells can squeeze through pre-existing pores in the ECM. Mesenchymal migration requires degradation of the ECM by proteases and high-levels of cell-ECM adhesion (53). Alternatively, intermediate or partial EMTs result in tumour cells migrating collectively as streams, sheets or strands. Multicellular streaming is the process by which loosely or non-adherent cells migrate along the same pathway, each generating their own traction force. In contrast, collective migration or invasion relies on cell-cell junctions being maintained over a period of time. In this case the leading edge, composed of one or several cells with mesenchymal traits, is responsible for generating traction force (54) (Figure 1.4). Importantly, the migration of tumour cells is a plastic process whereby cells can switch between modes of migration in response to their environment (55). Therefore, signals from the TME that drive EMT including hypoxic conditions, pro-inflammatory cytokines, mechanical properties and ECM components can dictate how tumour cells invade their surrounding stroma.

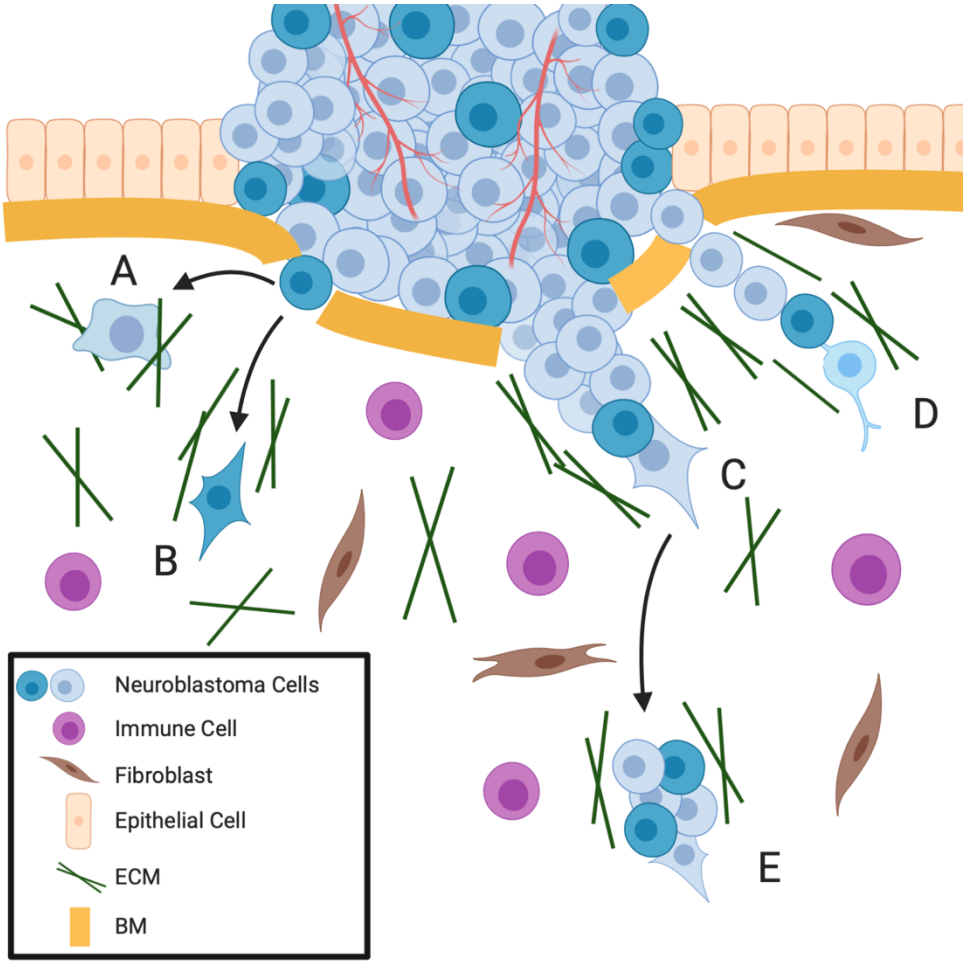

Figure 1.4 Schematic illustration of cancer cells employing different modes of migration during local tumour invasion. Depending on their local environment and the degree of EMT, cancer cells can invade using a variety of interchangeable cellular migration strategies. Individual disseminated tumour cells can migrate through pores in the ECM using the amoeboid mode of migration (A), alternatively they can engage the mesenchymal strategy to proteolytically degrade the ECM (B). Tumour cells can also migrate collectively as multicellular strands (C) or streams (D). Small groups of cells that disseminate from the tumour mass can migrate as clusters (E). Collective invasion relies on varying degrees of cell-cell contacts and matrix degrading enzymes. EMT; epithelial-mesenchymal transition, ECM; extracellular matrix, BM; basement membrane.

1.5 The ECM and local tumour invasion

The ECM refers to the acellular component of a tissue that provides both structural and biochemical support to its cellular residents. While ECM composition varies between tissues, the main components of this functional framework include fibrous proteins such as collagens type I and II and elastins, glycoproteins such as laminin, as well as a range of proteoglycans. These proteins are secreted by the ECM's cellular constituents and organized into a 3D mesh that is biologically active, in part due to the presence of secreted factors, such as cytokines, chemokines, growth factors (GFs) and hormones. Thus, the ECM regulates many cellular processes, including migration, proliferation, differentiation and cell fate (56). There are two main types of ECM, the interstitial connective tissue matrix and the basement membrane (BM). BMs are thin, dense, cell bound ECMs that coat the basal side of epithelial and endothelial cells and surround muscle, fat and the peripheral nerves. These ECMs are first expressed during early embryogenesis and self-assemble through binding interactions between laminin, collagen IV, nidogens and proteoglycans. BMs are rich in biochemical and biomechanical cues and hence play a role in many cellular processes including cell adhesion and migration, polarity, tissue shaping and signalling (57, 58). Unlike the BM, the interstitial matrix is loosely organised and surrounds individual cells, tissues and organs like a hydrated gel. While the composition of the interstitial matrix in any given microenvironment can vary, examples of major components of this matrix include collagens (collagen type I), glycoproteins (fibronectin, vitronectin) and matricellular proteins (thrombospondin) (59). Cell adhesion to the ECM is primarily mediated by the integrin family of transmembrane receptors, which act as a bridge between the cellular cytoskeleton and the ECM. Integrins bind ECM glycoproteins, such as laminins and collagens in the BM or fibronectin in the interstitial matrix. At sites of cell-ECM binding, integrins cluster and form adhesion complexes, such as focal adhesions and invadopodia. Importantly, these adhesion complexes have two roles in mediating cell migration; generating traction force by connecting the ECM to the cytoskeleton and activating intracellular signalling pathways that can control cell motility. Therefore, cell-ECM adhesion complexes integrate biochemical and biomechanical cues from the ECM and are paramount for cell migration (60, 61).

For a tumour to metastasise, first cancer cells must access the circulatory or lymphatic system. Therefore, the ability of tumour cells to penetrate the BM and invade through the surrounding interstitial matrix is critical. As previously mentioned, cancer cells can invade using a range of migration modes, but ECM remodelling is a common requirement. Matrix degrading enzymes, such as the matrix metalloproteinases (MMPs), create pathways through the ECM enabling cell migration. Amoeboid migration of tumour cells does not require matrix proteases however the deformability of the nucleus is a limiting factor and BMs are too dense for cells to migrate through using this mode of migration (53, 62). Thus, the secretion of MMPs by tumour cells and/or stromal cells such as cancer associated fibroblasts is required for local tumour invasion. Interestingly, induction of the EMT programme causes cells at the invasive front to secrete MMPs that degrade the BM. For instance, activation of the EMT programme by the transcription factor SNAIL induces the expression of MMPs (63, 64). Moreover, MMPs also play an important role in the EMT process during neural crest development (65), providing evidence that MMPs may be involved in the EMT and invasion of NB.

1.6 Invasion and the EMT in neuroblastoma

Due to its embryonal origin there is a lack of literature relating to the local invasion of NB. However, the migration of NCCs, the cells of origin for NB, exemplifies the EMT during development and is well studied in model organisms. It is likely that NB takes advantage of this intrinsic migratory potential to invade and metastasise and this hypothesis is supported in the literature (66). In fact, the migratory behaviour of NCCs during development is often compared to cancer metastasis in general (67). Following formation of the neural crest, cells of the former neural folds which are epithelial-like undergo an EMT and delaminate to become migratory NCCs. Delamination of chick trunk NCCs is triggered by a BMP/canonical Wnt cascade involving Bmp4, Wnt 1, Msx1 and c-Myb. This cascade, through activation of Snail2 (Slug), FoxD3 and members of the SoxE family (Sox9, Sox10), causes a cadherin switch, β1-integrin activation, basal lamina degradation and RhoB expression resulting in an EMT and migratory NCCs (68). Interestingly, similar molecular events have been seen in NB cells, whereby the proto-oncogene c-Myb regulates Slug transcription and induces expression of the mesenchymal markers vimentin, fibronectin and N-cadherin, resulting in

increased invasion through a Matrigel (BM/basal lamina extract) membrane (69). The expression of Slug is detectable in most NB cell lines, where its inhibition results in decreased cellular invasion *in vitro* (70). Vitali et al. also showed that the silencing of Slug reduced the metastatic burden in a tail-vein injection model of NB metastasis.

Similar to cancer invasion, matrix-degrading proteases are a requirement for NCC delamination and migration (71). This study demonstrates a critical role for MMP-9 in the dorsal neural tube of developing chick embryos; Blocking MMP-9 *in vivo* inhibits the migration of NCCs, while injecting MMP-9 conditioned media into these embryos induces enhanced and premature migration. It is also shown that MMP-9 facilitates this migration through its degradation of laminin, a key component of the BM. MMP-2 is also expressed in the avian NC and plays an integral role during initiation of the EMT, however its expression is transient and dissipates rapidly ones cells have delaminated (65). A recent study has confirmed the expression of both MMP-2 and -9 in mouse embryos, where their inhibition also prevents NCC migration (72). Interestingly, both MMP-2 and MMP-9 are expressed in NB tissue samples and their expression levels are elevated in samples from metastatic compared to non-metastatic disease (73, 74). The expression of MMP-2 and -9 has been also been shown in NB cell lines and in the case of MMP-9 expression is shown to increase their invasive capacity (75, 76).

1.7 Current models of tumour cell migration and invasion

For many years, researchers have attempted to model different aspects of the metastatic cascade, however due its complexity no model fully recapitulates this process. That being said many of these models have provided important information regarding the migration and invasion of tumour cells. Here, we will discuss models that are frequently used to assess the invasion of NB cells and cancer cells in general as well as their suitability as models of local tumour invasion in NB (Table 1.8). The most widely used *in vitro* techniques to assess cell migration and invasiveness are transwell assays (or modified Boyden chamber assays) and the wound-healing assay (or scratch assay). The Boyden chamber comprises of two wells separated by a semipermeable filter (migration assay) that can be coated with a layer of ECM (invasion assay). Chemoattractant is added to the lower chamber and tumour cells

in serum-free medium are added to the upper chamber. Invasive cells migrate through the membrane and can be quantified or recovered (77). The main benefits of this widely used assay are its relative ease and low-cost. However, this method has many limitations with regards modelling local tumour invasion. When cells are added to the Boyden chamber, they are individually exposed to a harsh gradient of chemoattractant, forcing them to migrate in order to survive. This is not indicative of the scenario *in vivo*, where cancer cells are exposed to different levels of nutrients/chemoattractant depending on their position within a tumour. Furthermore, this model only evaluates individually migrating cancer cells and it is an endpoint assay, meaning invasion through the membrane cannot be visualised in real-time. The scratch assay is also a relatively simple method of studying cell migration *in vitro,* whereby a confluent cell layer is "scratched", and the resulting gap is monitored using time-lapse microscopy. Cells will migrate to close the artificial wound and the rate at which this occurs can be measured (78). Unlike the Boyden chamber method, this assay allows migration to be observed in real-time and cell-cell contacts are maintained. However, while useful for studying the migration of epithelial sheets it also lacks the dimensionality needed to effectively model local tumour invasion. Although these assays are both routinely used to assess NB migration and invasion (79-81) their validity is questionable due to the aforementioned limitations , thus highlighting the need for more suitable *in vitro* models.

Solid tumours have a complex 3D architecture which results in a heterogenous exposure to biochemical (nutrients, oxygen) and biophysical (stiffness) properties in the microenvironment. While difficult to model in 2D, these aspects of tumour biology can be partially recreated in 3D *in vitro.* The most commonly used 3D *in vitro* models of local invasion utilise multicellular tumour spheroids (MCTS); aggregates of cancer cells (cell lines or primary cells) created by compacting cells together using techniques such as the hanging drop method (82). This method forms homogenous spheroids that secrete ECM, meaning spheroids gain cell-cell and cell-ECM adhesions during the process. For invasion assays MCTS are embedded in ECM gels, usually composed of collagen type I or basement membrane extract (BME). This method was proposed to model small avascular tumours and has been used to study invasion in NB (83) as well as other cancers, including ovarian, glioma and squamous cell carcinoma (84-86). This model offers many advantages over the *in vitro* methods mentioned above. Spheroids are more representative of *in vivo* tumours due to

their dimensionality, cell-cell and cell-ECM adhesions. They can also be cultured or co-cultured in a range of 3D matrices to model the native TME and explore its effects on invasion. Furthermore, MCTSs are capable of mimicking *in vivo* diffusive gradients, resulting in necrosis at their cores and regions of hypoxia (87). Although MCTS are valuable for invasion studies in some cancers, their use is limited to incubation periods that are less than one cell cycle and hence they can only be used to study rapidly migrating cancer cells, such as those mentioned previously. MCTS are also made up of cells that have previously adapted to a 2D *in vitro* environment, which results in homogeneity and hence poses disadvantages in terms of modelling intratumour heterogeneity (ITH) (88).

In vivo murine models are often the gold standard in terms of cancer research, providing the most applicable representation of human tumours *in situ.* However, this is not necessarily the case in terms of models for tumour cell migration and invasion. One of the primary challenges of modelling invasion *in vivo* is the need to visualise the process optically. In this regard, studies involving flies (*Drosophila melanogaster)* and zebrafish (*Danio rerio)* are more widely used when assessing migration and invasion. In a *Drosophila* model of colorectal cancer*,* controlled expression of Snai1 has been shown to induce a partial EMT, collective invasion through the BM, migration to distant sites and seeding of polyclonal metastasis (89). This model has many advantages including the ability to visualise this entire process, low cost and efficiency (2-3 weeks). That being said, *Drosophila* embryos are not used to study NB because they have no neural crest or enteric nervous system. Zebrafish on the other hand have been widely used to study the neural crest (90).

Xenotransplantation of human cancer cell lines into zebrafish is often used to assess their invasive capacity (91, 92). Specifically, the zebrafish embryo is regularly used due to its transparency and *ex utero* development, allowing for direct imaging of the cells*.* Zebrafish also lack an adaptive immune system at early stages, meaning immune rejection is uncommon. Furthermore, ethical issues do not arise until zebrafish embryos are five days old (93). While this method can allow visualisation of single cell migration during intravasation, extravasation and invasion of distant tissues it does not effectively model local invasion of malignant cells from a primary tumour (94). This is likely due to cells being injected in suspension and hence lacking cell-cell adhesions and poorly representing a

tumour mass, which would explain their rapid migration away from site of injection. In fact, many studies quantify invasion by counting the number of cells that extravasate (95). That being said, tumours that metastasise can be grafted into certain zebrafish models, however they require immunosuppressed, artificially transparent (*casper* strain) adult transgenic fish, adding to the cost and time associated with experiments (96). Interestingly, Tang et al. have developed this model for melanoma and NB cells. While this is more reflective of native metastasis, invasion of the primary tumour cannot be observed in real-time and the model still lacks physiological relevance as NB cells are engrafted retro-orbitally. Transgenic zebrafish models of NB have also been developed and are more physiologically relevant due to the spontaneous development of tumours in the zebrafish analogue of the adrenal gland (the interrenal gland)(97, 98). That being said, these tumours do not metastasise and thus cannot be used to study local invasion.

In recent years, models that effectively recapitulate the embryonal tumorigenesis of NC-derived tumours, namely NB and melanoma, have been developed in avian embryos (99, 100). In both studies GFP-labelled cancer cell lines are grafted into the chick neural crest, specifically between somite 18 and 24 (sympatho-adrenal level) in the case of NB. These studies show that both NB and melanoma cells retain and can reactivate aspects of their NCC-like embryonic gene program. In their model of NB, Delloye-Bourgeois C et al. highlight that malignant human cells display collective migratory behaviour similar to that of NCCs but subsequently proliferate and disseminate via the dorsal aorta and peripheral nerves thus maintaining their tumorigenic and metastatic potential. This model is an excellent representation of the early events in NB pathogenesis and as such has many advantages over the previously discussed models of local invasion. The model is faithful to the embryonal origin of NB, it has good optical accessibility, cell migration can be observed in real-time and it is relatively low-cost compared to murine models. That being said, this model is not suitable for high-throughput drug screening and the cellular strategies of invasion cannot be seen in high-resolution. It is also difficult to isolate metastatic cells for analysis once grafted into the embryo.

Crucially, many of the models discussed thus far lack physiological relevance to *in vivo* tumours. To this end the imaging of cancer cells in live animals using intravital microscopy

has come to the fore in the last two decades. This method can be used to image local invasion in high-resolution by implanting a window in close proximity to mouse tumours. Imaging relies on the excitation of fluorescence, which is usually achieved using multiphoton microscopy, although other microscopic techniques can be used (101). In recent years this model has been used effectively to gain insight into invasion programs, particularly in breast cancer, where distinct migration strategies have been observed in real time *in vivo*, including collective invasion and single cell dissemination (102, 103). In melanoma, cells have also been shown migrating through the *in vivo* mouse ECM collectively as well as adapting their mode of migration to overcome environmental challenges (104). Intravital imaging has also been used to study the cellular dynamics of invasion in other cancers including glioma (105) and pancreatic (106), however this state-of-the-art technique remains untested in terms of local tumour invasion in the majority of cancers. While intravital imaging has not yet been used to study NB, the technique has been implemented in transgenic mice to live image embryonic development *in utero* (107), which indicates its potential for investigating early embryonal events in local NB invasion. This method allows simultaneous imaging of tumour cells and a relevant *in vivo* TME which is extremely advantageous but also poses challenges given the associated complexity. For instance, the method is limited by the availability of fluorescent reporters and dyes as well as a lack of image processing tools capable of handling the large 5D datasets that are generated (108). Furthermore, intravital imaging and multiphoton microscopy raise ethical concerns and the associated cost is far greater than any of the previously mentioned models.

Table 1.8 Advantages and limitations associated with current *in vitro* and *in vivo* models applicable to tumour cell invasion in NB.

Model/Assay	Dimensionality	Advantages	Limitations	References
Scratch wound	2D	• Simple • Low-cost • Potential for high throughput	• 2D epithelial sheet migration • Cell proliferation can contribute	(78)
Transwell/Boyden chamber	2D (migration) 3D (invasion)	• ECM composition optional • Potential for high throughput	• Single cell migration/invasion only • Dimensionality (No 'tumour mass') • Inconsistent ECM layer (thickness) • Unrealistic chemotactic gradient • Endpoint assay (no real-time imaging)	(77)
Multicellular Tumour Spheroids (MCTS)	3D	• Dimensionality (Cell-cell, cell-ECM contacts) • ECM gels (composition optional) • Tumour mass (diffusive gradients) • Co-culture possible	• Rapidly migrating cells only • Homogenous cell populations	(82, 85, 87)
Xenotransplantation into Zebrafish	3D	• No adaptive immune system at early stages • No ethical issues < 5 days old • *In vivo* ECM	• Lacks physiological relevance for local invasion • No metastasising ‘tumour mass’ • Low physiological temperature (27°C) compared to human	(92, 93, 98)

Xenotransplantation into Chick Embryo	3D	• Low cost compared to murine • Good physiological relevance • Live imaging	• Not suitable for high throughput • Invasion not imaged in high resolution • Difficult to isolate metastatic cells once grafted	(99)
Intravital Imaging	3D	• Good physiological relevance • Dimensionality • *In vivo* TME • Transgenic mice (spontaneous tumours)	• Ethical concerns • Highly complex, challenging data analysis • Limited by availability of fluorescent reporters • High cost	(102, 104, 108)

ECM; Extracellular matrix, TME; Tumour microenvironment, MCTS; multicellular tumour spheroids

1.8 Aims and objectives

Given the significant gap in our knowledge regarding local tumour invasion in general and particularly in NB and the fact that about half of NB patients present with metastatic disease, we propose that modelling NB invasion in 3D may provide a platform for developing an understanding of this complex heterogenous process. Therefore, the aims of this study were as follows:

1. To investigate the suitability of 3D organoid culture assays for the study of local NB invasion.

2. To characterise the migration strategies employed by NB cells to navigate different ECM environments.

3. To compare the behaviour of NB cell lines to that of NB organoids in 3D ECM cultures.

4. To investigate the role played by *MYCN* in local NB invasion using the SHEP-Tet21N system.

2. Materials and Methods

Cell culture experiments (subheadings 2.1-2.13) were conducted by Dr Olga Piskareva during her Fullbright fellowship to the research group of Professor Andrew Ewald in the Cell Biology Department at Johns Hopkins School of Medicine, MD, USA. Dr Piskareva provided me with the raw imaging data generated by these experiments to analyse and present for this MSc by research. The methods carried out to generate this dataset have been previously published by Professor Ewald's group for the study of breast cancer invasion (109). The experimental design optimised for NB will be described here briefly.

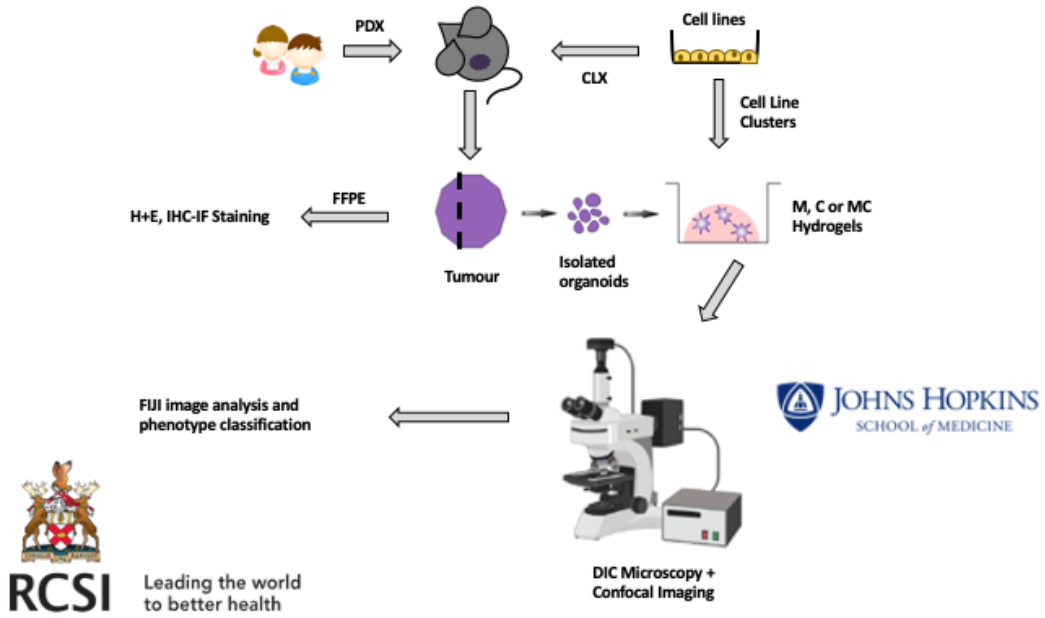

Figure 2.0 Schematic illustration of the experimental design for this project.
This study was a collaborative project between Johns Hopkins and RCSI. All cell culture experiments were carried out by Dr Piskareva in the Cell Biology Department at Johns Hopkins School of Medicine (MD, USA). Data analysis and staining of formalin-fixed paraffin embedded samples was carried out by Cian Gavin in the Department of Anatomy and Regenerative Medicine/School of Pharmacy and Biomolecular Sciences at RCSI. PDX; Patient-derived xenograft, CLX; Cell line xenograft, M; Matrigel, MC; Matrigel:Collagen (1:1), FFPE; Formalin fixed paraffin embedded, IHC-IF; Immunohistochemistry-immunofluorescence.

2.1 Isolating neuroblastoma organoids from tumour xenografts.

NB PDXs were shipped on dry ice within 24 hours by the Children's Oncology Group (Texas Tech University, TX, USA). SH-SY5Y cells were subcutaneously xenografted into 6-8 week-old female Hsd:Athymic Nude-Foxn1nu mice by Meaghan Haynes (Dept of Cell Biology, Johns Hopkins School of Medicine, MD, USA). All organoid isolations were performed in a sterile hood. NB tumour xenografts were minced with a scalpel approximately 25-50 times per tumour. The minced tumours were transferred to collagenase solution (10mL per tumour) in a 50mL tube. The suspension was shaken to break the tissue into smaller pieces. The tube was then centrifuged at 1500rpm for 10 minutes at room temperature to separate the solution into three layers; the fatty layer on top, aqueous layer in the middle and a red pellet at the bottom containing tumour tissue. The opaque fatty layer was transferred into a BSA coated 15 mL tube using BSA coated pipette tips. BSA is used to prevent organoids from clumping together. 10mL of DMEM/F12 was added to the tube and pipetted up and down to disrupt the fatty layer. The tube was centrifuged at 1500rpm for 10 minutes at room temperature. The fat and supernatant were aspirated and the pellet containing additional tumour tissue was kept. The aqueous layer was aspirated from the tube containing the original pellet and 10 mL DMEM/F12 was added. The pellet was resuspended and then combined with the pellet of tumour tissue from the fatty layer in the 15mL tube. The solution was mixed well by pipetting vigorously up and down. The tube was then centrifuged at 1500rpm for 10 minutes at room temperature. The supernatant was aspirated and 4 mL DMEM/F12 was added to the combined pellet which now contained small clusters or tumour organoids and stromal cells attached to each other. 40µL of DNase was added to the 4mL organoid suspension and the tube was gently inverted by hand for 2-5 minutes at room temperature to break up the clusters and detach organoids from single cells. 6 mL of DMEM/F12 was added and mixed thoroughly by pipetting up and down. The tube was centrifuged at 1500rpm for 10 minutes at room temperature. The supernatant was aspirated to the 0.5 mL mark. The pellet was resuspended in 10mL DMEM/F12 and mixed well. The tube was then centrifuged for 3-4s after it reaches 1500rpm. These three steps were repeated three more times and yielded an off-white pellet consisting almost entirely of NB organoids.

2.2 Determining the density of the organoid suspension

The organoid pellet was resuspended in 10mL DMEM/F12 and mixed thoroughly until homogenous. 50µL of organoid suspension was transferred to a 30mm Petri dish and the number of organoids in this sample volume was counted under the microscope. The organoid density was calculated and then readjusted to 1000 organoids/mL. The organoid suspension was then aliquoted into 1.5mL BSA-coated microcentrifuge tubes (to avoid clumping) at the required volume for each experiment. Each tube was centrifuged at 1500rpm for 5 minutes at room temperature and the supernatant was aspirated without disturbing the pellet.

2.3 Plating organoids in Matrigel

Matrigel used in all experiments was growth factor reduced (GFR Matrigel®, Corning ®). Matrigel was thawed at 4°C and the required volume to reach a final density of 2 organoids/µL was calculated. The required volume of Matrigel was added to a microcentrifuge tube with the organoids and kept on ice to avoid gelation. The Matrigel/organoid suspension was mixed until homogenous and then 100µL was added to each well of a plate (For time-lapse imaging, plates with glass bottoms were used). The plate was kept on a heating block for several minutes to allow gelation and then incubated at 37°C, 5% CO2 for 30-60 minutes. Pre-warmed organoid medium (DMEM/F12, 1% penicillin/streptomycin, 1% insulin-transferrin-selenium) was then added to each of the wells. PBS was added to the empty wells.

2.4 Preparing the neutralised collagen I solution

Neutralized collagen I solution contained 87% rat tail collagen type I, 10% DMEM 10X and 3% 1.0 N NaOH. DMEM 10X was first combined with NaOH and mixed well. The collagen I was then added and mixed well until the colour remained stable. The desired colour was light pink or salmon which corresponds to a pH of 7.0-7.5. The pH was tested using pH strips and the neutralised collagen I solution was adjusted to a concentration of 3mg/mL using DMEM 1X.

2.5 Plating organoids in collagen I

In a 24-well glass bottomed plate, wells were pre-coated with a small amount of neutralized collagen at room temperature, this step ensures attachment of the collagen/cell suspension to the plate. The plate was incubated at 37°C. The neutralized collagen I for hydrogel formation was pre-incubated at 4°C for 60-120 minutes. This pre-incubation period has been shown to affect the assembly of collagen fibrils within gels, impacting cellular behaviour (110). Thus, the collagen hydrogels used here were prepared using preassembled collagen I as described by Nguyen-Ngoc et al. Once the collagen I was preassembled (solution turned cloudy and fibrous), it was kept on ice. The plate was placed in a heating block set to 37°C. The required volume of preassembled collagen I was added to the organoid pellet (subheading 2.2) (desired density was 2 organoids μL^{-1}). The pellet was resuspended and 100µL of collagen/organoid suspension was plated in each pre-coated well. The plate was kept on the heating block for several minutes to allow gelation before being returned to the incubator (37°C, 5% CO_2) for 45-60 minutes. Pre-warmed organoid medium was then added to each of the wells. PBS was added to the empty wells.

2.6 Plating neuroblastoma organoids in a mixture of Matrigel and collagen I

Neutralised collagen solution was prepared as described in subheading 2.4. Each well of a glass bottom plate was pre-coated with 20-30µL of neutralised collagen at room temperature. Preassembled collagen I solution was prepared as in subheading 2.5. Matrigel was combined with preassembled collagen I at a ratio of 1:1 (MC) and well mixed until homogenous. The mixed matrix solution was kept on ice. Organoids were resuspended in the desired volume of solution and mixed well. 100µL of mixed cell/MC suspension was plated in each pre-coated well. The plate was kept on the heating block for several minutes to allow gelation before being returned to the incubator (37°C, 5% CO2) for 45-60 minutes. Pre-warmed organoid medium was then added to each of the wells. PBS was added to the empty wells.

2.7 Plating neuroblastoma cell lines in Matrigel

7 NB cell lines (Table 2.7) were cultured in T75 cell culture flasks until 90% confluent and then harvested using Trypsin-EDTA. Cells were cultured in medium containing supplements as described in Table 2.7. Cells were resuspended in medium and counted using a haemocytometer. The required volume of cell suspension was aliquoted in a microcentrifuge tube (BSA coated) and spun down at 1500rpm for 5 minutes. Matrigel was thawed at 4°C and the required volume to reach a final density of 1-2 cells/µL was calculated. The required volume of Matrigel was added to a microcentrifuge tube with cells and kept on ice to avoid gelation. The Matrigel/cell suspension was mixed until homogenous and then 100µL was added to each well of a plate containing a glass bottom (required for time-lapse imaging). The plate was kept on a heating block for several minutes to allow gelation and then incubated at 37°C, 5% CO2 for 30-60 minutes. Pre-warmed medium was then added to each of the wells. PBS was added to empty wells.

Table 2.7 Neuroblastoma cell lines and corresponding culture medium used.

Cell Line	Culture Medium
Kelly	RPMI, 10% FBS, 1% P/S
KellyCis83	RPMI, 10% FBS, 1% P/S
CHP-212	MEM:F12, 10% FBS, 1% L-glut, 1% P/S
SH-SY5Y	MEM:F12, 10% FBS, 1% P/S
NB1691	RPMI, 10% FBS, 1% P/S
SHEP-Tet21N	RPMI, 10% FBS, 1% P/S
Lan-1	MEM:F12, 10% FBS, 1% P/S

FBS; fetal bovine serum, P/S; penicillin/streptomycin.

2.8 Plating neuroblastoma cell lines in collagen I

Neutralised collagen I and preassembled collagen I were prepared as in subheadings 2.4 and 2.5 respectively. Plates previously pre-coated with neutralized collagen I were placed in a heating block set to 37°C. Cell pellets (as prepared in subheading 2.6) were resuspended in the required volume of preassembled collagen I. 100µL of cell/collagen I suspension was plated in each pre-coated well. The plate was kept on the heating block for several minutes to allow gelation before being returned to the incubator (37°C, 5% CO2) for 45-60 minutes. Pre-warmed medium was then added to each of the wells. PBS was added to the empty wells.

2.9 Plating neuroblastoma cell lines in a mixture of Matrigel and collagen I

Collagen I was prepared as previously described. Each well of a glass bottom plate was pre-coated with 20-30µL of neutralized collagen at room temperature. Matrigel was combined with preassembled collagen I at a ratio of 1:1 (MC) and well mixed until homogenous. The mixed matrix solution was kept on ice. Cell pellets (subheading 2.6) were resuspended in the desired volume of solution and mixed well (1-2 cells/µL). 100µL of mixed cell/MC suspension was plated in each pre-coated well. The plate was kept on the heating block for several minutes to allow gelation before being returned to the incubator (37°C, 5% CO2) for 45-60 minutes. Pre-warmed medium was then added to each of the wells. PBS was added to the empty wells.

2.10 3D invasion assays.

We set out to investigate the invasion of NB organoids and cell lines into 3D ECM cultures. To determine the optimal growth conditions and ECM composition for invasion, we cultured organoids isolated from Felix-PDX in organoid medium supplemented with 10% FBS and 2.5nM bFGF (FGF-2), 10% FBS only or 2.5nM bFGF only. For the remaining invasion assays all organoids were cultured in organoid medium supplemented with both 10% FBS and 2.5nM bFGF. For invasion assays of clonal cell line clusters, 2.5nm bFGF was added to standard cell culture medium (table 2.7). Differential interference contrast (DIC) microscopy was used to optically monitor NB invasion *ex vivo* in high resolution. Organoids were monitored using time-lapse microscopy, where images were captured every 20 minutes for 5 days beginning

on the day organoids were plated (t0hr). Cell line clusters were monitored daily and the first time-point was 24 hours after initial cell seeding (t24hr).

2.11 The SHEP-Tet21N cell line

The SHEP-Tet21N cell line was developed on the basis of a system designed by Bujard and Gossen for reversibly controlling gene expression in HeLa cells (111). The study describes a tetracycline transactivator (tTA) protein that was created by fusing the tetracycline repressor of E Coli with the activating domain of protein virion 16 of herpes simplex virus. The tTA they generated stimulates transcription of a target gene, but its activity is sensitive to the antibiotic tetracycline. Lutz et al. used this method to develop a synthetic inducible expression system for MYCN in the SH-EP cell line, where MYCN is barely detectable at endogenous levels (112). The resulting cell line, SHEP-Tet21N, has a reversible "on/off" switch for MYCN expression that is controlled by tetracycline. Here, we use a more potent derivative of tetracycline, doxycycline, to repress/turn "off" the transcription of MYCN (Figure 2.11). Thus, for experiments requiring MYCN repression, SHEP-Tet21N cells were cultured continuously in 50ng/mL of doxycycline.

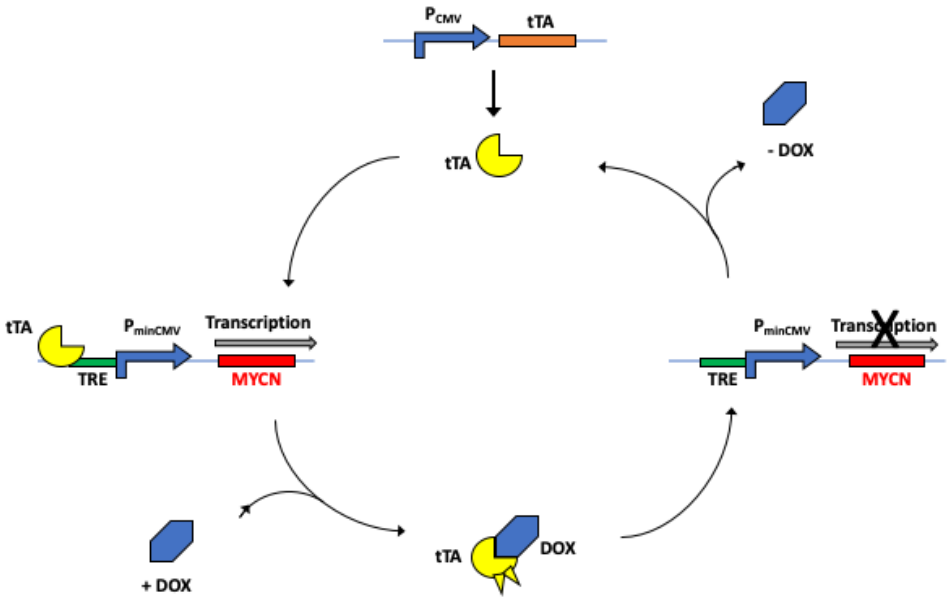

Figure 2.11 Schematic representation of the reversible N-myc expression system in the SHEP-Tet21N cell line. In the absence of doxycycline the Tet-Transcriptional Activator (tTA) can bind to the transcriptional regulatory element (TRE), which is downstream of the minimal immediate early promoter cytomegalovirus(P_{minCMV}), resulting in transcription of *MYCN.* When doxycycline is added, it inhibits the binding of tTA to the TRE domain, preventing the downstream transcription of *MYCN*.

2.12. Ethidium Homodimer (EHD) staining

The membrane impermeable, fluorescent nucleic acid dye, EHD, was used to stain dead cells within 3D hydrogel cultures. EHD solution was added directly to the culture medium and incubated for 30 minutes while protected from light. Live florescent images were then taken of clusters/organoids to assess viability.

2.13 Fluorescence staining of whole 3D hydrogels

Once the imaging experiments were completed (t120hr in culture), organoid medium was removed from the wells and the hydrogel samples were washed with DPBS and fixed in 4% paraformaldehyde (PFA). PFA was then removed and the samples were washed three times with DPBS. Gels were permeabilized with 0.5% Triton X-100 and immediately blocked with 10% FBS in DPBS. The hydrogels were then incubated with phalloidin and DAPI to stain F-actin and cell nuclei respectively. Images of organoids/cell clusters were taken using a confocal microscope.

2.14 FIJI image analysis

3D ECM culture assays of NB organoids and cell line clusters generated a large dataset of images (approx. 400GB). These images were manually examined to classify organoid/cell cluster phenotypes based on morphology. NB organoids were grouped into six distinct phenotype classifications based on specific morphological traits. The images were then analysed and processed using FIJI (Fiji is just imageJ) image analysis software. Images were spatially calibrated and organoids/cell clusters were selected by manually outlining their perimeter (Figure 2.14). The area of organoids/cell clusters was then calculated by FIJI software in μm^2. By comparing the area of organoids/cell clusters every 24 hours their relative growth at any given time point could be calculated using the following formulas; *area t(x)-area t0hr/area t0hr* for organoids and *area t(x)-area t24hr/area t24hr* for clonal cell clusters. Using the same method for organoid and cell cluster selection, we also used

FIJI to calculate circularity values, which we used to confirm our microscopic observations of phenotypic changes. This is calculated by FIJI using the following formula; $4\pi*area/perimeter^2$. Circularity is calculated as a fraction of 1.0, where the value 1.0 indicates a perfect circle, while values approaching 0.0 indicate an increasingly elongated shape. Circularity measurements were used to support microscopic observations of invasiveness, where decreasing circularity was found to correlate with increasing levels of invasion (113, 114). Large organoids/cell clusters can generally be classified as invasive, mildly invasive or non-invasive based on the respective circularity scores; <0.4, 0.4-0.7, >0.7. It is important to note that circularity values lack validity for very small cells/clusters.

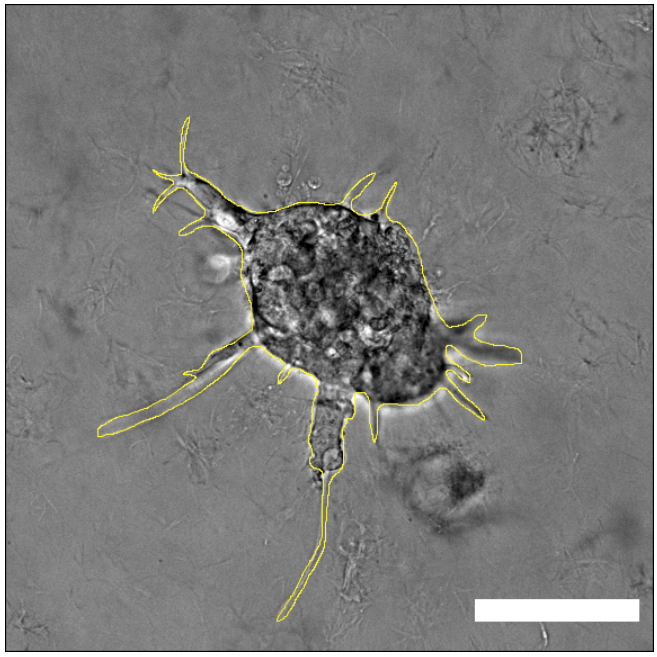

Figure 2.14 Representative image of manual organoid selection using FIJI image analysis software. Example illustrating the manual selection of an organoid using FIJI image analysis software. Area = $16.37x10^3 \mu m^2$, circularity = 0.084. Scale bare = 100µm

2.15 Exclusion Criteria

A number of technical issues were encountered while processing this dataset which led to certain organoids and/or cell line clusters being excluded from the analysis. A small proportion of organoids/clusters came into contact with and adhered to the cell culture plate, resulting in cells spreading out into a 2D monolayer (Figure 2.15 A). These organoids/cell clusters were easily identifiable due to their transparent appearance and

their significant cell spreading that results in an unusually large size compared to populations that remain embedded in the gels. Non-viable organoids/cell clusters were also excluded from the analysis. These organoids/cell clusters maintained an identical morphology and size across time-lapse images indicating the absence of any viable cells (Figure 2.15 B). When organoids/cell clusters were embedded in close proximity to neighbouring cell populations, they were seen to migrate toward each other and merge (Figure 2.15 C), likely as a result of secreted factors. For this reason, organoids/cell clusters that were in close proximity to another cell population were excluded from the analysis. In some instances, an error occurred with cell tracking, whereby the organoids/clusters selected were lost by cell tracking software (Figure 2.15 D) due to cell migration or plate re-calibration errors and hence not included in the analysis.

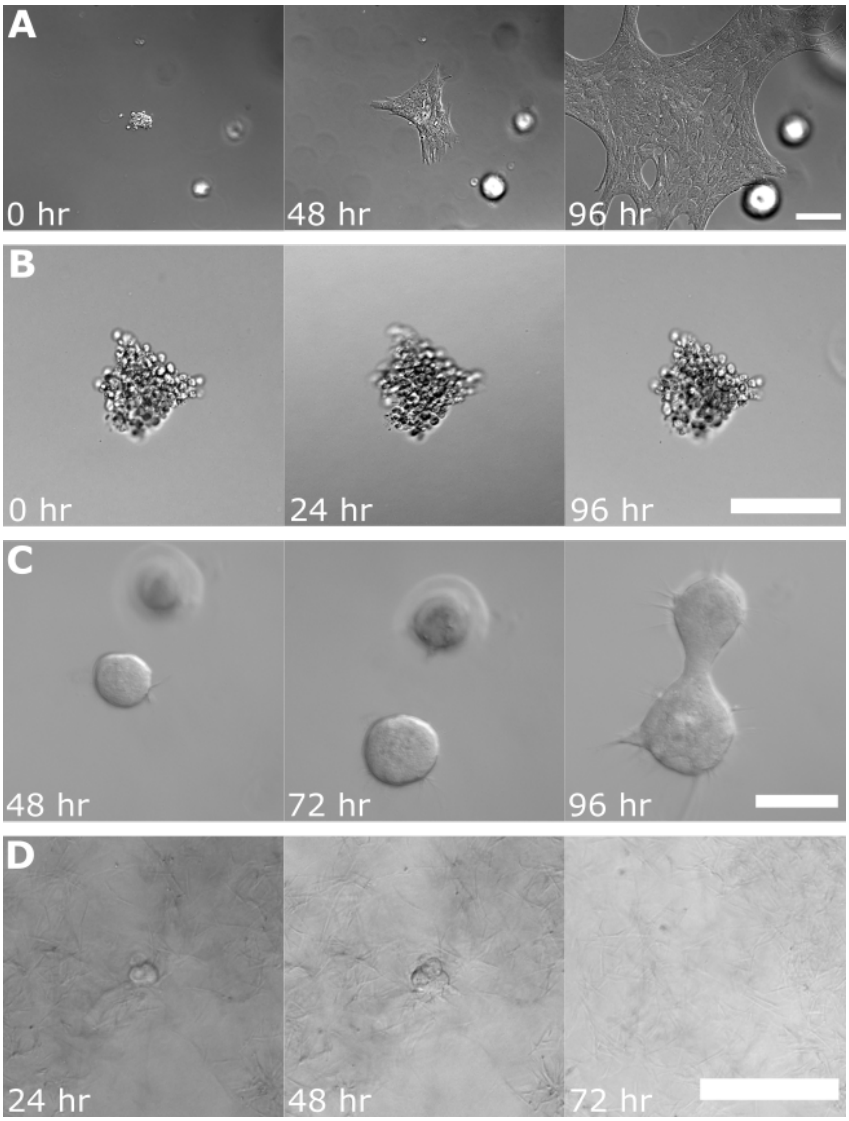

Figure 2.15 Technical issues encountered that resulted in organoids/cell clusters being excluded from image analysis. Representative DIC images displaying organoids/cell line clusters that were excluded from the analysis due to technical issues. Organoids/cell clusters were excluded if they adhered to the cell culture plate (A), were non-viable (B), were plated in close proximity to a neighbouring cell population (C) or were lost by cell tracking

2.16 Processing of paraffin-embedded samples

Tissue samples were previously embedded in paraffin wax using tissue processing cassettes. Wax embedded tumours were mounted onto the vice grips of a microtome (LEICA RTV 1225) and the block was trimmed by sectioning at 30µm until the sample was visible. Sections were then cut at 3µm and placed directly into a 40°C water bath. Samples were mounted onto poly-lysine slides (VWR, Germany) and transferred to a heated slide rack to dry. Once dry, slides were incubated overnight (12 hours) in a 60°C tissue drying oven.

2.17 Haematoxylin and Eosin (H&E) staining

Once slides were removed from the tissue baking oven, they were deparaffinized and rehydrated through multiple xylene (Sigma-Aldrich, Germany) and ethanol (EtOH) washes. The tissue was submerged in xylene twice for 3 minutes and then consecutively in 100% EtOH twice for 5 minutes, 95% EtOH twice for 3 minutes and 70% EtOH once for 3 minutes. The tissue was then rehydrated by submerging slides in distilled water (diH_2O) for 3 minutes. To stain cell nuclei, slides were submerged in pre-filtered Harris Haematoxylin (Sigma-Aldrich, Germany) for 4 minutes and then rinsed in running tap water for 10 minutes. This was followed by 3 dips in acid alcohol (0.25% hydrochloric acid in 70% EtOH) to remove any excess dye. Slides were then rinsed in tap water for 5 minutes before being submerged in Eosin Y solution 1% (Sigma-Aldrich, Germany) for 2 minutes to stain the cytoplasmic/ECM portion of tissue. Once stained, tissue was dehydrated by consecutively submerging slides in 95% EtOH twice for 3 minutes, 100% EtOH twice for 3 minutes and xylene twice for 3 minutes. Slides were then allowed to dry in a fume hood. One or two drops of DPX mountant (Sigma-Aldrich, Germany) was then added and slides were carefully mounted with coverslips using forceps.

2.18 Immunofluorescence staining

Paraffin embedded samples were processed as in subheading 2.16. Slides were removed from the tissue-baking oven and deparaffinized by submerging in Xylene (Sigma-Aldrich, Germany) twice for 5 minutes. Tissue was rehydrated by consecutively submerging slides in

decreasing concentrations of EtOH as follows; 100% EtOH twice for 3 minutes, 95% EtOH twice for 3 minutes and 70% EtOH once for 3 minutes. Residual EtOH was removed by washing slides once in tris-buffered saline (TBS; 20mM Tris base, 150mM NaCl, pH 7.4) for 5 minutes. Antigen retrieval was executed using the heat induced epitope retrieval (HIER) method. Freshly made sodium citrate buffer (10mM Sodium Citrate (Sigma-Aldrich, Germany), 0.05% Tween 20 (Sigma-Aldrich, Germany), pH 6.0) was preheated in a microwave. Slides were then fully submerged and boiled in the citrate buffer for 8 minutes. Slides were allowed to cool and subsequently washed twice in TBS-T (TBS with 0.1% Tween 20). Individual tissue sections were surrounded with a hydrophobic layer using a PAP pen (Sigma-Aldrich, Germany). To prevent non-specific antibody binding, blocking solution containing 5% Normal Goat Serum (NGS) (Thermo Fisher, USA), 1% Bovine Serum Albumin (BSA) (Sigma-Aldrich, Germany) and 0.1% Tween 20 was applied to specimens for 90 minutes at room temperature. Blocking solution also contained 0.5% Triton X-100 (Sigma-Aldrich, Germany) for tissue permeabilization. Blocking solution was removed and slides were incubated with primary antibody solution in the dark at room temperature for 60 minutes and then overnight at 4°C. Primary antibody solution contained 1% NGS, 1% BSA and 0.1% Tween in PBS to ensure minimal non-specific antibody binding. Slides were washed once with TBS-T for 5 minutes and three times with TBS for 3 minutes to remove any unbound primary antibody. Secondary antibody solution (PBS, 1% BSA, 1% NGS, 0.1% Tween 20) was applied and slides were incubated in the dark for 90 minutes at room temperature. Secondary antibody was removed by washing once with TBS-T for 5 minutes and three times with TBS for 3 minutes. DAPI was applied (0.5µg/mL in PBS) for 4 minutes to fluorescently stain cell nuclei and then removed by washing slides once in TBS for 3 minutes. Slides were mounted with appropriate cover slips using Prolong™ Diamond Antifade Mountant (Thermo Fisher, USA) and left overnight to dry.

The primary antibodies used for staining were Rabbit Anti-Vimentin (ab92547, Abcam, UK) at a working concentration of 1:200, Rabbit anti-N-Cadherin (D4R1H, Cell Signalling Technology, USA) at a working concentration of 1:125 and Mouse anti-Neuron-Specific Enolase (Clone BBS/NC/VI-H14, Agilent Dako, Santa Clara, CA, USA) at a working concentration of 1:200. Fluorescently tagged secondary antibodies were used to detect primary antibody binding, namely Goat Anti-Rabbit (Alexa Fluor® 488) (ab150077, Abcam,

UK) and Goat Anti-Mouse IgG (TRITC) (ab6786, Abcam, UK). Negative controls were used to confirm positive immunofluorescence staining. Primary antibody was not applied to the selected tissue sections, but the remaining experimental procedure was unchanged. Representative images of stained sections were digitally recorded using a Nikon i90 eclipse fluorescent microscope with Nikon Nis elements software run on a PC.

2.19 Statistical analysis

All statistical analyses were performed using Prism Software (Graphpad Software Inc, La Jolla, CA, USA). We performed statistical analysis to compare the relative growth of organoids/cell clusters across different matrices and different conditions. This analysis involved comparing unmatched, gaussian populations where equal variances could not be assumed. Therefore, we used either unpaired t-tests with Welch's correction or Brown-Forsythe One-Way ANOVAs followed by T3 Dunnett post-hoc tests, depending on the number of groups, to compare the equality of means between populations. We also performed statistical analysis to compare the circularity of organoid/cell cluster populations at different time points. In this case we had non-normally distributed data and thus performed non-parametric analyses. We used Kruskal-Wallis followed by Dunn's post hoc tests for multiple comparison between time-points.

3. Results

Chapter 3.1 Pairing PDXs and 3D culture assays to model local invasion in neuroblastoma

3.1.1 Introduction

Subpopulations of cancer cells within a given tumour can display different phenotypic features, including cellular morphology, gene expression, drug resistance, cell motility, and metastatic potential (115). This is known as intra-tumour heterogeneity (ITH) and is a hallmark of all malignancies, including NB. Therefore, it is extremely important that preclinical models of disease progression maintain this cellular heterogeneity. The most widely used models of high-risk NB are tumour cell lines, xenografts derived from these cell lines and genetically engineered mouse models, all of which have major limitations with regard maintaining ITH. Cell lines are derived through clonal expansion of specific cancer cells within a population, whereby the cells that survive in culture have up-regulated pro-survival genes. One study suggests that the cell lines used in the NCI-60 panel (116), regardless of their tissue of origin, are more recapitulative of each other than the clinical samples which they are used to model (117). This would explain the repeated failure of these models to predict clinical efficacy in targeted cancer therapy trials. Despite this, In 2016, 82% of preclinical studies published, employed cell-line derived tumour models (118). On the other hand, genetically engineered mouse models are often developed under the control of a specific oncogenic driver (MYCN, ALK etc) and hence do not effectively recapitulate the diversity of human NBs, which can have many complex potential drivers, including copy number alterations and TERT rearrangements (119). These limitations can be partially overcome by using patient-derived xenograft (PDX) models, which are created by direct transplantation of human tumour material into immunodeficient mice and maintained by *in vivo* passaging (120). Unlike the aforementioned models, PDXs maintain histopathological features, genetic/epigenetic characteristics and anti-cancer drug sensitivities that are similar to their parental patient tumours (121-124). Thus, PDXs represent the only current model system where inter-patient and intra-tumour heterogeneity, critical hallmarks of human cancer, are directly incorporated. Furthermore, because primary human NB tissue is scarce, PDXs represent the most relevant model of native tumour tissue available.

Table 3.1.1 PDXs obtained from the Children's Oncology Group.

PDX	Risk Classification	Phase of Therapy	Sample Type	Stage	*MYCN* Amplification	*ALK* Status	*TERT* mRNA
COG-N-424x	High	DX	Tumour	4	✓	WT	++
COG-N-573x	High	BM	BM	4	✓	WT	++
COG-N-603x	High	DX	Tumour	4	✓	WT	+++
Felix-PDX	High	PD-PM	Blood	4	×	ALK F1245C	++

DX; diagnosis, BM; bone marrow, PD; progressive disease, PM; post-mortem, WT; wild type, +; low, ++; intermediate, +++; high.

With this in mind, four well characterised NB PDXs were obtained from the Children's Oncology Group (COG, https://childrensoncologygroup.org) (Table 3.1). Of these PDXs, three were *MYCN* amplified and one was non-*MYCN* amplified; COG-N-424x (424x), COG-N-573x (573x), COG-N-603x (603x) and Felix-PDX (Felix) respectively. Organoids, approximately 30-60 cells in size, were isolated from these PDXs and grown in 3D ECM cultures. Organoids from all of the PDXs were grown in rat tail collagen type I (C) hydrogels, which were used to model the interstitial ECM, and Matrigel (M) hydrogels, which were used to model the BM. 603x and Felix organoids were also cultured in an additional matrix composed of 50% rat tail collagen type I and 50% Matrigel (MC), which we used to model a disorganised ECM representing the invasive front. Organoids were cultured for five days and imaged using confocal and time-lapse microscopy to directly observe NB cell migration strategies. DIC time-lapse images were taken every 20 minutes for 96 hours. Images were then analysed using FIJI image analysis software to assess growth and morphology, and manually examined for migration and invasion.

3.1.2 PDX organoids are assessed based on size and morphological phenotype

First, we compared the size of all organoids at t0hr in each of the matrices tested (Fig 3.1.1). We found that the initial size of organoids within each population was variable, which was to be expected. Although the extraction of organoids was achieved by the same methodology, we found that the initial size of organoids was dependant on the PDX of origin. Felix organoids were significantly larger in most cases and 603x organoids were significantly smaller than both Felix and 424x at t0hr. Therefore, we decided that comparing the relative growth of organoids for the remaining experiments would be more indicative of the dynamic alterations in organoid phenotypes.

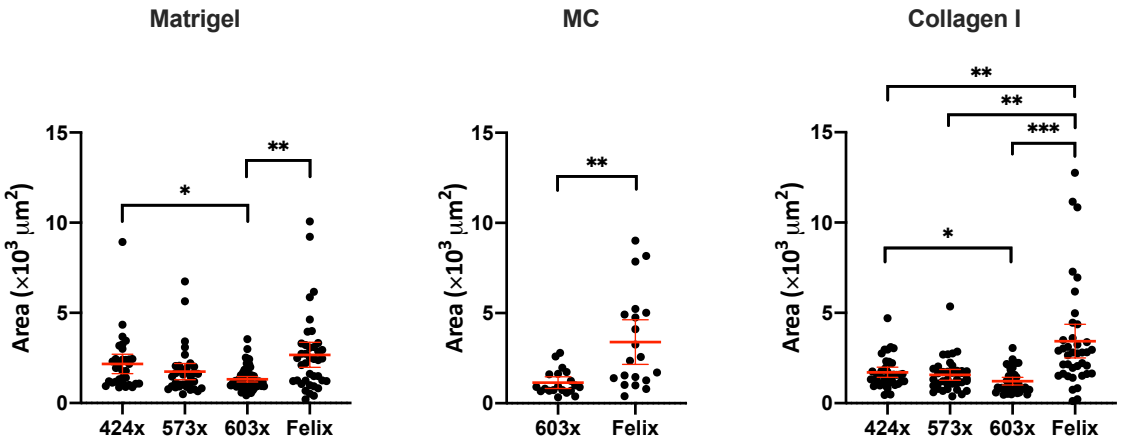

Figure 3.1.1 The size of isolated NB organoids depends on the PDX of origin. Organoids were isolated from four different NB PDXs and embedded in Matrigel or Collagen hydrogels. 603x and Felix organoids were also embedded in MC hydrogels. Images of organoids were captured by DIC microscopy at t0hr and area was measured using FIJI image analysis software. Each dot represents one organoid and error bars indicate mean ± 95% confidence interval. Asterisks indicate statistical significance obtained using Brown-Forsythe ANOVA with T3 Dunnett post-hoc test (*p<0.05, **p<0,01, *** p<0.001).

Next we examined our imaging data and found that NB cells showed distinct cellular behaviours within our organoid populations. We observed cells employing various cellular modes of migration as well non-invasive epithelial-like behaviours. Based on current knowledge of tumour cell migration and invasion, as documented in the literature, we visually classified organoids into six distinct phenotype classifications. Four invasive phenotypes were identified and have been termed, “collective mesenchymal”, “protrusive”, “neuronal” and “elongated”. We have also identified two distinct non-invasive phenotypes,

termed “spheroid” and “cyst” (Figure 3.1.2.1). Organoids classified as spheroid had a round morphology and did not protrude into the local ECM. Cyst organoids were defined as having round morphology with an internal lumen, giving them a cyst-like appearance. We observed cells invading as collective strands with actin-rich protrusions at their tips, indicative of cells at the invasive front with mesenchymal traits and thus termed this phenotype “collective mesenchymal”. Collective strands were also seen in organoids that we termed “elongated”, however in these cases strands were unbranching and cells appeared to migrate in a common direction. NB cells also displayed neuronal-like migratory behaviours in our 3D ECM cultures; organoids containing cells with neurite-like processes that appeared to invade as a collective network with transient cell-cell interactions were termed “neuronal”. Finally, we observed organoids that maintained a round, central cell mass while radially extending long, unbranching, actin-rich protrusions that were neurite-like into the ECM gels; this phenotype was termed “protrusive” (Figure 3.1.2.2). The basis of our phenotype classification is discussed in detail, with reference to current literature in the discussion section.

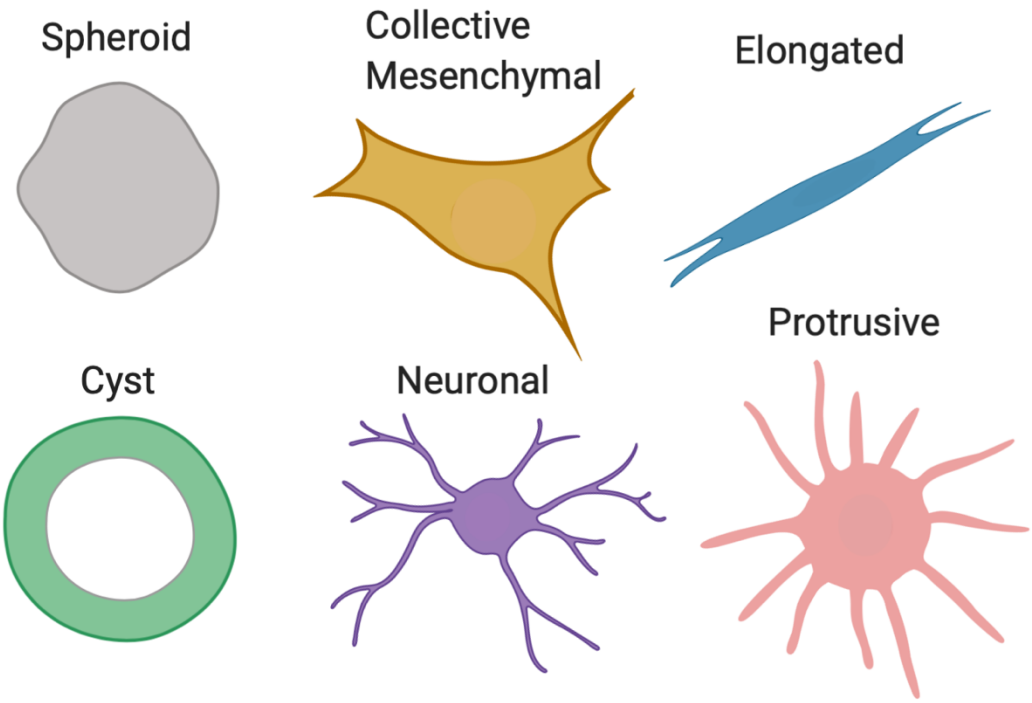

Figure 3.1.2.1 Schematic illustration of distinct organoid morphological phenotypes observed in 3D culture assays. We have identified six distinct phenotypes in NB organoids isolated from PDXs. We termed round organoids with no protrusions "Spheroid" and round organoids containing a lumen "cyst" due to their cyst-like appearance. Cells were observed invading ECM hydrogels as collective strands with actin-rich protrusions (indicative of cells with mesenchymal traits) at the leading edge and thus this phenotype was termed "collective mesenchymal". These organoids contained strands invading in multiple directions. The "elongated" phenotype also displayed collective strand invasion, although multicellular streaming was also seen in these organoids. Cells also appeared to migrate in a common direction leading with long actin-rich protrusions. "Neuronal" organoids invaded collectively as a dispersed network with transient cell-cell contacts, protrusions are neurite-like. The "protrusive" phenotype displays a radial pattern of neurite-like protrusions, where cells are seen migrating individually or are followed loosely by multicellular streams.

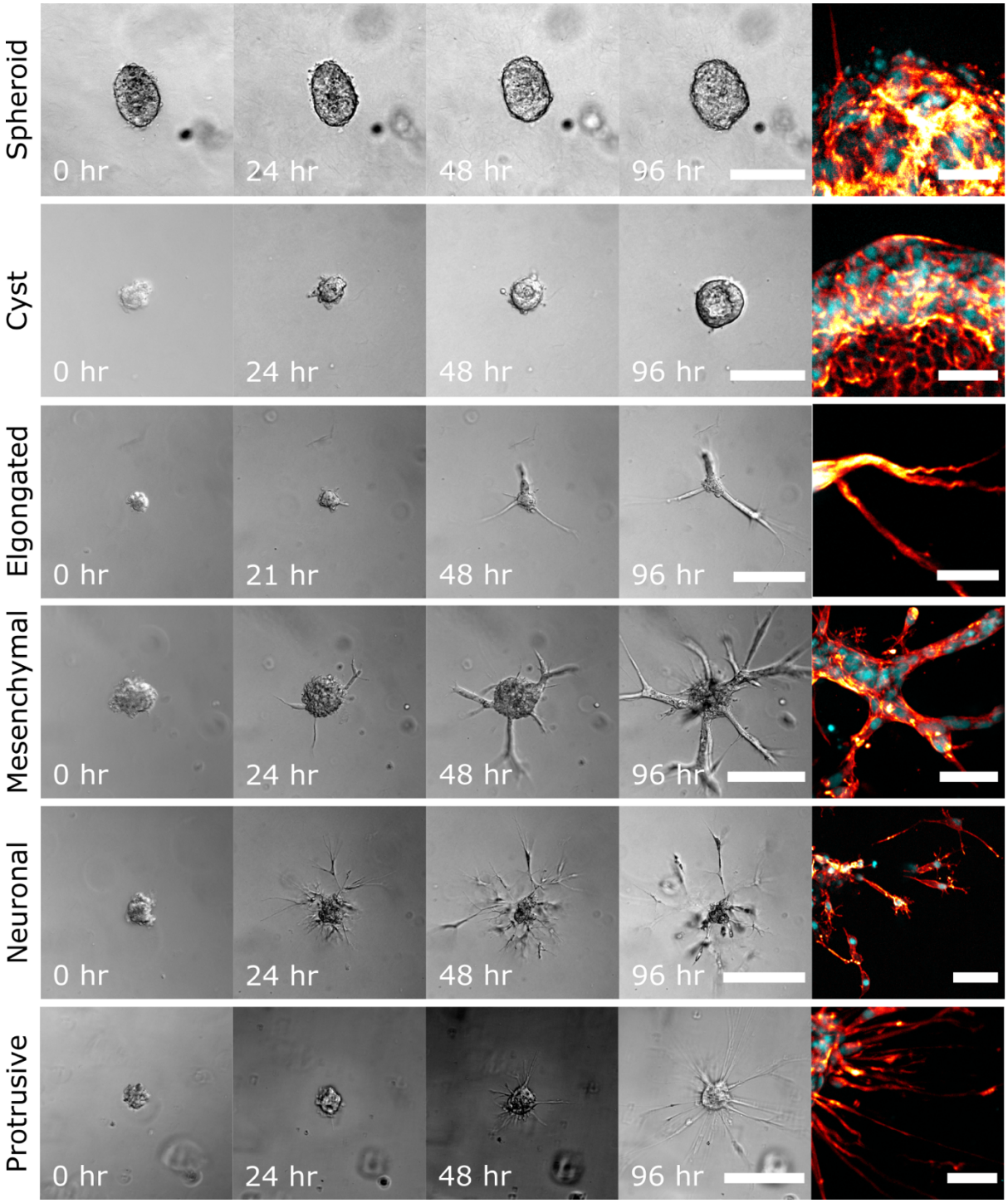

Figure 3.1.2.2 NB organoids are heterogenous and employ a range of distinct migration strategies in 3D invasion assays. Representative DIC time-lapse and confocal images of organoids isolated from Felix-PDX and grown in 3D ECM cultures. Confocal images, taken on day 5 of culture, show nuclei stained with DAPI (cyan) and actin filaments stained with phalloidin (red). Based on morphology NB organoids can be classified as non-invasive (spheroid, cyst) or invasive (elongated, collective mesenchymal, neuronal or protrusive). For spheroid and cyst; scale = 100µm DIC, 30µm confocal. For Elongated scale= 150µm DIC, 30µm confocal. For all remaining images scale =200µm DIC, 50µm confocal.

3.1.3 Organoids isolated from 424x are non-invasive

Organoids that were isolated from 424x PDXs exclusively formed non-invasive spheroid structures in both M and C hydrogels (Fig 3.1.3 A). In C, we found that the circularity of organoids increased over a five-day period and that this increase was statistically significant by t96hr (Fig 3.1.3 C), which confirmed our microscopic observations of spheroid formation. Although the majority of organoids exhibited the same behaviour in M as in C, we did notice a small proportion of spheroid organoids in M that extended singular protrusions into the ECM, however these protrusions were transient and thus the organoids were not classified as invasive. These organoids corresponded to the dots on the plot with lower circularity values (<0.4) in M (Fig 3.1.3 B). The evident decrease in circularity of organoids at t72hr compared to t48hr and subsequent increase at t96hr (statistically significant) supports the transience of the protrusions observed in microscopic images. We also found that organoids grew slowly; the majority of organoids showed less than a 1-fold increase in size after 96 hours (Fig 3.1.3 D).

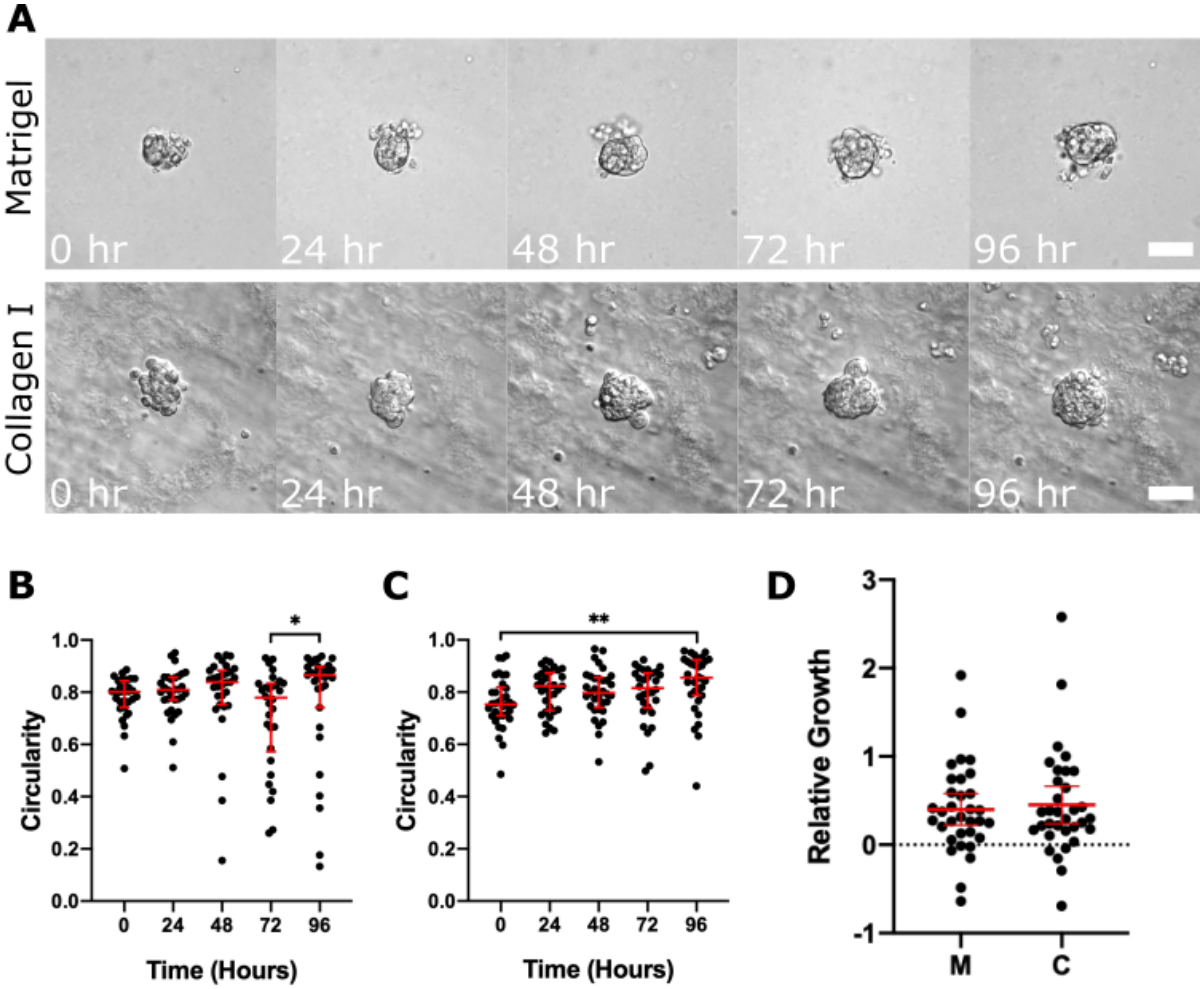

Figure 3.1.3 Organoids isolated from the COG-N-424x PDX are non-invasive in 3D hydrogel cultures. Representative DIC time-lapse images of spheroid organoids in 3D M and C hydrogels (A). Measurements of organoid circularity over five days confirms no significant phenotype changes (a value of 1 represents a perfect circle) in Matrigel (B) or Collagen I (C) gels (Kruskal-Wallis and Dunn's post-hoc tests, horizontal bars indicate median and interquartile range). The relative growth of organoids was calculated by dividing the difference in area between t0hr and t96hr by the area at t0hr and presented on the plot (D) (Unpaired t test with Welch's correction, horizontal bars indicate mean ± 95% confidence interval). For all plots, each dot represents one organoid (n=32 in M, n=35 in C) and asterisks indicate statistical significance (*$p<0.05$, ** $p<0.01$). All scale bars = 50µm.

3.1.4 Invasion was seen in small proportion of organoids isolated from 573x

Organoids isolated from 573x were also predominantly classified as non-invasive due to the fact that spheroid morphologies were predominant in both M (86%) and C (93%) hydrogels after 96 hours in culture (Fig 3.1.4 A, C). However, we identified a small proportion of organoids invading both matrices that were classified as neuronal due to the presence of neurite-like processes (Fig 3.1.4 B, black arrowheads). Interestingly, these organoids began to invade within 24 hours. We also observed one individual organoid in M that was classified as elongated. We observed organoid growth over the course of 5 days in culture but there was no significant difference in relative growth between matrices (Fig 3.1.4 D). Plotting the circularity of organoids over time supports our microscopic observations. The vast majority of organoids begin to form spheroids rapidly, resulting in a statistically significant increase in circularity in both M (Fig. 3.1.4 E) and C (Fig 3.1.4 F) at t24hr compared to t0hr. As the smaller proportion of invasive organoids continue to lose their circularity, the degree of statistical significance declines day after day. This is true in both matrices; however, it is more evident in M due to the greater proportion of invasive organoids in this matrix (14%) compared to C (7%). The populations of invasive organoids are evident on both plots where circularity < 0.3. Overall, the comparison of circularity in organoids between t0hr and t96hr confirms our observations that most 573x organoids form spheroids but that a small proportion display invasive phenotypes in culture. Figure 3.1.4 F shows a neuronal organoid invading M (circularity t0hr=0.65, t24hr=0.038) and spheroid formation in C (circularity t0hr=0.67, t96hr=0.85).

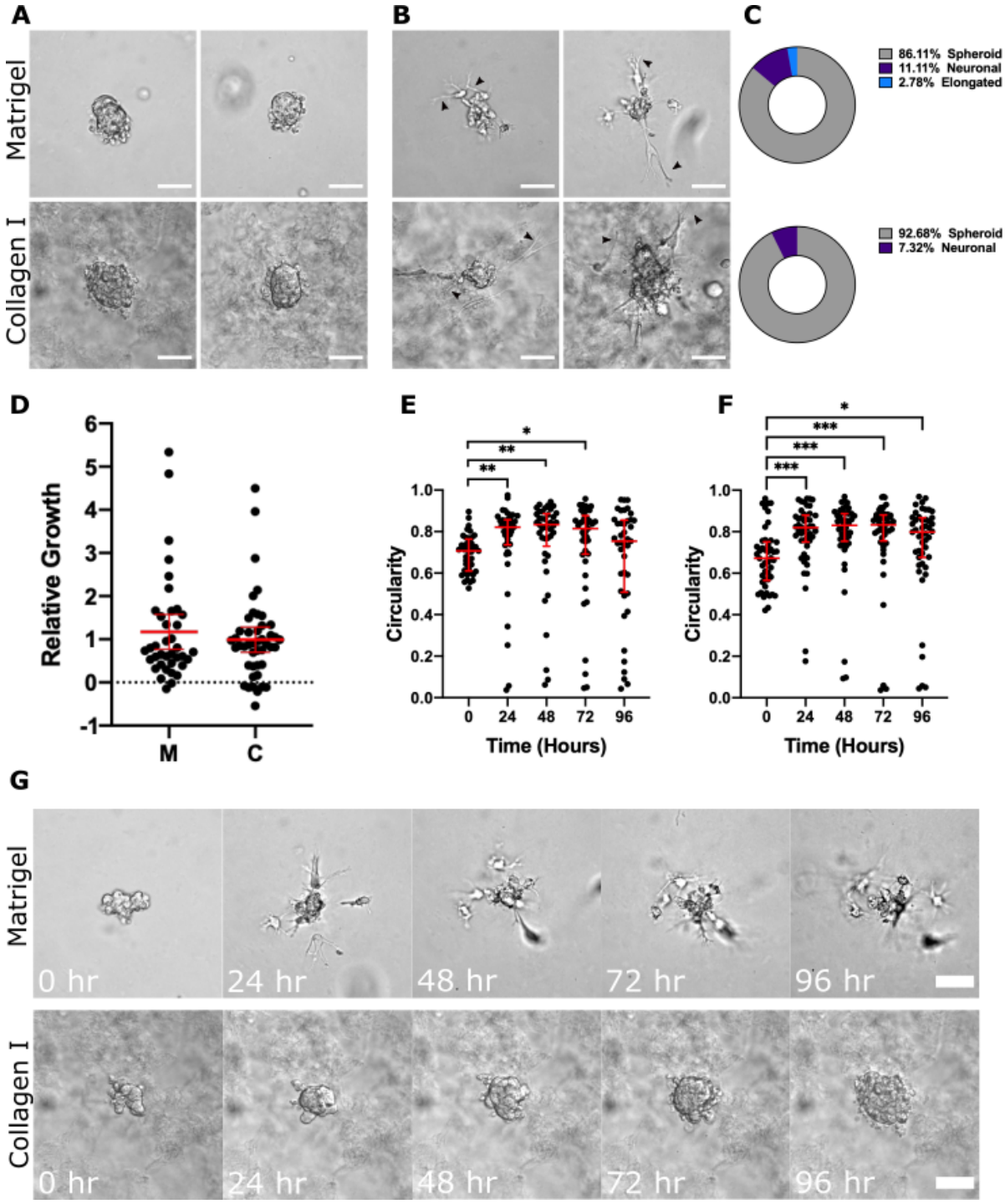

Figure 3.1.4 Organoids isolated from 573x are predominantly non-invasive and the small proportion of invasive organoids favour the neuronal phenotype. Representative DIC images of organoids isolated from 573x in 3D M or C hydrogels. Organoids were characterised as non-invasive spheroids (A) or invasive neuronal organoids (B), representative images were taken at t96hr hours and t24hr hours in culture respectively. Pie-charts represent the proportion of organoids per phenotype classification (C). The relative growth of organoids was calculated by dividing the difference in area between t0hr and t96hr by the area at t0hr and presented on the plot (D) (Unpaired t test with Welch's correction, horizontal bars indicate mean ± 95% confidence interval). Measurements of organoid circularity, where a value of 1 indicates a perfect circle, confirm microscopic observations of changes in morphology in M (E) and C (F) hydrogels (Kruskal-Wallis and Dunn's post-hoc tests, horizontal bars indicate median and interquartile range). G) Representative DIC time-lapse images of a neuronal organoid invasion in M and spheroid formation in C. Black arrowheads indicate neurite-like processes. For all plots, each dot represents one organoid (n=41 in M, n=46 in C) and asterisks indicate statistical significance (*p<0.05, **p<0.01, *** p<0.001, ns; not significant). All scale bars = 50µm.

3.1.5 603x organoids displayed ECM-dependent invasion that was phenotypically heterogeneous

We found that organoids isolated from 603x were more invasive than the previously discussed organoids (424x, 573x). Interestingly we observed far more invasive organoids in matrices that contained M (Fig 3.1.5 A, B). In M, 56% of organoids invaded the gels and in MC we found that 33% of organoids were invasive. In comparison, only 22% of organoids were seen invading their local ECM in C. Figure 3.1.5 G illustrates distinct cellular behaviours in each of our matrices; the collective mesenchymal phenotype was prevalent in M, while spheroid formation was most commonly seen in C. In MC, the presence of M in the MC matrix appears to promote the protrusive phenotype (single cell invasion/multicellular streaming), where 28% of organoids were observed employing this migration strategy. We confirmed our microscopic observations by measuring the circularity of the organoids every 24 hours. The circularity of organoids was significantly decreased ($p<0.01$) in M after only 48 hours (Fig 3.1.5 D, G), compared to in MC where a significant difference is not observed until t72hr (Fig 3.1.5 E, G). In C, we found that organoid circularity followed a different trend whereby an increase in circularity is seen as spheroids form (t0hr-t48hr), followed by a significant decrease as the invasive organoids in the population begin to protrude (t48hr-t96hr) (Fig 3.1.5 F, G). The relative growth of organoids was not found to be significantly different between matrices, however it is clear on the plot that the organoids displaying the largest increase in size (> 5-fold increase) are predominantly found in M (Fig 3.1.5 C). The greatest diversity in organoid phenotypes is also seen in M (6 phenotypes identified) (Fig 3.1.5 A, B); cyst formation, neuronal and elongated organoids were exclusively identified in M. Therefore, we postulate that these organoids display greater phenotypic heterogeneity in response to M.

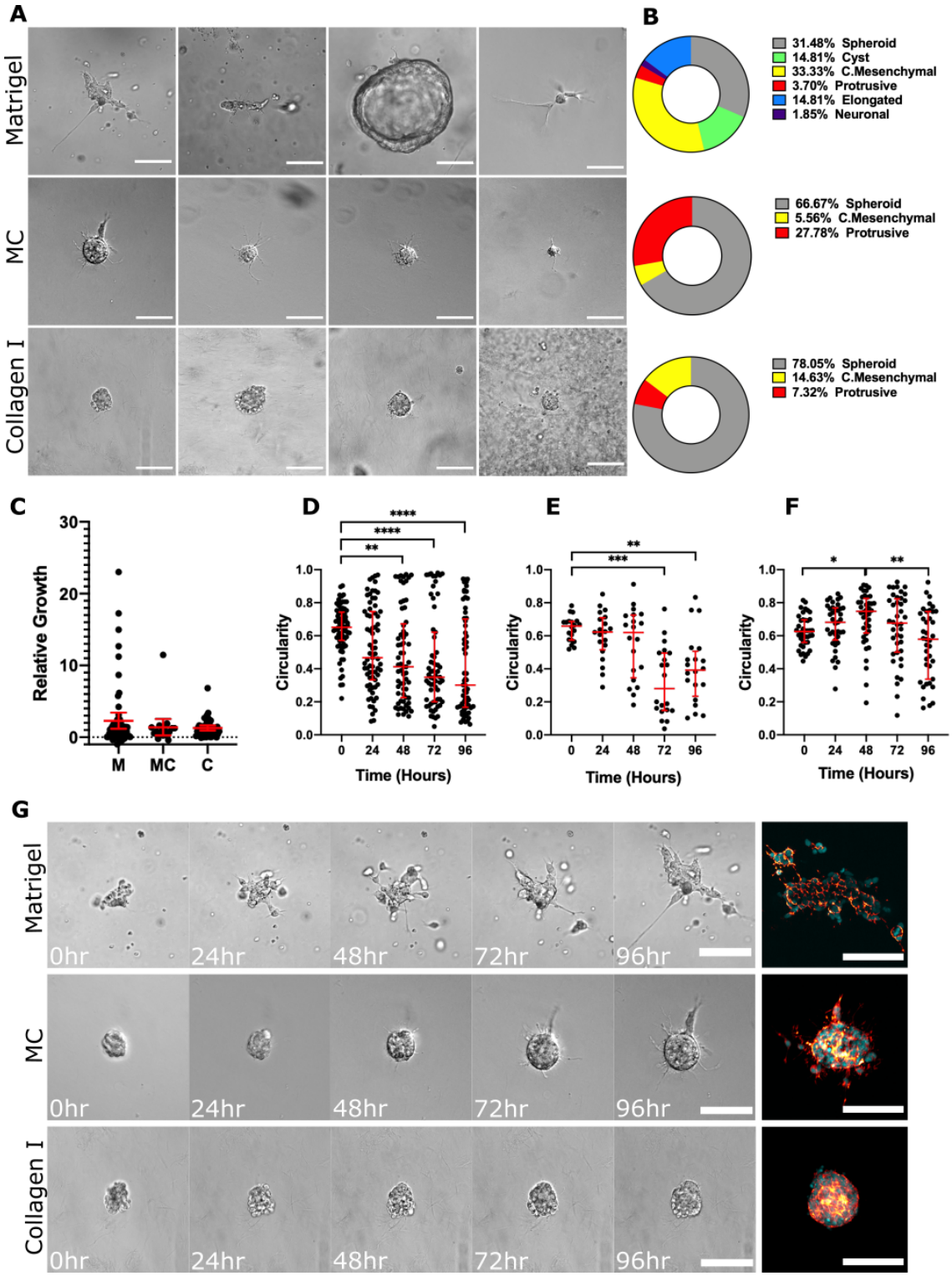

Figure 3.1.5. The local invasion of organoids isolated from 603x is dependent on ECM composition. Representative DIC images of NB organoids after 4 days of culture in 3D hydrogels composed of M, MC or C (A). Pie-charts represent the proportion of organoids per phenotype classification (B). The relative growth of organoids was calculated by dividing the difference in area between t0hr and t96hr by the area at t0hr and presented on the plot (C) (Brown-Forsythe and Welch ANOVA with T3 Dunnett post-hoc test, horizontal bars indicate mean ± 95% confidence interval). Organoid circularity was measured to support microscopic observations of phenotypical changes, where a value of 1.0 indicates a perfect circle, in M (D), MC (E) and C (F) hydrogels (Kruskal-Wallis and Dunn's post-hoc tests, horizontal bars indicate median and interquartile range). G) Representative DIC time-lapse and confocal images of prevalent organoid phenotypes in each of the respective matrices; collective mesenchymal in M, protrusive in MC and spheroid in C. Nuclei are stained with DAPI (cyan) and F-actin is stained with phalloidin (red hot). For all plots, each dot represents one organoid (n=63 in M, n=20 in MC, n=40 in C) and asterisks indicate statistical significance (*p<0.05, **p<0.01, *** p<0.001, ****p<0.0001). All scale bars = 100µm.

3.1.6 Felix organoids displayed ECM-dependent invasion that was phenotypically heterogeneous

Interestingly, organoids isolated from the non-*MYCN* amplified Felix-PDX were also highly invasive in hydrogels containing Matrigel (M, MC). Conversely, in C local organoid invasion was rarely observed (Fig 3.1.6 A, B). 91% of organoids were classified as non-invasive spheroids (74%) or cysts (17%) in C gels, while organoids displayed invasive phenotypes 50% of the time in M and 68% of the time in MC. Again, we observed the broadest range of phenotypes in M (6 phenotypes identified), compared to MC (5 phenotypes) and C (4 phenotypes) (Fig 3.1.6 A, B). We measured the circularity of organoids every 24 hours to confirm our microscopic observations of changes in phenotype. In matrices containing M, we observe similar trends when organoid circularity is plotted. In both M (Fig 3.1.6 D) and MC (Fig 3.1.6 E), a large proportion of organoids have low circularity values (< 0.4) by t48hr. In MC the circularity of organoids is significantly reduced at t72hr and t96hr compared to t0hr. However, statistical significance was not obtained when comparing organoid circularity in M. This can be explained by the almost complete segregation of invasive and non-invasive organoids on the plot after 72 hours. In C, we found no significant difference in organoid circularity over the course of 5 days. Furthermore, the vast majority of organoids maintain high circularity values (> 0.5) at all time points. This confirmed the prevalence of non-invasive spheroid and cyst phenotypes in this matrix. The representative images in Figure 3.1.6 G illustrate a loss of circularity in M (t0hr=0.677, t96hr=0.01) and MC (t0hr=0.672, t96hr=0.054) where invasion occurs, while an increase in circularity is seen in corresponding images of spheroid formation in C (t0hr= 0.53, t96hr=0.888). The mean relative growth of organoids is also significantly larger in M compared to C and it is clear on the plot that the most proliferative organoids are found in M (Fig 3.1.6 C). Representative time-lapse images show a protrusive organoid in M that is 17 times larger at t96hr compared to t0hr (Fig 3.1.6 G). The corresponding representative images in MC and C show the collective mesenchymal (4.4-fold increase in size) and spheroid (2.7-fold increase in size) phenotypes respectively over the same time period.

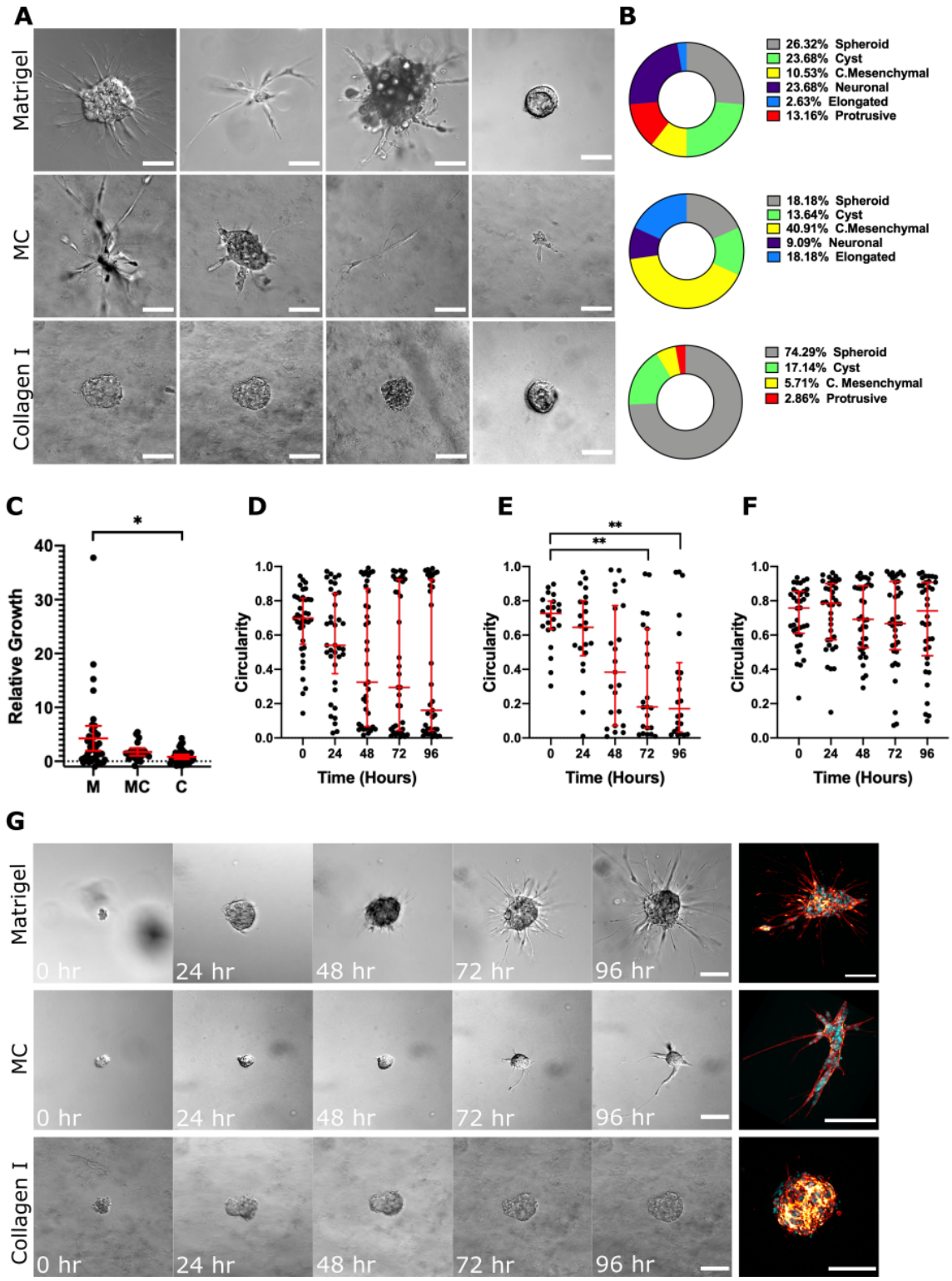

Figure 3.1.6 Invasion of organoids isolated from Felix is dependent on the composition of the matrix. Representative DIC images of organoids isolated from Felix taken at t96hrs in 3D M, MC, or C hydrogels (A). Pie-charts represent the proportion of organoids per phenotype classification (B). The relative growth of organoids was calculated by dividing the difference in area between t0hr and t96hr by the area at t0hr and presented on the plot (C) (Brown-Forsythe and Welch ANOVA with T3 Dunnett post-hoc test, horizontal bars indicate mean ± 95% confidence interval). Plotting the circularity of organoids, where a value of 1.0 indicates a perfect circle, over time supports our microscopic observations of phenotype alterations in M (D), MC (E) and C (F) (Kruskal-Wallis and Dunn's post-hoc tests, horizontal bars indicate median and interquartile range). Representative DIC time-lapse and confocal images of prevalent organoid phenotypes in each of the respective matrices; protrusive in M, collective mesenchymal in MC and spheroid in C. Nuclei are stained with DAPI (cyan) and F-actin is stained with phalloidin (red hot). For all plots, each dot represents one organoid (n=38 in M, n=22 in MC, n=36 in C) and asterisks indicate statistical significance (*p<0.05, **p<0.01, *** p<0.001, ****p<0.0001). All scale bars =100µm.

3.1.7 Nutrient-rich environment is a prerequisite for neuroblastoma invasion

Next we aimed to explore the effects of serum and growth factor presence in the microenvironment on the growth and invasion of NB organoids. All organoids mentioned thus far were supplemented with media containing FBS and basic fibroblast growth factor (bFGF/FGF-2). Therefore, we wanted to investigate whether these nutrients were essential for aggressive NB behaviour. Organoids were isolated from Felix-PDX, embedded in M, MC or C hydrogels and cultured for 96 hours in medium supplemented with either FBS, bFGF or both FBS and bFGF (FBS/bFGF). We then used DIC time-lapse imaging and invasion assays to directly observe organoid behaviour in response to these different microenvironmental conditions. After 96 hours we stained the hydrogels with ethidium homodimer (EHD) to evaluate the viability of our organoids under each of the different microenvironmental conditions.

We found that the presence of FBS and bFGF in the microenvironment promoted the greatest variety of organoid phenotypes in M, MC and C hydrogels. In M, 37% of organoids were classified as invasive in the presence of FBS and bFGF, while only 12% and 13% of organoids were deemed invasive when FBS or bFGF alone were present, respectively. In MC hydrogels, invasion was not observed at all when only bFGF was present and only seen in 13% of organoids cultured in FBS alone. In comparison, 56% of organoids are classified as having an invasive phenotype when supplemented with FBS/bFGF. However, it should be noted that the number of organoids cultured in MC hydrogels was relatively low for this experiment. In C hydrogels, invasive organoids were also absent when only bFGF was added to the culture, while invasion was observed under the other conditions; 20% of organoids invaded their local ECM when cultured with both FBS and bFGF compared to 24% in FBS alone (Fig 3.1.7 A).

The relative growth of organoids shows a similar trend to phenotype classifications, whereby organoids cultured with both bFGF and FBS performed optimally across all matrices (Fig 3.1.7 B). In M and MC, the presence of bFGF alone showed a significant increase in the relative size of organoids compared to that of FBS alone. Conversely, both bFGF and FBS are required to promote the proliferation of NB organoids in C hydrogels. The

majority of organoids supplemented with FBS alone decrease in size, suggesting that cells are dying (Fig 3.1.7 B, organoids below dotted line). We confirmed the presence of non-viable cells using EHD staining (Fig 3.1.7 C). EHD staining also confirmed that organoids grown in media supplemented with both bFGF and FBS performed optimally in 3D invasion assays (Fig 3.1.7 C). Overall, organoids cultured in either M or MC hydrogels with both bFGF and FBS supplements displayed the most aggressive behaviour and are most useful for the study of local NB invasion.

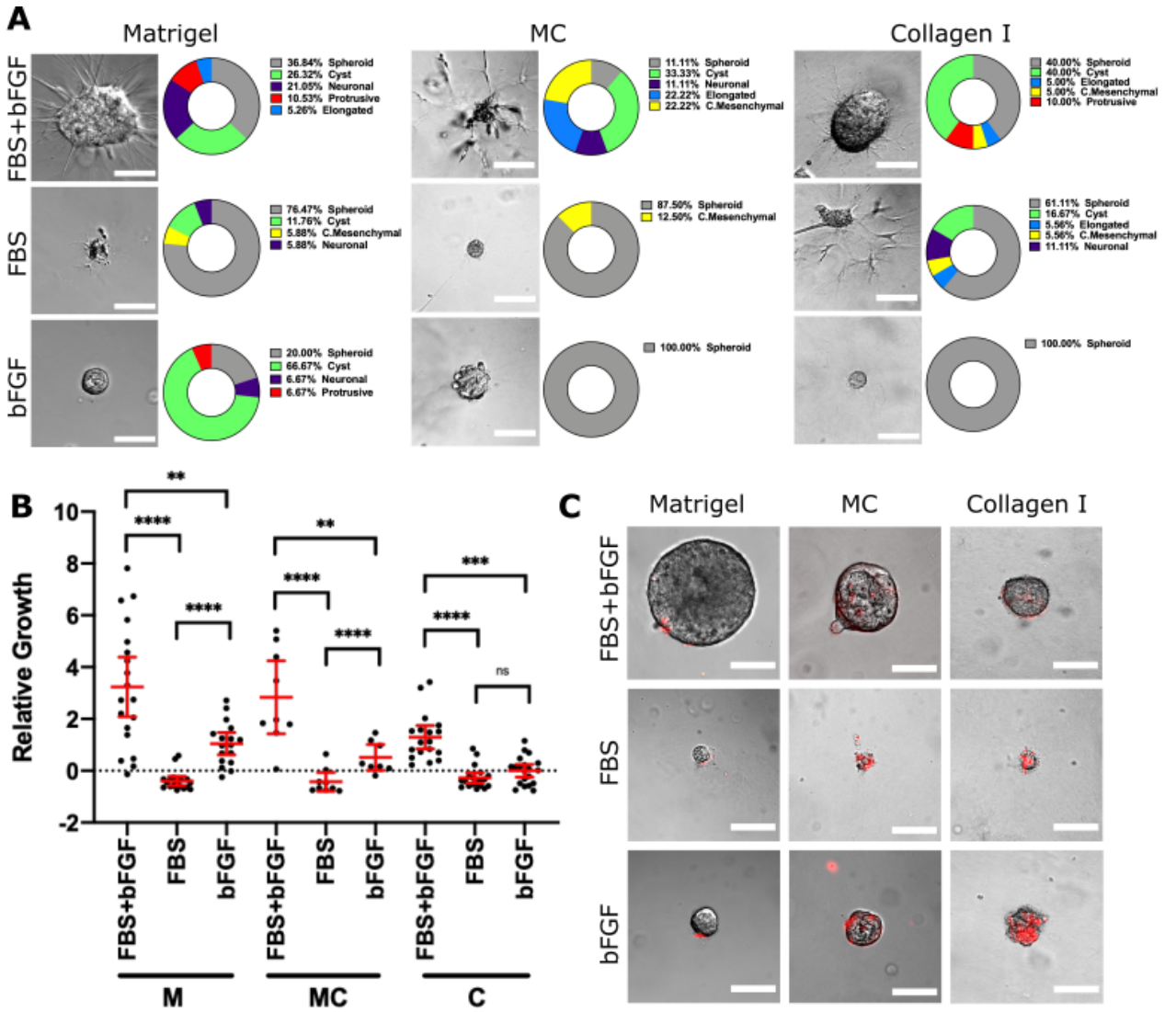

Figure 3.1.7. The invasion and growth of NB organoids is dependent on soluble factors in the microenvironment. A) Representative DIC images taken at t96hr and corresponding pie-charts representing phenotype classifications of organoids isolated from Felix-PDX. Organoids were cultured in M, MC or C in the presence of FBS+bFGF, FBS alone or bFGF alone. The relative growth of these organoids was calculated by dividing the difference in area between t0hr and t96hr by the area at t0hr and presented on the plot (B). C) Representative images of EHD staining (dead cells; red) of organoids at t120hr. Each dot represents the relative growth of one organoid (M: n=19 in FBS/bFGF, n=17 in FBS, n=15 in bFGF. MC: n=9 in FBS/bFGF, n=8 in FBS, n=5 in bFGF. C: n=20 in FBS/bFGF, n=17 in FBS, n=14 in bFGF). Error bars indicate the mean ± 95% confidence interval. Asterisks indicate statistical significance obtained using Brown-Forsythe ANOVA with T3 Dunnett post-hoc test (ns=not significant, ** p<0.01, *** p<0.001, **** p<0.0001). All scale bars = 100µm.

3.1.8 Key Findings

1. Using real-time imaging, organoids isolated from NB PDXs and 3D ECM cultures, we were able to visualise cellular invasion into hydrogels over time and thus we propose an effective model of local NB invasion.

2. isolated from NB PDXs are effective at modelling local tumour invasion in 3D ECM cultures.

3. We found that local invasion of NB organoids was dependent on the PDX of origin as well as the composition of ECM hydrogel.

4. The most invasive organoids were observed in matrices that contained the BME, Matrigel (M and MC).

5. NB organoids display a range of distinct phenotypes in response to different ECM conditions, suggesting the maintenance of intra-tumour heterogeneity; a hallmark of NB.

6. A nutrient-rich environment is a prerequisite for aggressive NB behaviour.

Chapter 3. Results

Chapter 3.2 Exploring the behaviour of NB cell lines in 3D culture assays.

3.2.1 Introduction

As mentioned previously, cultured cancer cell lines are the most widely used *in vitro* models in NB and cancer research in general, primarily due to their availability, reproducibility, low cost and simplicity. Therefore, we decided to assess a panel of NB cell lines in this 3D platform to see if their behaviour would emulate that of the organoids discussed in the previous chapter. We embedded single cells in M, MC and C hydrogels and used DIC time-lapse imaging to directly observe cell dynamics during clonal expansion and local invasion of NB cell clusters. The cell lines evaluated were Kelly, KellyCis83, CHP-212, SH-SY5Y, NB1691 and LAN-1 (Table 3.2.1). We also evaluated the SHEP-Tet21N cell line in later experiments (Chapter 3.4). We found that all cell lines proliferated and formed clusters in each of the 3D hydrogels tested, however invasion of the local ECM was not observed in all cell lines.

Table 3.2.1 Neuroblastoma cell lines, their origin and common genomic alterations.

Cell Line	Origin	MYCN	ALK	TERT
Kelly	Bone Marrow	MNA	F1174L	WT
KellyCis83	Bone Marrow	MNA	F1174L	WT
CHP212	Primary Kidney Mass	MNA	WT	unknown
SH-SY5Y	Bone Marrow	Non-MNA	F1174L	Mutation (C2285)
NB1691	Primary Abdominal Mass	MNA	WT	unknown
SHEP-Tet21N	Bone Marrow	repressible	F1174L	Mutation (C2285)
Lan-1	Bone Marrow	MNA	F1174L	WT

MNA; MYCN amplified, WT; wild type.

We allowed 24 hours after embedding cell lines into ECM gels for clonal expansion and cluster formation to occur. Thus, we first measured the area of selected cell line clusters using FIJI image analysis software at t24hr. Within most populations of cell line clusters there is large variation in size, regardless of the matrix (Fig 3.2.1). There is a clear difference

in size between cell lines, however the trend is consistent across matrices. For instance, CHP-212 are small in size across matrices, suggesting they may remain as single cells or very small clusters. The Lan-1 and KellyCis83 populations contain clusters of various different sizes, however the variation is conserved across matrices.

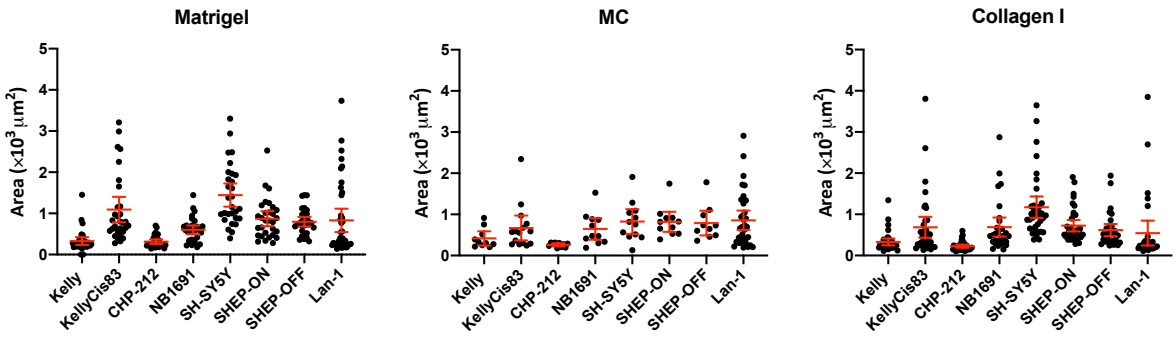

Figure 3.2.1 Comparison of size of clonal NB cell line clusters after 24 hours in 3D ECM cultures. NB cell lines were embedded in Matrigel, MC or Collagen I hydrogels and area was measured using FIJI image analysis software at t24hr to allow time for clonal expansion/cluster formation. Each dot represents one cell cluster. Error bars indicate the mean ± 95% confidence interval.

3.2.2 Cell line clusters can be classified as non-invasive in 3D invasion assays

The Kelly, KellyCis83 and CHP212 cell lines were deemed to be non-invasive in our 3D ECM cultures. These cell lines exclusively formed multicellular spheroids similar to those seen in organoids. These clusters did not extend protrusions into their local ECMs, regardless of composition (Figure 3.2.2 A, B). The spheroid morphologies of these clusters were confirmed by comparing circularity at t24hr and t96hr (Figure 3.2.2 C). In Kelly and KellyCis83, circularity values remain mostly high across matrices over time, confirming our microscopic observations of spheroid cluster morphology. Although, notably we saw a significant decrease in circularity in KellyCis83 in M and MC after 96 hours, no clusters were seen with circularity values < 0.4. We also identified clusters in the CHP-212 as spheroid, however these clusters are slightly more elongated than Kelly and KellyCis83 (Figure 3.2.2 B). Furthermore, CHP-212 clusters are noticeably smaller and potentially remain as single cells in some cases. Thus, circularity values are more sensitive to morphology changes in these clusters, which explains the apparent decrease in circularity seen across matrices (significant in M and C) (Figure 3.2.2 C). KellyCis83 and CHP-212 show no significant difference in relative growth across the three matrices tested. However, Kelly spheroids grow significantly larger in C and MC compared to M gels (Figure 3.2.2 D).

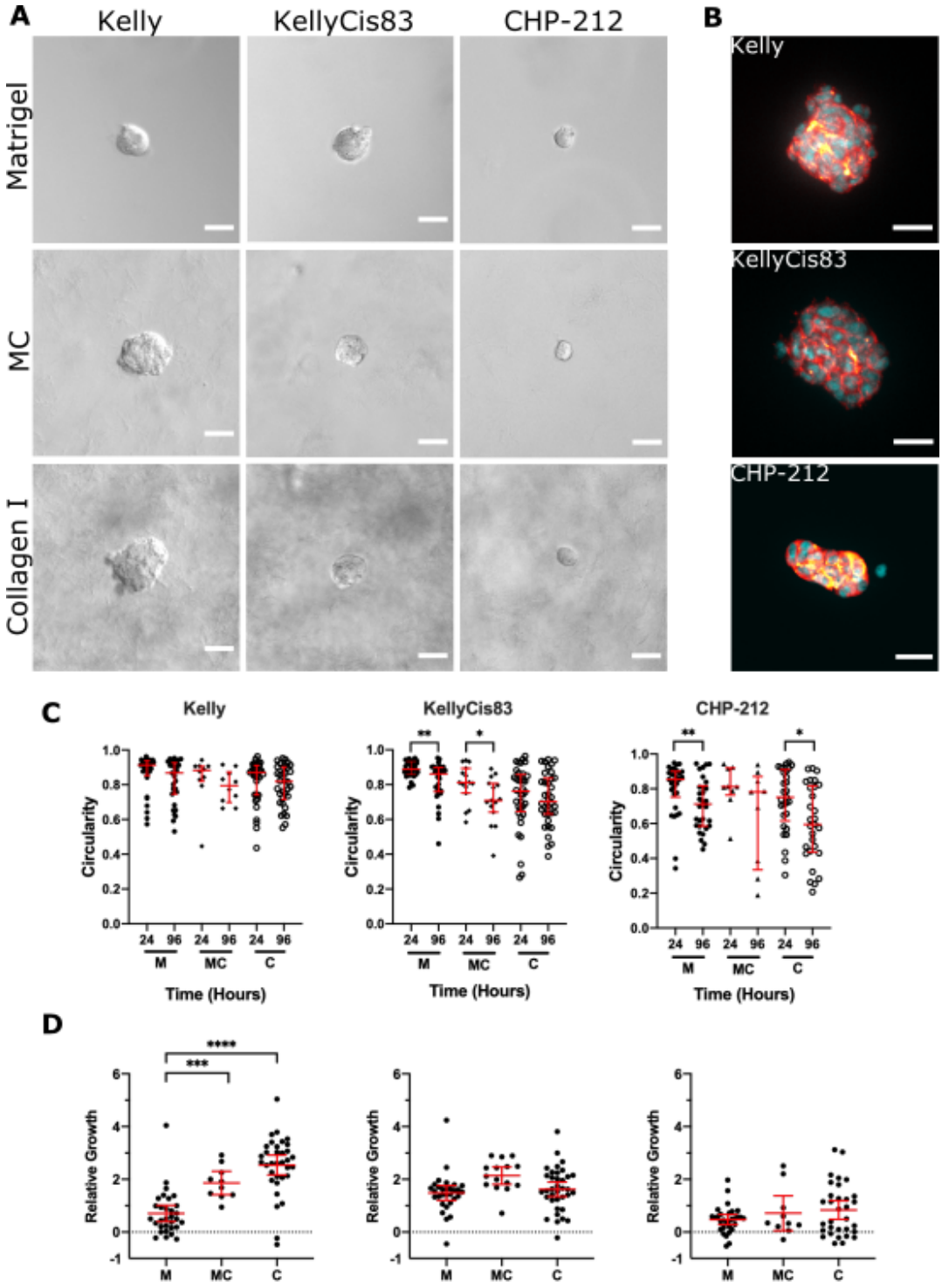

Figure 3.2.2 Kelly, KellyCis83 and CHP-212 cell clusters exclusively form non-invasive spheroids in 3D ECM cultures. A) Representative DIC images of Kelly, KellyCis83 and CHP-212 cell line clusters taken at t96hr in Matrigel, MC and Collagen I hydrogels. B) Representative confocal images of Kelly, KellyCis83 and CHP-212 cell clusters, nuclei stained with DAPI (cyan) and F-actin stained with phalloidin (red hot). The circularity of cell clusters, where a value of 1.0 indicates a perfect circle, was measured to confirm no significant phenotypic changes indicative of invasion; circularity values at t24hr and t96hr in M, MC and C are shown on the same plot for each cell line (C) (Mann-Whitney tests, horizontal bars represent median and interquartile range). The relative growth of cell clusters was calculated by dividing the difference in area between t96hr and t24hr by the area at t24hr and presented on plots corresponding to each cell line (D) (Brown-Forsythe ANOVA with T3 Dunnett post-hoc tests, horizontal bars represent mean ± 95% confidence intervals). For all plots, each dot represents one cluster (Kelly; n=31 in M, n=10 in MC, n=30 in C, KellyCis83: n=30 in M, n=15 in MC, n=36 in C, CHP-212: n=30 in M, n=9 in MC, n=29 in C) and asterisks indicate statistical significance (*p<0.05, *** p<0.001, **** p<0.0001). There is no statistical significance unless indicated on the plots. All scale bars = 30µm.

3.2.3 NB1691 form transient protrusions suggestive of cluster migration

The invasive phenotype observed in clonal NB1691 cell clusters was not similar to any of those seen in organoids. However, due to their transient protrusions, we suspect that these small cell clusters are capable of migrating through the matrices as a group and hence we have classified them as collective mesenchymal (Figure 3.2.3 A, B). Due to their small size it appears that clusters migrate in their entirety, rather than branching out into the ECM. That being said, the majority of clusters were classified as non-invasive spheroids in M (82%) and C (68%). In contrast, the majority of clusters were deemed invasive in MC, however the sample size was small in this population (n=8). The presence of transient protrusions in these cell clusters can also be appreciated when measuring circularity. In M, many clusters lose circularity at t72hr, however at t96hr the majority regain their round shape (Figure 3.2.3 C). This is also seen when statistically comparing circularity of the populations as a whole; after 72 hours circularity is significantly reduced ($p<0.0001$), however after 96 hours the decrease in circularity is less significant compared to t24hr ($p<0.001$). Similarly in C, a more significant decrease in circularity was obtained at t72hr ($p<0.01$) compared to t96hr ($p<0.05$) (Figure 3.2.3 E). Furthermore, this trend is also evident between t24hr and t48hr in C, where a proportion of clusters with low circularity values (<0.4) is present at t24hr but have regained a more spheroid morphology by t48hr. Although less prevalent in MC, this trend can still be appreciated (Figure 3.2.3 D). Time-lapse images also illustrate these trends and correspond to the time points outlined above (Figure 3.2.3 A), for instance the transient protrusions in M at t72hr and in C at t24hr and t72hr. The relative growth of cell clusters was significantly increased in C compared to M (Figure 3.2.3 F). Figure 3.2.3 G shows a representative confocal image confirming that NB1691 cells do migrate as clusters and not only as single cells.

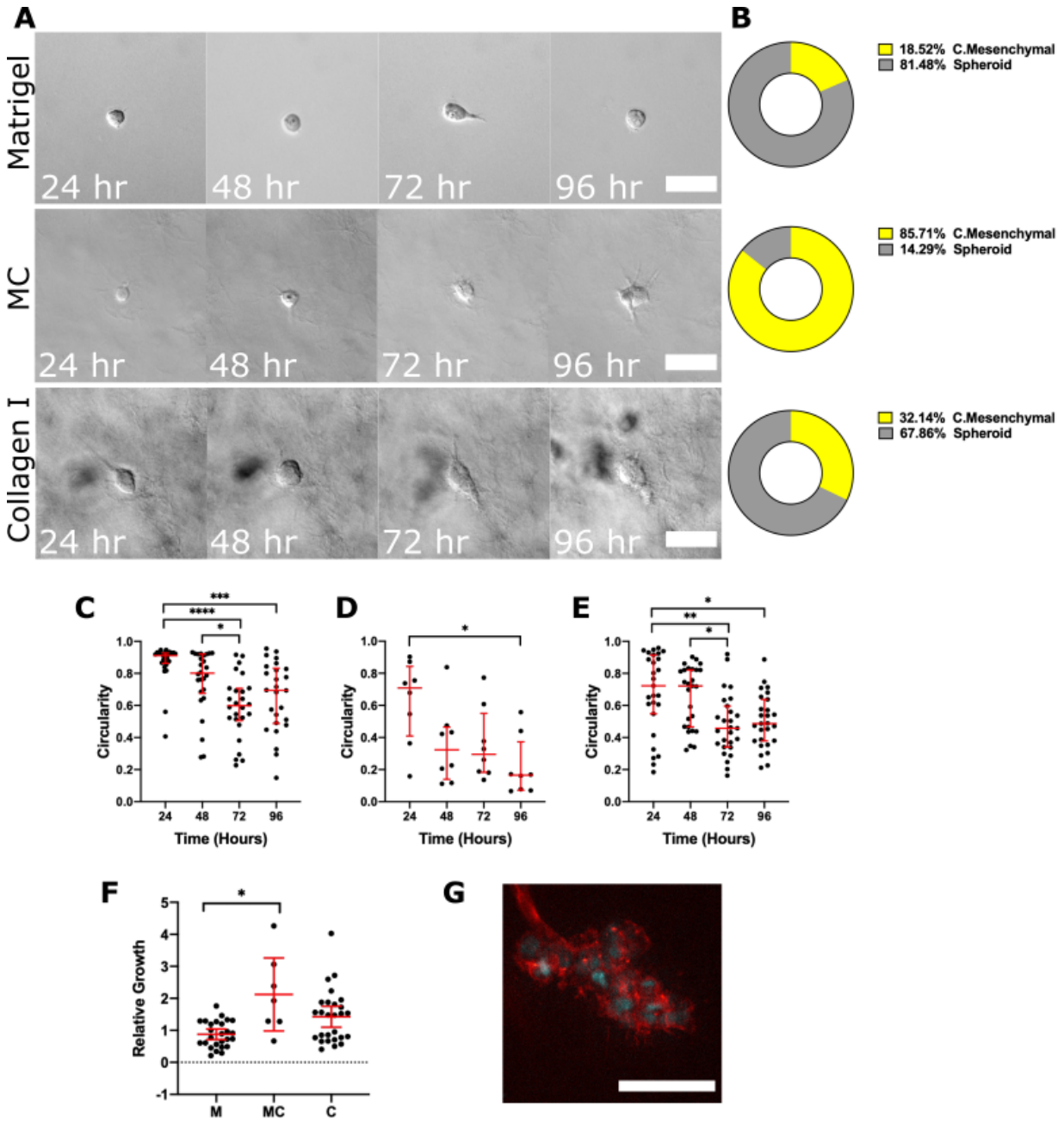

Figure 3.2.3 NB1691 cells migrate as small clusters in 3D ECM cultures, regardless of matrix composition. A) Representative DIC time-lapse images of clonal NB1691 cell clusters migrating collectively in 3D ECM cultures composed of either M, MC or C. B) Pie-charts represent the proportion of cell clusters per phenotype classification. The circularity of cell clusters, where a value of 1.0 indicates a perfect circle, was measured every 24 hours to confirm microscopic observations of phenotype alterations in M (C), MC (D), and C (E) hydrogels (Kruskal-Wallis and Dunn's post-hoc tests, horizontal bars represent median and interquartile range). F) The relative growth of cell clusters was calculated by dividing the difference in area between t96hr and t24hr to the area at t24hr and presented on the plot (Brown-Forsythe ANOVA with T3 Dunnett post-hoc tests, horizontal bars represent mean ± 95% confidence intervals). G) Representative confocal image of an NB1691 cell cluster in an MC hydrogel, nuclei are stained with DAPI (cyan) and F-actin is stained with phalloidin (red hot).On all plots, each dot represents one cell cluster (n=26 in M, n=8 in MC, n=27 in C) and asterisks indicate statistical significance (*p<0.05, ** p<0.01, ***p<0.001, ****p<0.0001). All scale bars = 50µm.

3.2.4 Invasion of SH-SY5Y cell line clusters is collective and independent of ECM composition

In the SH-SY5Y cell line, clusters were predominantly identified as invasive in all three matrices; 61% in M, 80% in MC and 95% in C (Fig 3.2.4 B). Cells exclusively employed the collective mesenchymal mode of invasion, which was identified by the presence of multicellular branches with protrusive tips (Fig 3.2.4 A, G, arrowheads). We measured the circularity of cell clusters to confirm our microscopic observations of phenotypic changes. In M and MC hydrogels, cells begin to invade their local ECM before t48hr, whereas in M the beginning of invasion appears delayed until approximately t72hr (Fig 3.2.4 A). This trend can also be seen when circularity values of cell clusters are plotted. In M the circularity of clusters is significantly decreased at t96hr compared to t48hr and t72hr confirming our microscopic observations (Fig 3.2.4 C). In C, a statistically significant decrease in circularity was seen at all time points compared to t0hr (Fig 3.2.4 E). Imaging data shows the same trend in MC (Fig 3.2.4 A), however no statistical significance was obtained when comparing circularity of cell clusters (Fig 3.2.4 D), however by t48hr most of the clusters can be seen within the lower limits of the plot (circularity <0.4) confirming their invasive phenotype. The lack of statistical significance was likely due to the small sample size (n=11) and the fact that a proportion of clusters had already begun to invade at t24hr, hence the low circularity values on the plot at this time point. Furthermore, the trend of decreasing circularity over time can still be appreciated on the plot. The mean relative growth of cell clusters was significantly increased in C compared to M hydrogels (Fig 3.2.4 F).

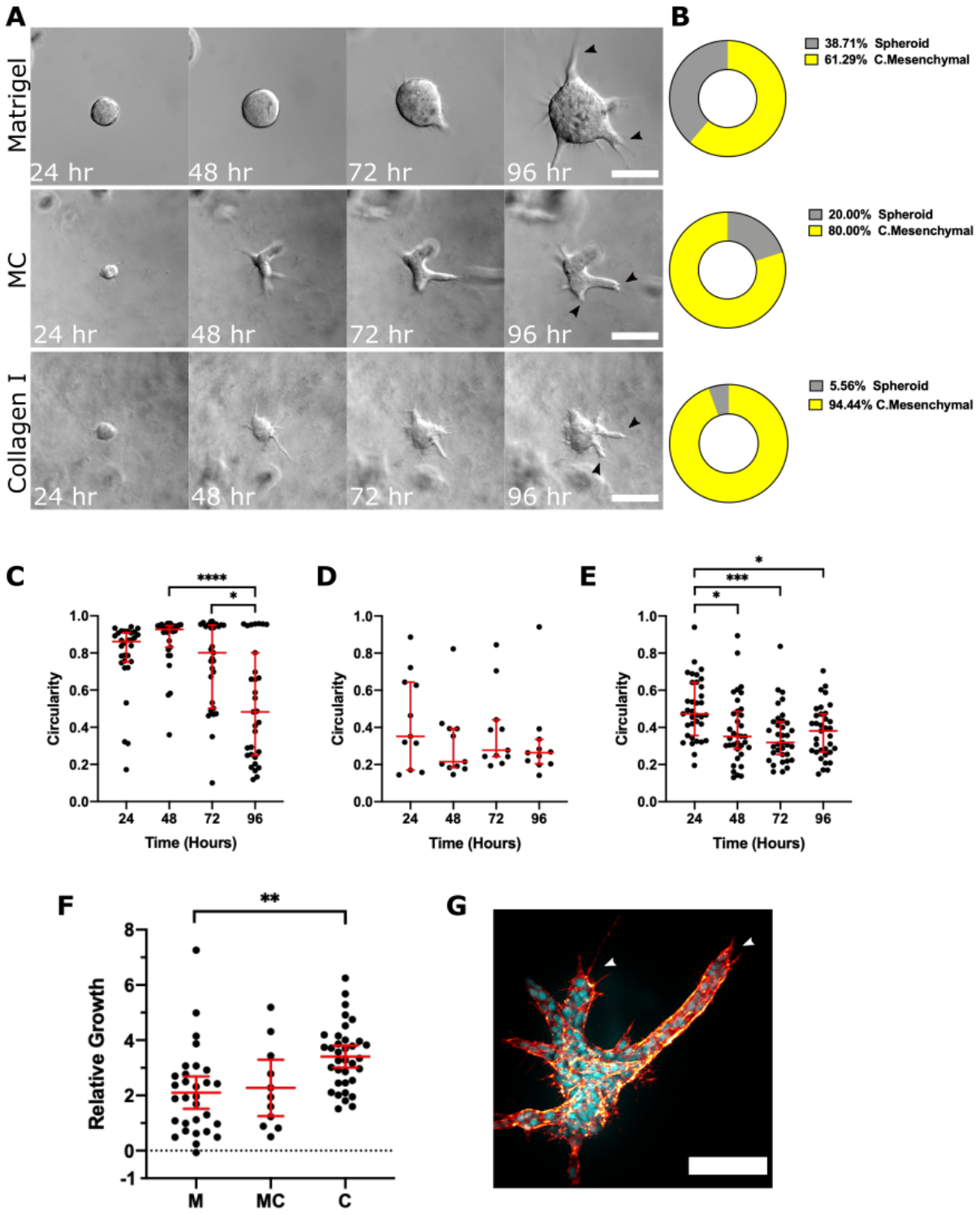

Figure 3.2.4 SH-SY5Y cells invade 3D ECM cultures collectively, regardless of matrix composition.
A) Representative DIC time-lapse images of SH-SY5Y cell clusters collectively invading (black arrowheads) 3D ECM cultures composed of either M, MC or C. B) Pie-charts represent the proportion of cell clusters per phenotype classification. The circularity of cell clusters, where 1.0 indicates a perfect circle, was measured every 24 hours to confirm microscopic observations of phenotypic alterations in M (C), MC (D), and C (E) hydrogels (Kruskal-Wallis and Dunn's post-hoc tests, horizontal bars represent median and interquartile range). F) The relative growth of cell clusters was calculated by dividing the difference in area between t96hr and t24hr to the area at t24hr and presented on the plot (Brown-Forsythe ANOVA with T3 Dunnett post-hoc tests, horizontal bars represent mean ± 95% confidence intervals). G) Representative confocal image of an SH-SY5Y cluster collectively invading an MC hydrogel, nuclei are stained with DAPI (cyan) and F-actin is stained with phalloidin (red hot). Each dot represents one cell cluster (n=30 in M, n=11 in MC, n=34 in C) and asterisks indicate statistical significance (* $p<0.05$, ** $p<0.01$, *** $p<0.001$, **** $p<0.0001$). All scale bars = 100µm.

3.2.5 The invasion of Lan-1 cells is neuronal in nature and ECM-dependent

The behaviour displayed by clusters of Lan-1 cells was more recapitulative of the behaviour that we observed in NB organoids compared to the previously discussed cell lines, whereby invasion was more commonly observed in matrices containing M (Fig 3.2.5 A, B). Clonal Lan-1 cell clusters were predominantly classified as invasive neuronal cell clusters in M (73%) and MC (81%), whereas clusters mostly formed non-invasive spheroids in C (82%) (Fig. 8 A, B). Measuring the circularity of Lan-1 clusters confirmed our microscopic observations of changes in cluster morphology where the majority of clusters have a circularity value of <0.3 in M (Fig 3.2.5 C) and MC (Fig 3.2.5 D) compared to >0.5 in C (Fig 3.2.5 E) by t96hr. In C, clusters maintained relatively constant circularity values over time and no statistical significance was found, confirming our microscopic observations of spheroid formation being favoured in this matrix. Although Lan-1 clusters are highly invasive in M, statistical significance was not obtained when comparing circularity of the entire population of clusters. This is due to the fact that the majority of clusters had already begun to change morphology at t24hr, which explains the large proportion of clusters with low circularity values (< 0.4) at this time point (Fig 3.2.5 C). A large proportion of clusters in MC also had low circularity values at t24hr, however the overall circularity of the population continued to decrease significantly over time (Fig 3.2.5 D). Because single cells were embedded in our hydrogels, we can assume that clusters would have a round morphology at t0hr and that the decrease in circularity between t0hr and t24hr would be more significant than the decrease seen between t24hr and t48hr. This is illustrated in Figure 3.2.5 A, where the representative organoids in M and MC have clearly begun invading the local ECM at t24hr and have circularity values of 0.114 and 0.112 respectively. At t96hr the clusters have circularity values of 0.03 in M and 0.058 in MC. In comparison the representative cluster in C has a circularity value of 0.934 at t24hr and 0.941 at t96hr. The relative growth of cell clusters is significantly larger in MC compared to C and while statistical significance was not found between M and C, there are more clusters in M with a >2-fold increase in size compared to C (Fig 3.2.5 F).

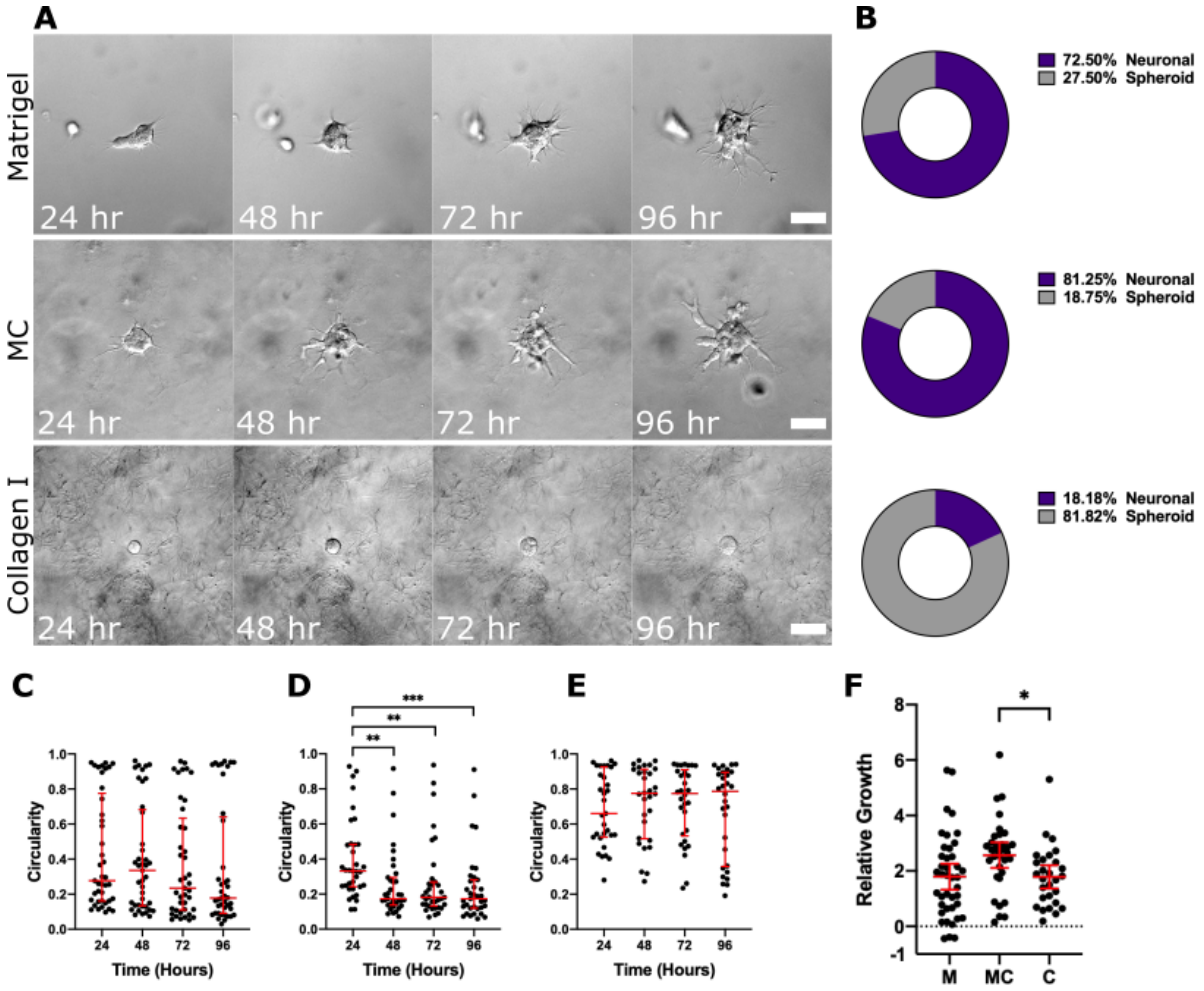

Figure 3.2.5 Lan-1 cell clusters display collective neuronal invasion that is ECM-dependent. A) Representative DIC time-lapse images of Lan-1 cell clusters classified as neuronal in M and MC and as spheroid in C hydrogels. B) Represents the proportion of clusters per phenotype classification. The circularity of cell clusters, where 1.0 indicates a perfect circle, was measured every 24 hours to confirm microscopic observations of phenotypic alterations in M (C), MC (D) and C (E) (Kruskal-Wallis and Dunn's post-hoc tests, horizontal bars represent median and interquartile range). The relative growth of cell clusters was calculated by dividing the difference in area between t24hr and t96hr by the area at t24hr and presented on the plot (F)(Brown-Forsythe ANOVA with T3 Dunnett post-hoc tests, horizontal bars represent mean ± 95% confidence intervals). For all plots, each dot represents 1 cell cluster (n=41 in M, n=35 in MC, n=34 in C) and asterisks indicate statistical significance (* $p<0.05$, ** $p<0.01$, *** $p<0.001$). All scale bars = 50µm.

3.2.6 Key Findings

1. Clonal clusters of NB cell lines did not display the same phenotypic diversity as organoids isolated from PDXs in the 3D model of local invasion.

2. Cell lines can be classified as invasive (Lan-1, SH-SY5Y) or non-invasive (Kelly, KellyCis83, CHP-212) based on their behaviour in 3D *ex vivo* invasion assays.

3. Invasion of cell lines did not depend on ECM composition in most cases. However, Lan-1 invaded matrices containing Matrigel more often.

Chapter.3. Results

Chapter 3.3 Investigating whether organoids isolated from SH-SY5Y xenografts can recapitulate the invasive features seen in patient-derived NBs.

3.3.1 Introduction

Thus far we have shown that organoids isolated from NB PDXs display greater phenotypic diversity compared to NB cell lines when grown in 3D ECM cultures. We suspected that this may potentially be due to the presence of the pre-existing cell-cell and cell-matrix interactions in an organoid. When cells are grown in 2D on plastic substratum they are deprived of many of these crucial interactions as well as the natural 3D architecture present in a tumour mass. This leads to changes in cell differentiation, cell signalling, morphology, division, response to stimuli, metabolism, polarity and behaviour (125, 126). With this in mind we hypothesised that re-introducing SH-SY5Y cells to a 3D *in vivo* tumour microenvironment would induce a NB cell line to display a broader range of invasion strategies.

We selected the SH-SY5Y cell line for this experiment because of its invasive nature in the previous tests. We grew SH-SY5Y xenografts and isolated organoids from the resulting tumours (SH-SY5Y organoids) for 3D invasion assays. We embedded SH-SY5Y organoids in either M, MC or C hydrogels and used DIC time-lapse microscopy to observe cellular strategies of invasion over the course of 5 days in culture. We stained sections of an SH-SY5Y tumour and Felix-PDX to compare their histopathological appearance and similarities were observed (Fig 3.3.1). That being said, cells in the SH-SY5Y tumour do appear more dispersed than in the Felix-PDX, perhaps indicating that cell-cell contacts are more numerous in our PDX. Organoids isolated from the SH-SY5Y tumour were similar in size to those isolated from Felix-PDX (Fig 3.3.1), which were shown earlier to be the largest of our organoids (Chapter 3.1, Fig 3.1.1).

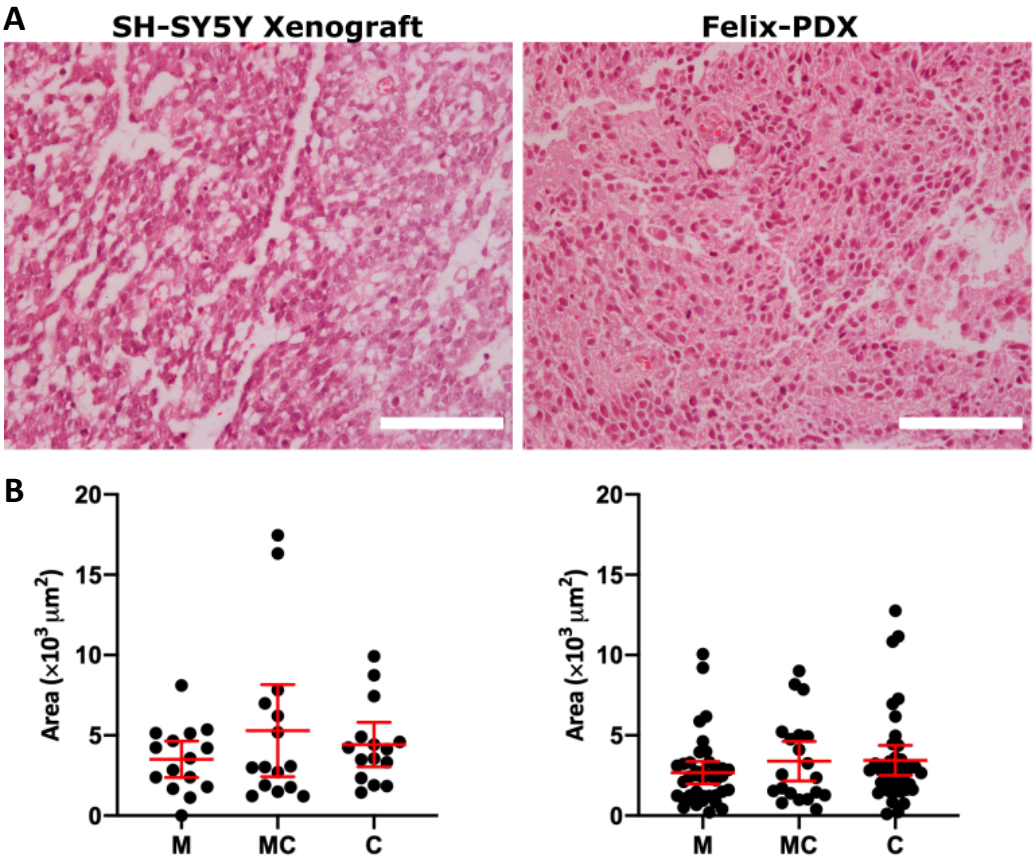

Figure 3.3.1. Comparison of a NB cell line-derived xenograft and patient-derived xenograft and the organoids they yield. A) Representative Hematoxylin and Eosin (H&E) staining of a sectioned SH-SY5Y xenograft and Felix PDX. DIC images were taken of organoids isolated from these tumours at t0hr in M, MC and C hydrogels, their area was calculated using FIJI image analysis software and plotted on the graphs (B). Each dot represents one organoid (SH-SY5Y; n=15 in all matrices, Felix; n=39 in M, n=20 in MC, n=39 in C) and error bars show mean ± 95% confidence interval.

3.3.2 SH-SH5Y organoids display a distinct cellular strategy of invasion in response to an *in vivo* TME.

The behaviour of these organoids in a 3D microenvironment was distinct from that of the SH-SY5Y cell line clusters discussed in chapter 3.2. In M we saw that the majority of SH-SY5Y organoids (76%) resembled the protrusive phenotype that we described in organoids isolated from PDXs (Fig 3.3.2 A-C). In MC, organoids predominantly invaded employing the collective mesenchymal invasion strategy (58%), however we also identified an elongated organoid as well as a number of protrusive organoids (Fig 3.3.2 A, B). Unlike cell line clusters, SH-SY5Y organoids were predominantly non-invasive in C, where 53% of organoids formed spheroids with no protrusions. However, we did observe invasive organoids in C that employed both the protrusive and collective mesenchymal strategies of invasion (Fig 3.3.2 A, B). Measuring the circularity of organoids confirmed our microscopic observations of phenotypical changes; In M the vast majority of organoids have lost their spheroid morphology and are considered invasive at t96hr, this is reflected on the plot (Fig 3.3.2 E) where the majority of organoids have a circularity value of < 0.4 at this time point. The loss of circularity within this organoid population is statistically significant at t96hr ($p<0.001$) and t120hr ($p<0.0001$) compared to t0hr. A similar trend is also seen in MC, where circularity values are significantly lower at t120hr compared to all other time points, excluding t96hr (Fig 3.3.2 F). In C matrices we did not identify as many invasive organoids and this is reflected on the plot (Fig 3.3.2 G) where the variation in organoid circularity is much higher than in M and MC at t120hr. Circularity values were significantly lower at t120hr compared to t0hr ($p<0.05$), however there was greater significance at t48hr ($p<0.01$) and t72hr ($p<0.001$) compared to t0hr, indicative of organoids forming spheroids (increase in circularity between t0hr and t48hr) initially before beginning to protrude after 72 hours. While invasive organoids were present in C matrices, they appear less aggressive than in M and MC (Fig 3.3.2 H). In terms of growth, we observed an approximate 2.5-fold increase in the size of SH-SY5Y organoids over a five-day period and there was no significant difference in growth between matrices (Fig 3.3.2 D).

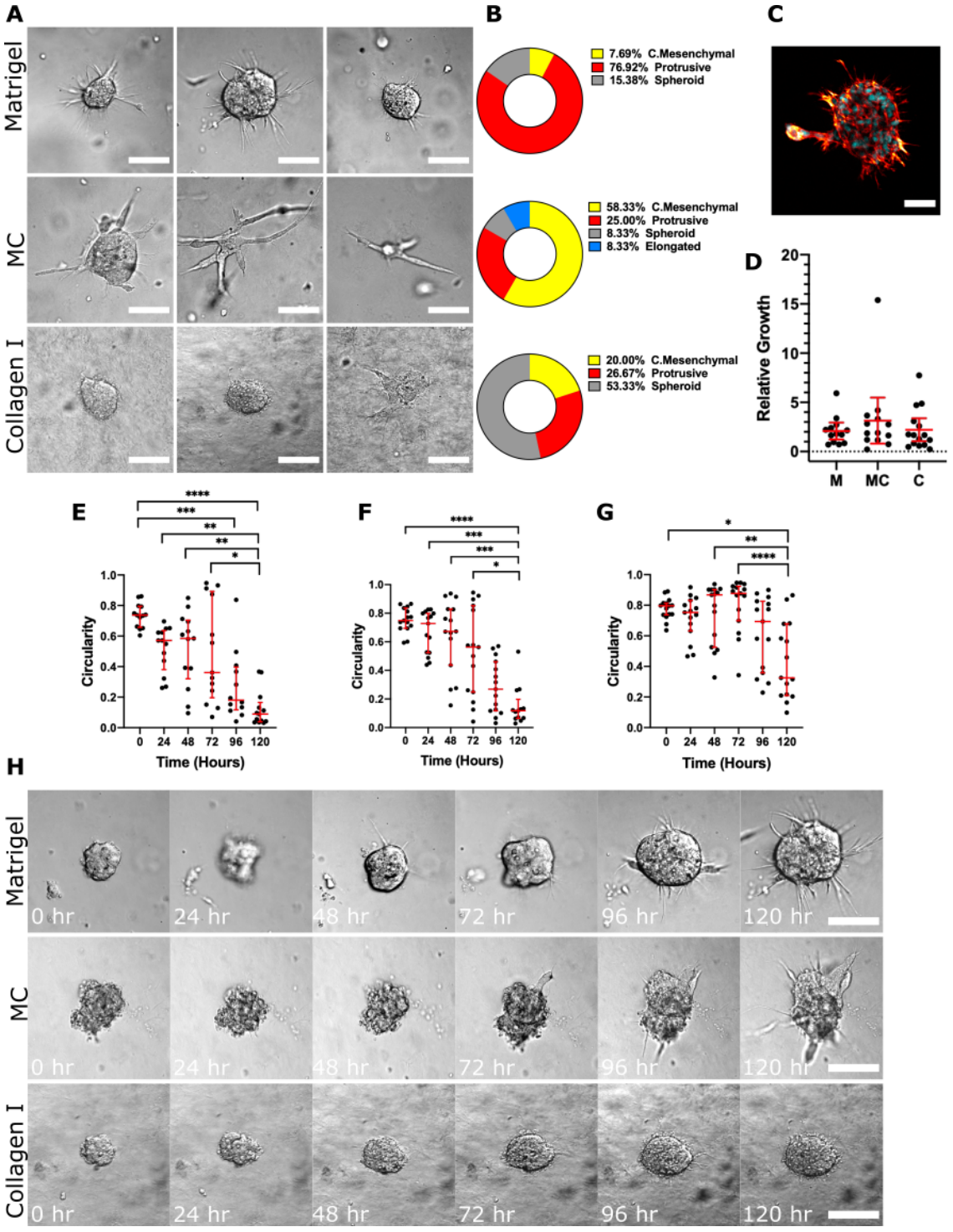

Figure. 3.3.2 The invasive behaviour displayed by SH-SY5Y cells is altered in response to an *in vivo* tumour microenvironment. Representative DIC images of organoids isolated from SH-SY5Y xenografts after 5 days of culture in 3D M, MC, or C hydrogels (A). Pie-charts represent the proportion of organoids per phenotype classification (B). C) Representative confocal image of a "protrusive" SH-SY5Y organoid in M; nuclei are stained with DAPI (cyan) and F-actin is stained with phalloidin (red hot). The relative growth of organoids was calculated by dividing the difference in area between t0hr and t96hr by the area at t24hr and presented on the plot (D) (Brown-Forsythe ANOVA with T3 Dunnett post-hoc tests, horizontal bars represent mean ± 95% confidence intervals). Organoid circularity, where a value of 1.0 indicates a perfect circle, was measured to support microscopic observations of phenotypical changes in M (E), MC (F) and C (G) hydrogels (Kruskal-Wallis and Dunn's post-hoc tests, horizontal bars represent median and interquartile range). H) Representative DIC time-lapse images of protrusive invasion in M and C and collective mesenchymal invasion in MC. On all plots, each dot represents one organoid (n=13 in M, n=12 in MC, n=15 in C) and asterisks indicate statistical significance (*p<0.05, ** p<0.01, ***p<0.001, **** p<0.0001). All DIC scale bars =100µm, confocal scale bar = 50µm

3.3.3 SH-SY5Y tumours express mesenchymal markers prior to organoid isolation

Prior to organoid isolation, a portion of SH-SY5Y xenograft was embedded in paraffin for future analysis. We stained sections of this sample for the mesenchymal markers vimentin and N-Cadherin. Using immunofluorescence staining we confirmed the expression of both vimentin and N-cadherin in the SH-SY5Y tissue prior to organoid isolation (Fig. 3.3.3). We noticed heterogenous vimentin expression across the tissue (white*= low expression, gold* = high expression). This may explain why some organoids from the same tumour are invasive while others are not.

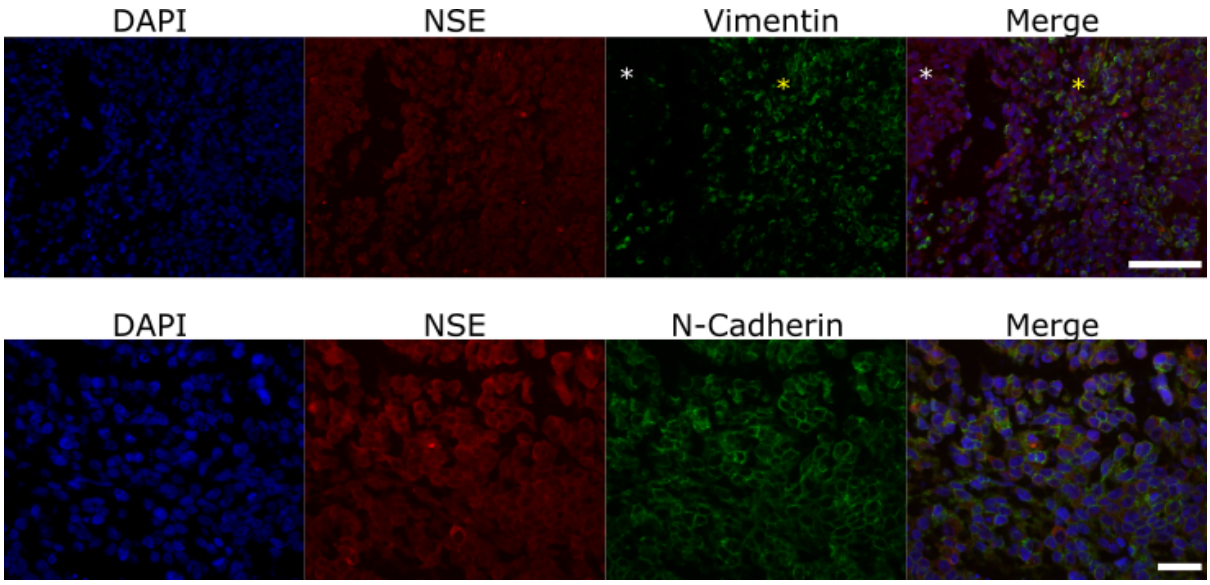

Figure 3.3.3. SH-SY5Y xenografts express mesenchymal markers prior to organoid isolation. Sections of the same SH-SY5Y tumours from which organoids were derived fluorescently stained for mesenchymal marker expression; vimentin (top) and N-Cadherin (bottom). Neuron specific enolase (NSE) is a marker for neuroblastoma cells and nuclei are counterstained with DAPI. Scale bars = 100µm (vimentin, top) and 30µm (N-cadherin, bottom). White stars indicate region of low vimentin expression and yellow stars indicate regions of high expression.

3.3.4 Key Findings

1. We found that the *in vivo* tumour microenvironment promoted a distinct cellular invasion strategy in SH-SY5Y cells.

2. The protrusive phenotype was identified in all three matrices, however it was more prevalent and more aggressive in M.

3. The phenotypic behaviour of SH-SY5Y organoids was ECM-dependent.

4. The expression of mesenchymal markers can be detected in SH-SY5Y tumour tissue prior to organoid isolation.

3. Results

Chapter 3.4 Repression of the *MYCN* gene in a NB cell line promotes less aggressive cellular behaviour in 3D *in vitro*.

3.4.1 Introduction

Amplification of the *MYCN* gene occurs in approximately 20% of NBs and correlates with more aggressive disease and worse outcome (24). Thus, elevated levels of MYCN expression is thought to activate genes that drive aggressive tumour behaviour. However, we found that organoids isolated from two of the earlier mentioned *MYCN* amplified PDXs did not display invasive behaviour in organoid assays. Therefore, we aimed to investigate whether elevated MYCN expression levels could promote the growth and invasion of a NB cell line in 3D ECM environments. For this experiment we used the SHEP-Tet21N cell line which can be treated with the antibiotic, doxycycline, to repress the expression of *MYCN* (127). We embedded single untreated SHEP-Tet21N cells (*MYCN*-ON) and cells that were continuously cultured in 50ng/mL doxycycline (*MYCN*-OFF) in M, MC and C hydrogels. We then used DIC time-lapse microscopy to observe clonal expansion and cellular invasion of the cell line clusters over the course of 5 days.

3.4.2 MYCN levels are associated with aggressive NB behaviour

We observed highly invasive behaviour in SHEP-Tet21N cell line clusters when *MYCN* transcription was turned “ON” and “OFF” (Fig 3.4.2 A). All cell clusters were classified as invasive and exclusively employed the collective mesenchymal strategy in each of the 3 matrices. However, the invasive behaviour we observed appeared more aggressive in *MYCN*-ON cells (Fig 3.4.2 A). Furthermore, cells with *MYCN*-ON grew significantly larger than those with *MYCN*-OFF in all three matrices (Fig 3.4.2 B). Measuring the circularity of individual cell clusters confirmed our microscopic observations and illustrates the highly invasive nature of the SHEP-Tet21N cell line regardless of *MYCN* status; this is evident on the plots where the vast majority of clusters have lost their spherical morphology by t48hr (circularity < 0.4) in M (Fig 3.4.2 C), MC (Fig 3.4.2 D), and C (Fig 3.4.2 E). The trend of

circularity loss is similar in *MYCN*-ON and *MYCN*-OFF cell lines, but the representative time-lapse and confocal images show that in fact invasion is more aggressive when *MYCN* transcription is turned “ON” (Fig 3.4.2 F).These results show that cells with high levels of MYCN display more aggressive behaviour in our model of local invasion than their *MYCN*-repressed counterparts.

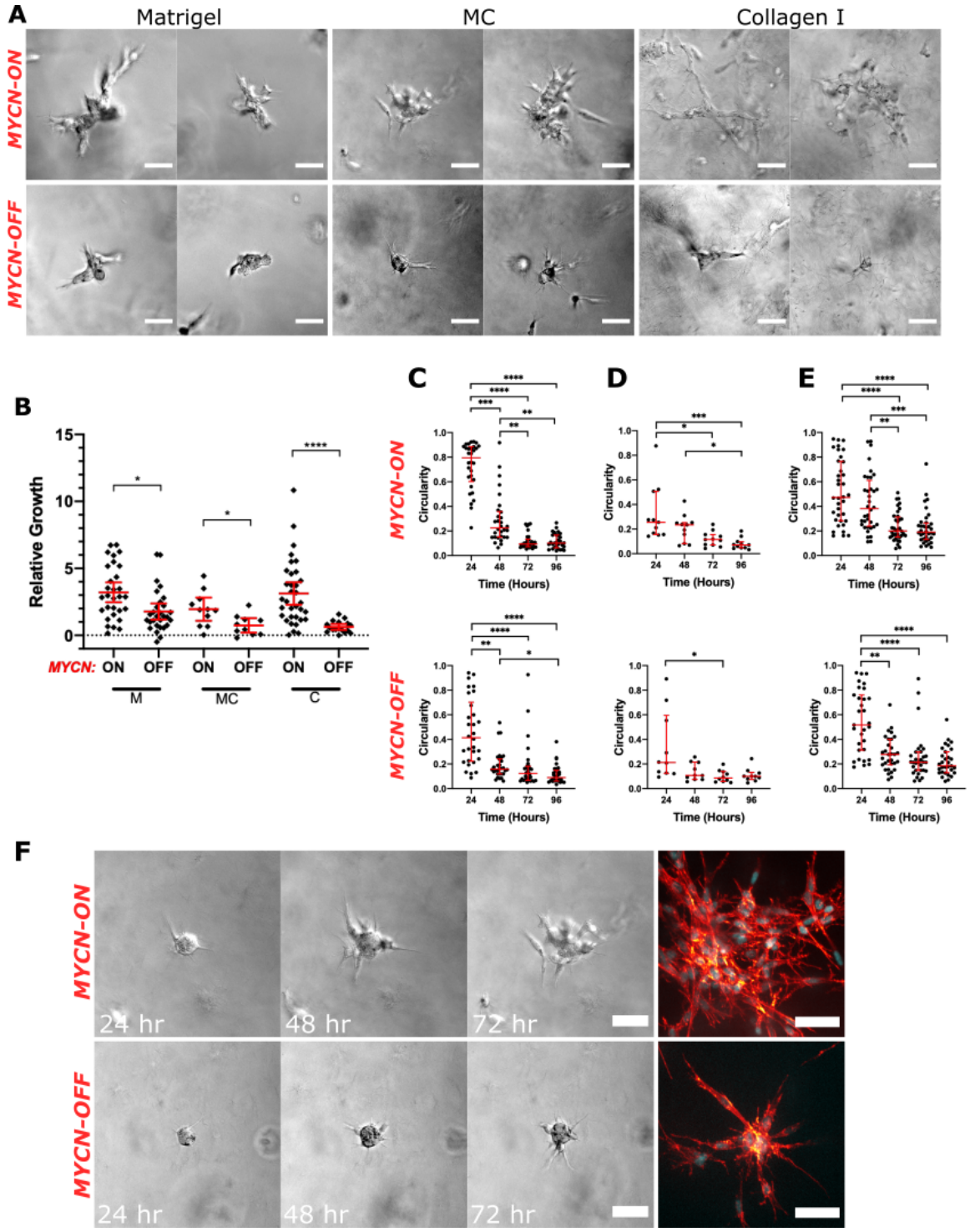

Figure 3.4.2 Repressing *MYCN* expression promotes less aggressive cellular behaviour in the SHEP-Tet21N cell line. A) Representative DIC images of untreated SHEP-Tet21N (*MYCN*-ON) and doxycycline treated (*MYCN*-OFF) cells after 72 hours in 3D M, MC or C hydrogels. Relative growth of organoids was calculated by dividing the difference in cluster area at t72hr compared to t24hr, by the area at t24hr, and presented on the plot (B) (Brown-Forsythe ANOVA with T3 Dunnett post-hoc tests, horizontal bars represent mean ± 95% confidence intervals). Circularity of *MYCN*-ON and *MYCN*-OFF cell clusters was measured at t72hr in M (C), MC (D), and C (E) (Kruskal-Wallis and Dunn's post-hoc tests, horizontal bars represent median and interquartile range). F) Representative DIC time-lapse and confocal images (t120hr) comparing SHEP-Tet21N cell clusters with *MYCN*-ON and *MYCN*-OFF; nuclei are stained with DAPI (cyan) and F-actin is stained with phalloidin (red hot). For all plots, each dot represents one cell cluster (*MYCN*-ON; n=30 in M, n=11 in MC, n=34 in C. *MYCN*-OFF; n=29 in M, n=10 in MC, n=17 in C) and asterisks indicate statistical significance (* p<0.05, **p<0.01, ***p<0.001, **** p<0.0001). All scale bars =50µm.

3.4.3 Key Findings

1. The SHEP-Tet21N cell line can be used to study the effect of MYCN on local NB invasion

2. SHEP-Tet21N cells are invasive in all three matrices, regardless of *MYCN* status

3. The repression of *MYCN* in the SHEP-Tet21N cell line promotes less aggressive cellular behaviour

4.General Discussion

4.1 NB organoids isolated from PDXs are phenotypically heterogenous during local invasion

We found that NB cells were capable of employing a number of distinct migration strategies to invade ECM hydrogels. We believe that we have identified four distinct invasive phenotypes, that we have classified based on morphology. We found that NB organoids commonly invaded as collective strands where adhesion between neighbouring cells was maintained. The cells at the leading edge of these strands appear mesenchymal-like due to the presence of one or several actin-rich protrusions which is indicative of cancer cells with mesenchymal traits. Thus, we have termed this cellular strategy of invasion "collective mesenchymal". Previous studies have described similar modes of multicellular migration where leading cells are believed to proteolytically degrade the matrix, creating a track that is widened by following cells (128). Collective strands such as this have been described in breast cancer in 3D *in vitro* and *in vivo* (102, 129). Interestingly, similar collective invasion has also been seen in melanoma cells *in vivo* using intravital imaging technology (130). Furthermore, clusters of circulating tumour cells are found in blood samples taken from patients with metastatic melanoma (131), providing evidence of collective invasion in patients. In a small study of 28 NB patients, one circulating tumour cell cluster was identified and interestingly it was found in a high-risk patient with distant lymph node metastasis (132). We also observed collective strand invasion in our "elongated" organoids, however we anticipate that this phenotype is molecularly distinct due to the fact that multicellular branching is uncommon and that the cells within these organoids appear to migrate in a common direction with a leading multicellular stream/strand. In comparison, collective mesenchymal organoids extend multicellular strands in multiple directions and these strands commonly branch.

NB is derived from neural progenitor cells and thus displays neuronal behaviour, notably neurite formation, which is commonly seen in NB cell lines (133, 134). We identified invasive NB organoids with dispersed cells extending neurite-like processes into ECM hydrogels and thus termed this phenotype "neuronal". This cellular strategy of invasion is morphologically

comparable to that seen in glioma, where cells invade as a collective network with transient cell-cell interactions both *in vivo* and in 3D *in vitro* (135, 136). Finally, we identified organoids that maintained a round central cell mass while extending long thin protrusions into the local ECM. We have termed this phenotype "protrusive" and believe that it may be unique to NB organoids. The radial protrusions observed are actin-rich and often do not contain nuclei. When nuclei are seen within these protrusions they were individually migrating or loosely followed by multicellular streams. We suspect that this phenotype is also neuronal in nature due to the long leading protrusion that is neurite-like and interestingly organotypic brain cultures of glioblastoma also display a radial pattern of invasion (137), however it appears less directional than that described here. Furthermore, single cell dissemination is frequently observed in glioblastoma and we did not observe NB organoids disseminating cells into the surrounding matrices in our time-lapse images.

In addition to the invasive phenotypes discussed above, phenotypic heterogeneity was also seen in non-invasive organoids. Organoids that maintained a round cellular mass were termed "spheroid", while round organoids that developed a lumen were termed "cyst". Cysts were more commonly found in M and MC matrices compared to collagen, suggesting again that Matrigel promotes phenotypic heterogeneity in NB organoids. Cyst formation in Matrigel was also seen by Nguyen-Ngoc et al. who describe a bi-layered epithelial structure that models the formation of epithelial ducts (109). Although we have not performed experiments to investigate whether the cyst-like structures seen here were bi-layered, we speculate, given the origin of NB, that they may in fact be neuroepithelial in nature. Neuroepithelial cyst formation in 3D hydrogels has been described as a model of neural tube development *in vivo* (138).

Considering the multipotency of the cells of origin for NB, the heterogeneity observed in organoids isolated from PDXs is unsurprising. Ultimately, we hypothesise that within a given PDX the intratumour heterogeneity of NB *in situ* is retained and that some cellular populations within a given PDX are more neuroepithelial in nature whilst others are more neuronal or mesenchymal.

4.2 The phenotypic heterogeneity seen in PDX organoids cannot be recapitulated using cell lines

NB cell lines cultured in the same platform under the same conditions as NB organoids did not display cellular heterogeneity such as that seen in PDX organoids. Thus, we believe that cell lines rely on an intrinsic migratory programme, meaning they lack the ability to overcome environmental challenges by adapting distinct migration strategies. Interestingly, EMT can occur as an "intrinsic cell autonomous process" or as a transient process in response to environmental stimuli (139). Intrinsic EMT and stem-cell like phenotypes have been described and are believed to be irreversible due to genetic alterations and a low capacity for differentiation (140). Thus, we speculate that the cell lines tested here, given their clonal nature, may have intrinsic phenotypes that determine their migratory behaviour. That being said, when we grew SH-SY5Y cells *in vivo*, the resulting tumours yielded organoids that responded to ECM composition. Furthermore the *in vivo* TME induced a distinct organoid phenotype. The cell lines we used in our studies were taken directly from a 2D monolayer culture where they are homogenously exposed to environmental factors such as oxygen, nutrients and waste. In contrast, when we introduce cell lines to an *in vivo* environment they grow as a tumour mass, where cells are heterogeneously exposed to such factors. One study employs a hypoxia-sensing xenograft model that allows hypoxic cells to be isolated from their non-hypoxic counterparts upon xenograft extraction (141). This study describes a distinct phenotype in hypoxic compared to non-hypoxic breast cancer cells and interestingly these phenotypic changes could not be induced by depriving cells of oxygen *in vitro*. The *in vivo* culture of cancer cell lines (xenograft) has also been shown to induce phenotypical changes in tumour initiating cells in ovarian cancer (142). Thus, we hypothesise that the *in vivo* tumour microenvironment can promote a level of cellular heterogeneity in NB cell lines. This is supported by our finding that the expression of EMT markers was heterogenous in SH-SY5Y xenografts. That being said, the phenotypic heterogeneity seen in these organoids was not as profound as that seen in organoids isolated from PDXs.

4.3 Matrigel is the preferred substratum for NB invasion

Here we have optimised the organoid assay model described in breast cancer by Ewald et al. for the study of local NB invasion (109). We have successfully isolated and grown organoids from NB PDXs in 3D hydrogels and observed cellular dynamics of invasion in real-time. In their studies of breast cancer, Ewald et al. show that ECM hydrogels composed of rat tail collagen I promote invasion and dissemination of malignant mammary epithelium whilst hydrogels composed of Matrigel do not (143). This preference has also been documented in pancreatic cancer (144) as well as colon cancer, where collagen I promotes the expression of EMT-TFs and mesenchymal genes (145). Conversely, our study demonstrates that NB organoids preferentially invade hydrogels that contain Matrigel. Although unexpected this result is not entirely surprising given the vast differences between these cancers and NB.

Matrigel is a BM-like matrix that is extracted from the Engelbreth-Holm-Swarm (EHS) mouse sarcoma; a tumour that is rich in ECM proteins. Matrigel is composed primarily of laminin (~60%), collagen IV (~30%), nidogen (~5%), heparan sulphate proteoglycan (perlecan, ~3%) and entactin (~1%). The matrix also contains a range of growth factors including TGF-β, insulin-like growth factor (IGF-1), epidermal growth factor (EGF) and fibroblast growth factor (bFGF) (146). However, due to the wide range of effects that GFs have on cells, we used GFR Matrigel to limit their impact on invasion.

Based on studies of NCC migration, both *in vivo* and *in vitro*, ECM components are classified into three distinct categories; permissive, non-permissive and inhibitory. ECM components that are permissive are expressed along the migratory pathways of NCCs and promote their motility. They include laminin, fibronectin, collagen type I and collagen type IV, which are all well evolutionarily conserved. However, of these only fibronectin, certain laminin isoforms and collagen type IV are believed to be critical for NC development (147). For instance, Olsson et al. have shown that implantation of micromembranes coated with laminin-1 or fibronectin into the pre-migratory NC of axolotl embryos induces extensive NCC migration (148). It has also previously been shown that NCCs migrate extensively in BM-like gels and that their migration is far more restricted in gels composed of collagen type I from rat tail, which is in agreement with our observations (149). Bilozur et al. also showed that the

addition of fibronectin to collagen type I gels stimulates migration, but that its addition to BM gels has no effect indicating that migration is already optimal in this matrix. Furthermore, this study demonstrates that a competitive agonist for laminin (YIGSR) inhibits NCC migration in BM gels, suggesting that laminin is essential for crest cell motility. In the chick, laminin containing basal laminae are also the preferred substratum for migration of NCCs (150). Therefore, we suspect that the embryonal origin of NB may be responsible for its preferential invasion of hydrogels composed of laminin rich Matrigel. Laminin is also well documented as a promoter of neurite formation (151) and interestingly we observed organoids with neurite-like processes in hydrogels containing Matrigel more often than in those composed of collagen type I. Of the cell lines tested, only invasive Lan-1 clusters were characterised as neuronal and interestingly Lan-1 was also the only cell line to preferentially invade hydrogels containing Matrigel over collagen type I.

4.4 Local invasion of NB *in vitro* is dependent on the sample of origin

We showed that organoids isolated from 603x and Felix displayed aggressive invasive behaviour in 3D ECM cultures and both showed a preference for matrices containing M. In contrast, we found that organoids isolated from 573x and 424x were for the most part non-invasive in all three of the matrices tested. Therefore we hypothesise that the origin of the PDX may be an important determinant of invasive behaviour in 3D *in vitro*.

603x was derived from a primary tumour of a stage 4 NB patient at diagnosis. 603x is *MYCN* amplified and was the only PDX we tested with high telomerase reverse transcriptase (hTERT) mRNA levels. Rearrangement of the *hTERT* gene is the second most common genetic defect in NB after *MYCN* amplification and correlates with more aggressive disease and poor prognosis (152). Although well known for its function in telomere lengthening and the resulting anti-apoptotic effects, hTERT overactivation has also been implicated in invasion and metastasis of many cancers. One study investigated the effect of *hTERT* knockdown on NB cell invasion using Matrigel coated transwell assays (153). Chakrabarti et al. found that the knockdown resulted in decreased expression of MMPs (MMP-2 and MMP-9) and an inhibition of cell invasion of approximately 90%. A similar study in glioblastoma also showed decreased MMP-9 expression and reduced invasion of multicellular spheroids

in response to *hTERT* knockdown (154). In gastric cancer, hTERT has been shown to promote EMT *in vitro* through the Wnt/β-catenin and TGF-β pathways. Furthermore, cells overexpressing hTERT were shown to form more metastatic colonies *in vivo* (155). The same study also found a correlation between Snail1, vimentin and hTERT mRNA levels in tumours derived from gastric cancer patients. In another study hTERT was shown to promote gastric cancer invasion *in vivo* by increasing integrin-β1 expression by enhancing FOXO3a ubiquitination (156). Integrin-β1 is expressed on neuroblastoma tumours and is required for neurite outgrowth in neuroblastoma cells, where its binding to collagen type IV (major component of M) but not collagen type I is modulated, which is interesting given our organoids protrude more aggressively into Matrigel (157, 158). In colorectal cancer, h*TERT* drives metastasis through the EMT activator *ZEB*1 (159), which has been implicated in melanoma invasion and the migration and invasion of NB cells (160, 161). *TERT* promoter mutations are commonly observed in melanomas and result in overexpression of the gene. Interestingly, these mutations are observed more frequently in metastatic tissue compared to primary tumour tissue (162). Therefore, high levels of TERT mRNA seem to regulate tumour cell invasion through many mechanisms that have been implicated in NB metastasis. Interestingly, it has been shown that telomerase activity is decreased in response to knockdown of the 37kDa/67kDa Laminin Receptor (LRP/LR) in human embryonic kidney cells (HEK293) and breast cancer cells (163). This study demonstrates an interaction between LRP/LR and hTERT that could also potentially explain the preferential invasion of 603x organoids into hydrogels containing Matrigel. While 424x and 573x are also both *MYCN* amplified, organoids isolated from these PDXs are predominantly non-invasive in our model. However, both PDXs only have intermediate levels of TERT mRNA compared to the high levels observed in 603x. Therefore, we speculate that high levels of hTERT activation in concert with MYCN amplification may explain the invasiveness we observe in organoids isolated from 603x.

Surprisingly, we found that the non-MYCN amplified PDX, Felix, yielded organoids that displayed the most aggressive invasion in our 3D experiments. Furthermore, clonal clusters derived from the non-MYCN amplified cell line, SH-SY5Y, and organoids derived from SH-SY5Y tumours also showed aggressive invasive behaviour. Considering the low levels of MYCN in these cases, we speculate that there must be another driver of the observed

aggressive cellular behaviour. Interestingly, both Felix-PDX (*ALK*^{F1245}) and SH-SY5Y (*ALK*^{F1174}) harbour activating mutations in the *ALK* gene. *ALK* is the most frequently, somatically mutated gene in NB and is found in approximately 8 - 9% of cases (14% of high-risk cases) (164, 165), with mutations at three amino acid positions accounting for 85% of these; R1275 (43%), F1174 (30%) and F1245 (12%). Such mutations, as well as aberrations in the *ALK* gene, correlate with poor prognosis and worse overall survival (29). In fact, *ALK* mutations are more common in samples from patients with progressive or relapsed disease (166) and ALK mRNA expression levels are significantly higher in patients with clinically aggressive NB, including high-risk metastatic disease with or without *MYCN* amplification (167). Moreover, inhibition of ALK in neural crest explants blocks delamination, resulting in a loss of NCC migration (30). Therefore, we suspect that ALK expression levels may contribute to the invasive behaviour we observed in Felix and SH-SY5Y cells. In support of this, overexpression of *ALK* in NB cells has been shown to promote migration and invasion in transwell assays, while siRNA mediated knockdown was shown to have the opposite effect (33). The highly invasive behaviour that we observed in Lan-1 and SHEP-Tet21N (*MYCN*-ON) cell line clusters was less surprising given their elevated levels of *MYCN* expression. That being said, both harbour mutations in the ALK gene. Interestingly, when mice are generated to overexpress both *ALK* and *MYCN* in the neural crest, they develop more aggressive NBs with earlier onset, higher penetrance and greater lethality than mice overexpressing *MYCN* alone (168). Another study showed that *ALK*-expressing neuronal cells display increased migratory and invasive behaviour when transduced with *MYCN* and that the migration/invasion occurred in a dose-dependent manner with FGF2 (169), which also re-enforces our results showing that FGF2 is required for Felix organoid invasion. Overexpression of both *MYCN* and the *ALK* mutant *in vivo* also increased tumour invasion and metastasis. Ueda et al. go on to show that the *ALK* mutation synergises with *MYCN* amplification to promote a more malignant phenotype through downregulation of ECM/BM genes, notably collagen type IV, and upregulation of MMP-2, which catalyses the degradation of collagen type IV. Therefore, the literature supports our speculation that elevated levels of ALK may be responsible for the observed invasive behaviour in certain cell lines and organoids, including perhaps the preferential invasion of Matrigel.

The aggressive invasion observed in Felix organoids was also interesting due to the way this PDX was established. Unlike the other PDXs tested, Felix-PDX was derived from a blood sample of a stage 4 NB patient, post-mortem (170). Therefore, the malignant cells used to establish this PDX had already acquired an invasive phenotype, disseminated from the primary tumour or metastatic site and entered the patient's circulation. CTCs have been isolated from patient blood samples using Matrigel transwell assays in lung and oesophageal cancers, providing evidence of their invasive nature (171). Establishing a PDX from CTCs also involves combining all of the malignant cells isolated from the large blood sample, which could perhaps yield a more heterogenous PDX that would explain the invasive heterogeneity seen in Felix organoids. Furthermore, we found that Felix organoids were significantly larger than organoids isolated from the remaining PDXs, despite identical methods of isolation. We suspect that this may be due to differences in ECM composition, whereby the ECM in Felix-PDXs was denser and more difficult to digest. Interestingly, the density and organisation of reticular fibres has been shown to strongly define a subset of NB patients within the high-risk cohort that have ultra-poor prognosis (172). This may also explain the preferential invasion of hydrogels containing Matrigel, which have a higher protein density (8-11 mg/mL) than our hydrogels composed of 3mg/ml collagen type I.

While this study alone cannot definitively state why some PDXs yield more invasive organoids than others, we show that this 3D model of local invasion can be used as a valuable tool to study NB biology. Although only four PDXs were examined in this pilot study, there is a large number of established NB PDXs. Therefore, we believe that pairing NB organoids and 3D invasion assays may uncover genes and pathways that are involved in the local invasion of this paediatric cancer.

4.5 Repression of *MYCN* transcription promotes less aggressive cellular behaviour in 3D *in vitro.*

The amplification of *MYCN* is well-known as an unfavourable prognostic factor in NB and is correlated with more aggressive disease and worse outcome (173). Thus, as expected, we found that cell clusters expressing *MYCN* grew larger and displayed more aggressive invasive behaviour in 3D invasion assays. The literature supports our suggestion that *MYCN*

expression plays a role in the local invasion of NB. One study employing migration and invasion assays using the transwell set-up showed that that higher levels of *MYCN* expression correlated with increased cell motility and invasiveness (174). In high-risk NB, upregulation of the EMT promoting transcription factor *TWIST1,* is correlated with *MYCN* amplification and was confirmed as a *MYC* transcriptional target (175). MYCN has also been shown to directly repress transcription of the death receptor antagonist, Lifeguard (FAIM2), which is downregulated in high-risk disease. Repression of Lifeguard was shown decrease cell adhesion and increase cell motility, promoting a more invasive phenotype (176). Thus, the literature supports our finding that *MYCN* transcription promotes aggressive cellular behaviour.

4.6 Benefits of 3D culture assays over current models of local invasion in NB

The model we describe has many benefits over current models of local invasion, both in NB and other cancers. Studies using organoid assays and hydrogels can be executed at a relatively low cost, particularly when compared to murine models of metastasis. Our model also offers superior optical accessibility and higher resolution imaging than *in vivo* models of local invasion. Once isolated and embedded into hydrogels, local NB invasion can be observed within a couple of days, which is another advantage of this model compared to *in vivo* studies. That being said, the initial development of PDXs can take a long period of time, however once tumours have grown, using organoids isolated from them can greatly increase their experimental yield. Furthermore, there is a large number of established PDXs currently available.

The literature regarding invasiveness of NB cell lines relies heavily on 2D and 2D to 3D assays, namely the scratch assay and transwell assays. We performed 3D invasion assays with NB cell lines, primarily to compare their behaviour to that observed in NB organoids but also to compare their behaviour with that published in the literature. In one study, invasion was assessed in a panel of NB cell lines using a transwell experimental set up (177). Importantly, the cells were serum starved for 24 hours and the transwell mesh was coated with basement membrane extract. Their panel of cell lines included three of the cell lines we assessed here, namely Kelly (NB 19), SHEP and Lan-1. In our 3D experimental set-up, we

observed highly aggressive behaviour in both the Lan-1 and SHEP cell lines while Kelly cell clusters were deemed to be non-invasive. Conversely, Shankar et al. describe Kelly cells as highly invasive and Lan-1 and SHEP cells as less invasive. They calculate an invasion index of 7 for Kelly cells compared to invasion indices of <1 for both Lan-1 and SHEP. We suspect that the stark contrast in cellular behaviour observed between the two models may be due to the difference in dimensionality and the fact that our model enables cells to migrate collectively. Differences in cellular behaviour between 2D and 3D cultures are well documented (178, 179). For instance NB cells grown in 3D scaffolds display more than 100-fold increased resistance to cisplatin compared to cells grown as a 2D monolayer (180). Interestingly, this chemotherapeutic resistance is comparable to that seen in orthotopic xenograft models, pointing toward the physiological relevance achieved when culturing in true 3D. Recently, the phenotype and motility of glioma cells has been compared across models of different dimensions (181). In 2D, glioma cells display sheet-like morphology and non-directional migration, characterised by random lamellipodium formation. However, glioma cells invading 3D collagen gels were phenotypically similar to neural-progenitor cells, which have a round cell body with a long leading process. This motility pattern is also seen when cells are grafted into organotypic brain slice cultures, suggesting that invasion in 3D culture more closely resembles the *in vivo* scenario. Furthermore, cellular heterogeneity among invasive cells was also seen in both collagen gel and brain slice culture but was absent in the 2D cell population.

Our results show that NB cells are capable of employing a range of distinct migration strategies to invade. Notably, NB cells often migrate collectively as strands (collective mesenchymal) or as streams (protrusive, neuronal). However, transwell assays only assess the migration/invasion of individual NB cells. While there is a lack of literature relating to the modes of migration/invasion in NB *in vivo*, we can look toward the migration of melanoma cells and NCCs. In the embryo, NCCs migrate as dense cohorts of cells that depend on three factors for directed migration; contact inhibition of locomotion, co-attraction and confinement (182). Stream migration in NCCs has also been shown to rely on leader cells at the invasive front with specific molecular signatures (183) and the presence of leader cells as well as the maintenance of cell-cell contacts are documented as requirements for trunk NCC migration (184). Furthermore, in a process known as contact-

stimulated migration, both NCCs and melanoma cells migrate far more effectively as a cohesive group (185). Therefore, due to its origin, we suspect that collective cell migration is the preferred mode of motility in NB. Thus, when modelling/assessing invasion in NB, collective migration must be enabled and thus our model is more suitable than the widely used transwell assay to assess invasion in NB. Furthermore, we believe that our model is more indicative of the *in situ* scenario than currently used 3D *in vitro* MCTS models of NB invasion (186). In these models, cells do not display directional, multicellular, invasive structures as seen here. In fact, cell proliferation contributes largely to the cell spreading that is seen in MCTS. Therefore, we believe that the phenotypic heterogeneity we observed during local invasion of organoids offers an advantage over current *in vitro* models of NB invasion.

4.7 Limitations and Future Work

While we have shown that this model can be useful for studying local invasion in NB, like any model this one has limitations. Firstly, given its origin Matrigel can vary from lot to lot. Also, the exact constituents present in Matrigel are not defined and could differ across gels from the same lot, meaning it's difficult to determine the signals that are contributing to the observed cellular behaviours (187). Furthermore, we cannot say for sure that Matrigel is entirely representative of the human NB microenvironment. This is in part due to the fact that there is a lack of literature regarding extracellular matrix composition in both NBs and healthy human embryos.

Our model does not completely emulate the *in vivo* TME, in part due to the lack of incorporated stromal cells. Importantly, immune cells and cancer associated fibroblasts (CAFs) are well documented to play roles in the invasion of tumour cells. Tumour cell invasion can be facilitated by CAFs through ECM remodelling or stimulated by CAF-secreted pro-invasive stimuli (188). Models incorporating co-culture techniques have been used to assess the role played by CAFs in some cancers. For instance, co-culture of lung adenocarcinoma cells with CAFs results in increased invasion into a collagen matrix compared to cancer cells cultured alone (189). This is also documented in melanoma, where the co-culture of patient-derived melanoma cells with CAFs promotes their invasion through

a Matrigel-coated filter (190). Finally, in a 3D tumour-tissue invasion model comparable to that discussed here, the invasion of patient-derived pancreatic ductal adenocarcinoma (PDAC) cells is increased when CAFs are added to the culture (191). Immune cells possess the ability to promote an EMT and invasion in tumour cells through secreted factors including cytokines, growth factors and MMPs (192). Co-culture of tumour associated macrophages (TAMs) with colorectal cancer cells induces an EMT and increases their migration in scratch and transwell assays (193). In a 3D co-culture model employing live-imaging of 3D Matrigel invasion, bone-marrow macrophages are required for the invasion of mammoshperes representing breast cancer (194). Therefore, in future studies we aim to further optimise this 3D platform to facilitate co-culture. Although this will add a level of complexity to the assays, it will move our model another step closer to the *in-situ* scenario of local NB invasion and allow us to explore the roles played by stromal cells, such as CAFs and TAMs, in local NB invasion.

We have characterised six distinct phenotypes in organoids derived from human NBs based on morphology, however we have not confirmed that these phenotypes are molecularly distinct. Our next experiments will investigate whether the identified phenotypes have different gene expression profiles by isolating organoids and doing RNA sequencing and bioinformatic pathway analysis. We aim to identify specific invasive gene signatures in NB, which we can then target using this model to confirm/identify key players in the local invasion in NB.

We found that mesenchymal markers were heterogeneously expressed in SH-SY5Y tumours, however we have not yet evaluated their expression in organoids *in vitro* or in PDX tumours. We hypothesise that the expression of mesenchymal genes may predict invasiveness in organoids and hence we aim to perform marker analysis in PDXs and complimentary organoids.

We believe that the model described in this study has many applications for the study of NB biology. It offers an excellent platform to study the effects of gene knockdown/induction on local invasion. For instance, to examine the effect of hTERT or ALK on the invasion of NB organoids. Based on our current results, it would be interesting to knockdown hTERT in 603x

organoids to see if this decreases invasion or to induce hTERT expression in organoids isolated from 424x to see if this promotes invasion. By the same logic, ALK knockdown in Felix organoids or overexpression in 424x organoids could provide insights into the invasion process.

Conclusion

This study demonstrates that 3D culture assays are a valuable tool to study local invasion in NB. We found that various matrix compositions induced distinct cellular behaviours, where Matrigel was the preferred substratum for local organoid invasion. We also showed that the invasiveness of organoids was PDX- and cell line-dependent. We have identified and characterised six distinct phenotypes in NB organoids isolated from PDXs. In contrast, we found that NB cell lines were phenotypically confined during invasion of the local ECM and while organoids isolated from cell line xenografts displayed a broader range of phenotypes compared to clonal cell line clusters, they could not recapitulate the diversity seen in PDX organoids. We found that organoid medium supplemented with both FBS and bFGF induced the most aggressive cellular behaviour and the widest range of phenotypes. We also used 3D invasion assays to show that repression of the powerful prognostic marker in NB, *MYCN,* results in less aggressive cellular behaviour in a NB cell line. Overall, we propose the pairing of PDX organoid culture and 3D invasion assays as a valuable tool to observe NB invasion in high-resolution and real-time and discover the molecular mechanisms controlling local invasion in this paediatric cancer of unmet clinical need.

References

1. Steliarova-Foucher E, Colombet M, Ries LAG, Moreno F, Dolya A, Bray F, et al. International incidence of childhood cancer, 2001-10: a population-based registry study. Lancet Oncol. 2017;18(6):719-31.
2. Global, regional, and national age-sex-specific mortality for 282 causes of death in 195 countries and territories, 1980-2017: a systematic analysis for the Global Burden of Disease Study 2017. Lancet. 2018;392(10159):1736-88.
3. Colon NC, Chung DH. Neuroblastoma. Adv Pediatr. 2011;58(1):297-311.
4. Maris JM, Hogarty MD, Bagatell R, Cohn SL. Neuroblastoma. Lancet. 2007;369(9579):2106-20.
5. Whittle SB, Smith V, Doherty E, Zhao S, McCarty S, Zage PE. Overview and recent advances in the treatment of neuroblastoma. Expert Rev Anticancer Ther. 2017;17(4):369-86.
6. Smith V, Foster J. High-Risk Neuroblastoma Treatment Review. Children (Basel). 2018;5(9).
7. Basta NO, Halliday GC, Makin G, Birch J, Feltbower R, Bown N, et al. Factors associated with recurrence and survival length following relapse in patients with neuroblastoma. British journal of cancer. 2016;115(9):1048-57.
8. Armstrong AE, Danner-Koptik K, Golden S, Schneiderman J, Kletzel M, Reichek J, et al. Late Effects in Pediatric High-risk Neuroblastoma Survivors After Intensive Induction Chemotherapy Followed by Myeloablative Consolidation Chemotherapy and Triple Autologous Stem Cell Transplants. J Pediatr Hematol Oncol. 2018;40(1):31-5.
9. Gatta G, Ferrari A, Stiller CA, Pastore G, Bisogno G, Trama A, et al. Embryonal cancers in Europe. European Journal of Cancer. 2012;48(10):1425-33.
10. DuBois SG, Kalika Y, Lukens JN, Brodeur GM, Seeger RC, Atkinson JB, et al. Metastatic sites in stage IV and IVS neuroblastoma correlate with age, tumor biology, and survival. J Pediatr Hematol Oncol. 1999;21(3):181-9.
11. Cohn SL, Pearson AD, London WB, Monclair T, Ambros PF, Brodeur GM, et al. The International Neuroblastoma Risk Group (INRG) classification system: an INRG Task Force report. J Clin Oncol. 2009;27(2):289-97.
12. Monclair T, Brodeur GM, Ambros PF, Brisse HJ, Cecchetto G, Holmes K, et al. The International Neuroblastoma Risk Group (INRG) staging system: an INRG Task Force report. Journal of clinical oncology : official journal of the American Society of Clinical Oncology. 2009;27(2):298-303.
13. Marshall GM, Carter DR, Cheung BB, Liu T, Mateos MK, Meyerowitz JG, et al. The prenatal origins of cancer. Nat Rev Cancer. 2014;14(4):277-89.
14. Vo KT, Matthay KK, Neuhaus J, London WB, Hero B, Ambros PF, et al. Clinical, Biologic, and Prognostic Differences on the Basis of Primary Tumor Site in Neuroblastoma: A Report From the International Neuroblastoma Risk Group Project. Journal of Clinical Oncology. 2014;32(28):3169-76.
15. Sommer L, Shah N, Rao M, Anderson DJ. The cellular function of MASH1 in autonomic neurogenesis. Neuron. 1995;15(6):1245-58.
16. Huber K. The sympathoadrenal cell lineage: Specification, diversification, and new perspectives. Dev Biol. 2006;298(2):335-43.

17. Lumb R, Schwarz Q. Sympathoadrenal neural crest cells: The known, unknown and forgotten? Development, Growth & Differentiation. 2015;57(2):146-57.
18. Saito D, Takase Y, Murai H, Takahashi Y. The Dorsal Aorta Initiates a Molecular Cascade That Instructs Sympatho-Adrenal Specification. Science (New York, NY). 2012;336(6088):1578.
19. Betters E, Liu Y, Kjaeldgaard A, Sundström E, García-Castro MI. Analysis of early human neural crest development. Dev Biol. 2010;344(2):578-92.
20. Tomolonis JA, Agarwal S, Shohet JM. Neuroblastoma pathogenesis: deregulation of embryonic neural crest development. Cell Tissue Res. 2018;372(2):245-62.
21. Li D, Mei H, Qi M, Yang D, Zhao X, Xiang X, et al. FOXD3 is a novel tumor suppressor that affects growth, invasion, metastasis and angiogenesis of neuroblastoma. Oncotarget. 2013;4(11):2021-44.
22. Ikram F, Ackermann S, Kahlert Y, Volland R, Roels F, Engesser A, et al. Transcription factor activating protein 2 beta (TFAP2B) mediates noradrenergic neuronal differentiation in neuroblastoma. Mol Oncol. 2016;10(2):344-59.
23. Fang W-H, Wang Q, Li H-M, Ahmed M, Kumar P, Kumar S. PAX3 in neuroblastoma: oncogenic potential, chemosensitivity and signalling pathways. J Cell Mol Med. 2014;18(1):38-48.
24. Ambros PF, Ambros IM, Brodeur GM, Haber M, Khan J, Nakagawara A, et al. International consensus for neuroblastoma molecular diagnostics: report from the International Neuroblastoma Risk Group (INRG) Biology Committee. Br J Cancer. 2009;100(9):1471-82.
25. Wakamatsu Y, Watanabe Y, Nakamura H, Kondoh H. Regulation of the neural crest cell fate by N-myc: promotion of ventral migration and neuronal differentiation. Development. 1997;124(10):1953.
26. Weiss WA, Aldape K, Mohapatra G, Feuerstein BG, Bishop JM. Targeted expression of MYCN causes neuroblastoma in transgenic mice. EMBO J. 1997;16(11):2985-95.
27. Olsen RR, Otero JH, Garcia-Lopez J, Wallace K, Finkelstein D, Rehg JE, et al. MYCN induces neuroblastoma in primary neural crest cells. Oncogene. 2017;36(35):5075-82.
28. Iwahara T, Fujimoto J, Wen D, Cupples R, Bucay N, Arakawa T, et al. Molecular characterization of ALK, a receptor tyrosine kinase expressed specifically in the nervous system. Oncogene. 1997;14(4):439-49.
29. Bresler SC, Weiser DA, Huwe PJ, Park JH, Krytska K, Ryles H, et al. ALK mutations confer differential oncogenic activation and sensitivity to ALK inhibition therapy in neuroblastoma. Cancer cell. 2014;26(5):682-94.
30. Gonzalez Malagon SG, Lopez Muñoz AM, Doro D, Bolger TG, Poon E, Tucker ER, et al. Glycogen synthase kinase 3 controls migration of the neural crest lineage in mouse and Xenopus. Nat Commun. 2018;9(1):1126-.
31. Liu Z. TCJ. Molecular Genetics of Neuroblastoma. . In: Pacak K., Taïeb D. (eds) Diagnostic and Therapeutic Nuclear Medicine for Neuroendocrine Tumors. Contemporary Endocrinology. Humana Press, Cham2017.
32. Limpt Vv, Schramm A, Lakeman A, Sluis Pv, Chan A, Noesel Mv, et al. The Phox2B homeobox gene is mutated in sporadic neuroblastomas. Oncogene. 2004;23(57):9280-8.
33. Hasan MK, Nafady A, Takatori A, Kishida S, Ohira M, Suenaga Y, et al. ALK is a MYCN target gene and regulates cell migration and invasion in neuroblastoma. Sci Rep. 2013;3:3450.

34. Bachetti T, Di Paolo D, Di Lascio S, Mirisola V, Brignole C, Bellotti M, et al. PHOX2B-mediated regulation of ALK expression: in vitro identification of a functional relationship between two genes involved in neuroblastoma. PloS one. 2010;5(10).
35. Dillekås H, Rogers MS, Straume O. Are 90% of deaths from cancer caused by metastases? Cancer Medicine. 2019;8(12):5574-6.
36. Mehlen P, Puisieux A. Metastasis: a question of life or death. Nature Reviews Cancer. 2006;6(6):449-58.
37. Paget S. THE DISTRIBUTION OF SECONDARY GROWTHS IN CANCER OF THE BREAST. The Lancet. 1889;133(3421):571-3.
38. EWING J. NEOPLASTIC DISEASES. Annals of Surgery. 1919;69(3):342.
39. Fidler IJ, Nicolson GL. Organ selectivity for implantation survival and growth of B16 melanoma variant tumor lines. J Natl Cancer Inst. 1976;57(5):1199-202.
40. Hart IR, Fidler IJ. Role of Organ Selectivity in the Determination of Metastatic Patterns of B16 Melanoma. Cancer Research. 1980;40(7):2281.
41. Gao Y, Bado I, Wang H, Zhang W, Rosen JM, Zhang XHF. Metastasis Organotropism: Redefining the Congenial Soil. Developmental Cell. 2019;49(3):375-91.
42. Celià-Terrassa T, Kang Y. Metastatic niche functions and therapeutic opportunities. Nature Cell Biology. 2018;20(8):868-77.
43. Liu Y, Cao X. Characteristics and Significance of the Pre-metastatic Niche. Cancer Cell. 2016;30(5):668-81.
44. Nieto MA, Huang Ruby Y-J, Jackson Rebecca A, Thiery Jean P. EMT: 2016. Cell. 2016;166(1):21-45.
45. Thiery JP, Acloque H, Huang RY, Nieto MA. Epithelial-mesenchymal transitions in development and disease. Cell. 2009;139(5):871-90.
46. Puisieux A, Brabletz T, Caramel J. Oncogenic roles of EMT-inducing transcription factors. Nature Cell Biology. 2014;16(6):488-94.
47. Lamouille S, Xu J, Derynck R. Molecular mechanisms of epithelial-mesenchymal transition. Nat Rev Mol Cell Biol. 2014;15(3):178-96.
48. Campbell K, Casanova J. A common framework for EMT and collective cell migration. Development. 2016;143(23):4291-300.
49. Huang RY, Wong MK, Tan TZ, Kuay KT, Ng AH, Chung VY, et al. An EMT spectrum defines an anoikis-resistant and spheroidogenic intermediate mesenchymal state that is sensitive to e-cadherin restoration by a src-kinase inhibitor, saracatinib (AZD0530). Cell Death Dis. 2013;4(11):e915.
50. Khoo BL, Lee SC, Kumar P, Tan TZ, Warkiani ME, Ow SGW, et al. Short-term expansion of breast circulating cancer cells predicts response to anti-cancer therapy. Oncotarget. 2015;6(17):15578-93.
51. Yu M, Bardia A, Wittner BS, Stott SL, Smas ME, Ting DT, et al. Circulating breast tumor cells exhibit dynamic changes in epithelial and mesenchymal composition. Science (New York, NY). 2013;339(6119):580-4.
52. Beerling E, Seinstra D, de Wit E, Kester L, van der Velden D, Maynard C, et al. Plasticity between Epithelial and Mesenchymal States Unlinks EMT from Metastasis-Enhancing Stem Cell Capacity. Cell Reports. 2016;14(10):2281-8.
53. Pandya P, Orgaz JL, Sanz-Moreno V. Modes of invasion during tumour dissemination. Mol Oncol. 2017;11(1):5-27.
54. Friedl P, Locker J, Sahai E, Segall JE. Classifying collective cancer cell invasion. Nat Cell Biol. 2012;14(8):777-83.

55. Friedl P, Alexander S. Cancer invasion and the microenvironment: plasticity and reciprocity. Cell. 2011;147(5):992-1009.
56. Muncie JM, Weaver VM. The Physical and Biochemical Properties of the Extracellular Matrix Regulate Cell Fate. Curr Top Dev Biol. 2018;130:1-37.
57. Yurchenco PD. Basement membranes: cell scaffoldings and signaling platforms. Cold Spring Harb Perspect Biol. 2011;3(2):a004911.
58. Sekiguchi R, Yamada KM. Basement Membranes in Development and Disease. Curr Top Dev Biol. 2018;130:143-91.
59. Frantz C, Stewart KM, Weaver VM. The extracellular matrix at a glance. Journal of cell science. 2010;123(Pt 24):4195-200.
60. Conway JRW, Jacquemet G. Cell matrix adhesion in cell migration. Essays in Biochemistry. 2019;63(5):535-51.
61. Huttenlocher A, Horwitz AR. Integrins in cell migration. Cold Spring Harb Perspect Biol. 2011;3(9):a005074-a.
62. Parekh A, Weaver AM. Regulation of cancer invasiveness by the physical extracellular matrix environment. Cell Adh Migr. 2009;3(3):288-92.
63. Yokoyama K, Kamata N, Fujimoto R, Tsutsumi S, Tomonari M, Taki M, et al. Increased invasion and matrix metalloproteinase-2 expression by Snail-induced mesenchymal transition in squamous cell carcinomas. Int J Oncol. 2003;22(4):891-8.
64. Lin C-Y, Tsai P-H, Kandaswami CC, Lee P-P, Huang C-J, Hwang J-J, et al. Matrix metalloproteinase-9 cooperates with transcription factor Snail to induce epithelial–mesenchymal transition. Cancer Science. 2011;102(4):815-27.
65. Duong TD, Erickson CA. MMP-2 plays an essential role in producing epithelial-mesenchymal transformations in the avian embryo. Developmental Dynamics. 2004;229(1):42-53.
66. Delloye-Bourgeois C, Castellani V. Hijacking of Embryonic Programs by Neural Crest-Derived Neuroblastoma: From Physiological Migration to Metastatic Dissemination. Frontiers in Molecular Neuroscience. 2019;12(52).
67. Gallik KL, Treffy RW, Nacke LM, Ahsan K, Rocha M, Green-Saxena A, et al. Neural crest and cancer: Divergent travelers on similar paths. Mech Dev. 2017;148:89-99.
68. Theveneau E, Mayor R. Neural crest delamination and migration: From epithelium-to-mesenchyme transition to collective cell migration. Dev Biol. 2012;366(1):34-54.
69. Tanno B, Sesti F, Cesi V, Bossi G, Ferrari-Amorotti G, Bussolari R, et al. Expression of Slug Is Regulated by c-Myb and Is Required for Invasion and Bone Marrow Homing of Cancer Cells of Different Origin. Journal of Biological Chemistry. 2010;285(38):29434-45.
70. Vitali R, Mancini C, Cesi V, Tanno B, Mancuso M, Bossi G, et al. Slug (SNAI2) down-regulation by RNA interference facilitates apoptosis and inhibits invasive growth in neuroblastoma preclinical models. Clin Cancer Res. 2008;14(14):4622-30.
71. Monsonego-Ornan E, Kosonovsky J, Bar A, Roth L, Fraggi-Rankis V, Simsa S, et al. Matrix metalloproteinase 9/gelatinase B is required for neural crest cell migration. Dev Biol. 2012;364(2):162-77.
72. Kalev-Altman R, Hanael E, Zelinger E, Blum M, Monsonego-Ornan E, Sela-Donenfeld D. Conserved role of matrix metalloproteases 2 and 9 in promoting the migration of neural crest cells in avian and mammalian embryos. The FASEB Journal. 2020;34(4):5240-61.
73. Sugiura Y, Shimada H, Seeger RC, Laug WE, DeClerck YA. Matrix metalloproteinases-2 and -9 are expressed in human neuroblastoma: contribution of stromal cells to their production and correlation with metastasis. Cancer Res. 1998;58(10):2209-16.

74. Ara T, Fukuzawa M, Kusafuka T, Komoto Y, Oue T, Inoue M, et al. Immunohistochemical expression of MMP-2, MMP-9, and TIMP-2 in neuroblastoma: Association with tumor progression and clinical outcome. Journal of Pediatric Surgery. 1998;33(8):1272-8.
75. Sans-Fons MG, Sole S, Sanfeliu C, Planas AM. Matrix metalloproteinase-9 and cell division in neuroblastoma cells and bone marrow macrophages. Am J Pathol. 2010;177(6):2870-85.
76. Noujaim D, van Golen CM, van Golen KL, Grauman A, Feldman EL. N-Myc and Bcl-2 coexpression induces MMP-2 secretion and activation in human neuroblastoma cells. Oncogene. 2002;21(29):4549-57.
77. Kleinman HK, Jacob K. Invasion Assays. Current Protocols in Cell Biology. 1998;00(1):12.2.1-.2.5.
78. Liang C-C, Park AY, Guan J-L. In vitro scratch assay: a convenient and inexpensive method for analysis of cell migration in vitro. Nature protocols. 2007;2(2):329-33.
79. Li Z, Chen H. miR-34a inhibits proliferation, migration and invasion of paediatric neuroblastoma cells via targeting HNF4alpha. Artif Cells Nanomed Biotechnol. 2019;47(1):3072-8.
80. Li W, Cao J, Liu J, Chu W, Zhang C, Chen S, et al. Downregulation of CDKL1 suppresses neuroblastoma cell proliferation, migration and invasion. Cellular & Molecular Biology Letters. 2019;24(1):19.
81. Zhu S, Zhang X, Weichert-Leahey N, Dong Z, Zhang C, Lopez G, et al. LMO1 Synergizes with MYCN to Promote Neuroblastoma Initiation and Metastasis. Cancer cell. 2017;32(3):310-23.e5.
82. Kelm JM, Timmins NE, Brown CJ, Fussenegger M, Nielsen LK. Method for generation of homogeneous multicellular tumor spheroids applicable to a wide variety of cell types. Biotechnol Bioeng. 2003;83(2):173-80.
83. Mitchell CB, O'Neill GM. Cooperative cell invasion: matrix metalloproteinase-mediated incorporation between cells. Mol Biol Cell. 2016;27(21):3284-92.
84. Sodek KL, Ringuette MJ, Brown TJ. Compact spheroid formation by ovarian cancer cells is associated with contractile behavior and an invasive phenotype. International Journal of Cancer. 2009;124(9):2060-70.
85. Cheng V, Esteves F, Chakrabarty A, Cockle J, Short S, Brüning-Richardson A. High-content analysis of tumour cell invasion in three-dimensional spheroid assays. Oncoscience. 2015;2(6):596-606.
86. Vinci M, Box C, Zimmermann M, Eccles SA. Tumor spheroid-based migration assays for evaluation of therapeutic agents. Methods Mol Biol. 2013;986:253-66.
87. Hirschhaeuser F, Menne H, Dittfeld C, West J, Mueller-Klieser W, Kunz-Schughart LA. Multicellular tumor spheroids: An underestimated tool is catching up again. Journal of Biotechnology. 2010;148(1):3-15.
88. Ben-David U, Siranosian B, Ha G, Tang H, Oren Y, Hinohara K, et al. Genetic and transcriptional evolution alters cancer cell line drug response. Nature. 2018;560(7718):325-30.
89. Campbell K, Rossi F, Adams J, Pitsidianaki I, Barriga FM, Garcia-Gerique L, et al. Collective cell migration and metastases induced by an epithelial-to-mesenchymal transition in Drosophila intestinal tumors. Nat Commun. 2019;10(1):2311.
90. Klymkowsky MW, Rossi CC, Artinger KB. Mechanisms driving neural crest induction and migration in the zebrafish and Xenopus laevis. Cell Adh Migr. 2010;4(4):595-608.

91. Naber HPH, Drabsch Y, Snaar-Jagalska BE, ten Dijke P, van Laar T. Snail and Slug, key regulators of TGF-β-induced EMT, are sufficient for the induction of single-cell invasion. Biochemical and Biophysical Research Communications. 2013;435(1):58-63.
92. Teng Y, Xie X, Walker S, White DT, Mumm JS, Cowell JK. Evaluating human cancer cell metastasis in zebrafish. BMC Cancer. 2013;13:453-.
93. Konantz M, Balci TB, Hartwig UF, Dellaire G, Andre MC, Berman JN, et al. Zebrafish xenografts as a tool for in vivo studies on human cancer. Ann N Y Acad Sci. 2012;1266:124-37.
94. Stuelten CH, Parent CA, Montell DJ. Cell motility in cancer invasion and metastasis: insights from simple model organisms. Nature Reviews Cancer. 2018;18(5):296-312.
95. de Boeck M, Cui C, Mulder AA, Jost CR, Ikeno S, Ten Dijke P. Smad6 determines BMP-regulated invasive behaviour of breast cancer cells in a zebrafish xenograft model. Scientific reports. 2016;6:24968-.
96. Tang Q, Moore JC, Ignatius MS, Tenente IM, Hayes MN, Garcia EG, et al. Imaging tumour cell heterogeneity following cell transplantation into optically clear immune-deficient zebrafish. Nat Commun. 2016;7:10358-.
97. Zhu S, Lee J-S, Guo F, Shin J, Perez-Atayde AR, Kutok JL, et al. Activated ALK collaborates with MYCN in neuroblastoma pathogenesis. Cancer cell. 2012;21(3):362-73.
98. Zhu S, Thomas Look A. Neuroblastoma and Its Zebrafish Model. Advances in experimental medicine and biology. 2016;916:451-78.
99. Delloye-Bourgeois C, Bertin L, Thoinet K, Jarrosson L, Kindbeiter K, Buffet T, et al. Microenvironment-Driven Shift of Cohesion/Detachment Balance within Tumors Induces a Switch toward Metastasis in Neuroblastoma. Cancer Cell. 2017;32(4):427-43.e8.
100. Bailey CM, Morrison JA, Kulesa PM. Melanoma revives an embryonic migration program to promote plasticity and invasion. Pigment Cell Melanoma Res. 2012;25(5):573-83.
101. Pittet MJ, Weissleder R. Intravital imaging. Cell. 2011;147(5):983-91.
102. Ilina O, Campanello L, Gritsenko PG, Vullings M, Wang C, Bult P, et al. Intravital microscopy of collective invasion plasticity in breast cancer. Dis Model Mech. 2018;11(9):dmm034330.
103. Patsialou A, Bravo-Cordero JJ, Wang Y, Entenberg D, Liu H, Clarke M, et al. Intravital multiphoton imaging reveals multicellular streaming as a crucial component of in vivo cell migration in human breast tumors. Intravital. 2013;2(2):e25294-e.
104. Weigelin B, Bakker G-J, Friedl P. Intravital third harmonic generation microscopy of collective melanoma cell invasion. IntraVital. 2012;1(1):32-43.
105. Alieva M, Leidgens V, Riemenschneider MJ, Klein CA, Hau P, van Rheenen J. Intravital imaging of glioma border morphology reveals distinctive cellular dynamics and contribution to tumor cell invasion. Scientific Reports. 2019;9(1):2054.
106. Beerling E, Oosterom I, Voest E, Lolkema M, van Rheenen J. Intravital characterization of tumor cell migration in pancreatic cancer. Intravital. 2016;5(3):e1261773-e.
107. Huang Q, Cohen MA, Alsina FC, Devlin G, Garrett A, McKey J, et al. Intravital imaging of mouse embryos. Science (New York, NY). 2020;368(6487):181-6.
108. Perrin L, Bayarmagnai B, Gligorijevic B. Frontiers in intravital multiphoton microscopy of cancer. CANCER REPORTS. 2020;3(1):e1192.

109. Nguyen-Ngoc KV, Shamir ER, Huebner RJ, Beck JN, Cheung KJ, Ewald AJ. 3D culture assays of murine mammary branching morphogenesis and epithelial invasion. Methods Mol Biol. 2015;1189:135-62.
110. Nguyen-Ngoc KV, Ewald AJ. Mammary ductal elongation and myoepithelial migration are regulated by the composition of the extracellular matrix. J Microsc. 2013;251(3):212-23.
111. Gossen M, Bujard H. Tight control of gene expression in mammalian cells by tetracycline-responsive promoters. Proceedings of the National Academy of Sciences. 1992;89(12):5547-51.
112. Lutz W, Stöhr M, Schürmann J, Wenzel A, Löhr A, Schwab M. Conditional expression of N-myc in human neuroblastoma cells increases expression of alpha-prothymosin and ornithine decarboxylase and accelerates progression into S-phase early after mitogenic stimulation of quiescent cells. Oncogene. 1996;13(4):803-12.
113. Eslami Amirabadi H, SahebAli S, Frimat JP, Luttge R, den Toonder JMJ. A novel method to understand tumor cell invasion: integrating extracellular matrix mimicking layers in microfluidic chips by "selective curing". Biomed Microdevices. 2017;19(4):92-.
114. Kajiho H, Kajiho Y, Frittoli E, Confalonieri S, Bertalot G, Viale G, et al. RAB2A controls MT1-MMP endocytic and E-cadherin polarized Golgi trafficking to promote invasive breast cancer programs. EMBO reports. 2016;17(7):1061-80.
115. Marusyk A, Polyak K. Tumor heterogeneity: causes and consequences. Biochim Biophys Acta. 2010;1805(1):105-17.
116. Shoemaker RH. The NCI60 human tumour cell line anticancer drug screen. Nat Rev Cancer. 2006;6(10):813-23.
117. Gillet JP, Calcagno AM, Varma S, Marino M, Green LJ, Vora MI, et al. Redefining the relevance of established cancer cell lines to the study of mechanisms of clinical anti-cancer drug resistance. Proc Natl Acad Sci U S A. 2011;108(46):18708-13.
118. Gengenbacher N, Singhal M, Augustin HG. Preclinical mouse solid tumour models: status quo, challenges and perspectives. Nature Reviews Cancer. 2017;17(12):751-65.
119. Kamili A, Atkinson C, Trahair TN, Fletcher JI. Mouse models of high-risk neuroblastoma. Cancer Metastasis Rev. 2020:10.1007/s10555-020-09855-0.
120. Hidalgo M, Amant F, Biankin AV, Budinská E, Byrne AT, Caldas C, et al. Patient-derived xenograft models: an emerging platform for translational cancer research. Cancer discovery. 2014;4(9):998-1013.
121. Zhao X, Liu Z, Yu L, Zhang Y, Baxter P, Voicu H, et al. Global gene expression profiling confirms the molecular fidelity of primary tumor-based orthotopic xenograft mouse models of medulloblastoma. Neuro Oncol. 2012;14(5):574-83.
122. Campbell KM, Lin T, Zolkind P, Barnell EK, Skidmore ZL, Winkler AE, et al. Oral Cavity Squamous Cell Carcinoma Xenografts Retain Complex Genotypes and Intertumor Molecular Heterogeneity. Cell Reports. 2018;24(8):2167-78.
123. Hsu C-L, Kuo Y-C, Huang Y, Huang Y-C, Lui K-W, Chang K-P, et al. Application of a patient-derived xenograft model in cytolytic viral activation therapy for nasopharyngeal carcinoma. Oncotarget. 2015;6(31):31323-34.
124. Nunes M, Vrignaud P, Vacher S, Richon S, Lièvre A, Cacheux W, et al. Evaluating patient-derived colorectal cancer xenografts as preclinical models by comparison with patient clinical data. Cancer research. 2015;75(8):1560-6.
125. Baker BM, Chen CS. Deconstructing the third dimension: how 3D culture microenvironments alter cellular cues. Journal of cell science. 2012;125(Pt 13):3015-24.

126. Kapałczyńska M, Kolenda T, Przybyła W, Zajączkowska M, Teresiak A, Filas V, et al. 2D and 3D cell cultures - a comparison of different types of cancer cell cultures. Arch Med Sci. 2018;14(4):910-9.
127. Lutz W, Stohr M, Schurmann J, Wenzel A, Lohr A, Schwab M. Conditional expression of N-myc in human neuroblastoma cells increases expression of alpha-prothymosin and ornithine decarboxylase and accelerates progression into S-phase early after mitogenic stimulation of quiescent cells. Oncogene. 1996;13(4):803-12.
128. Wolf K, Wu YI, Liu Y, Geiger J, Tam E, Overall C, et al. Multi-step pericellular proteolysis controls the transition from individual to collective cancer cell invasion. Nat Cell Biol. 2007;9(8):893-904.
129. Khalil AA, Ilina O, Vasaturo A, Venhuizen J-H, Vullings M, Venhuizen V, et al. Leader cell activity and collective invasion by an autocrine nucleotide loop through connexin-43 hemichannels and ADORA1. bioRxiv. 2019:2019.12.30.888958.
130. Alexander S, Weigelin B, Winkler F, Friedl P. Preclinical intravital microscopy of the tumour-stroma interface: invasion, metastasis, and therapy response. Current Opinion in Cell Biology. 2013;25(5):659-71.
131. Khoja L, Shenjere P, Hodgson C, Hodgetts J, Clack G, Hughes A, et al. Prevalence and heterogeneity of circulating tumour cells in metastatic cutaneous melanoma. Melanoma Research. 2014;24(1).
132. Liu X, Zhang Z, Zhang B, Zheng Y, Zheng C, Liu B, et al. Circulating tumor cells detection in neuroblastoma patients by EpCAM-independent enrichment and immunostaining-fluorescence in situ hybridization. EBioMedicine. 2018;35:244-50.
133. Dwane S, Durack E, Kiely PA. Optimising parameters for the differentiation of SH-SY5Y cells to study cell adhesion and cell migration. BMC Research Notes. 2013;6(1):366.
134. Marler KJM, Kozma R, Ahmed S, Dong J-M, Hall C, Lim L. Outgrowth of neurites from NIE-115 neuroblastoma cells is prevented on repulsive substrates through the action of PAK. Mol Cell Biol. 2005;25(12):5226-41.
135. Gritsenko PG, Atlasy N, Dieteren CEJ, Navis AC, Venhuizen J-H, Veelken C, et al. p120-catenin-dependent collective brain infiltration by glioma cell networks. Nature Cell Biology. 2020;22(1):97-107.
136. Serres E, Debarbieux F, Stanchi F, Maggiorella L, Grall D, Turchi L, et al. Fibronectin expression in glioblastomas promotes cell cohesion, collective invasion of basement membrane in vitro and orthotopic tumor growth in mice. Oncogene. 2014;33(26):3451-62.
137. Fayzullin A, Tuvnes FA, Skjellegrind HK, Behnan J, Mughal AA, Langmoen IA, et al. Time-lapse phenotyping of invasive glioma cells ex vivo reveals subtype-specific movement patterns guided by tumor core signaling. Experimental Cell Research. 2016;349(2):199-213.
138. Zheng Y, Xue X, Resto-Irizarry AM, Li Z, Shao Y, Zheng Y, et al. Dorsal-ventral patterned neural cyst from human pluripotent stem cells in a neurogenic niche. Science Advances. 2019;5(12):eaax5933.
139. Elisha Y, Kalchenko V, Kuznetsov Y, Geiger B. Dual role of E-cadherin in the regulation of invasive collective migration of mammary carcinoma cells. Scientific Reports. 2018;8(1):4986.
140. Brabletz T. To differentiate or not — routes towards metastasis. Nature Reviews Cancer. 2012;12(6):425-36.
141. Kim H, Lin Q, Glazer PM, Yun Z. The hypoxic tumor microenvironment in vivo selects the cancer stem cell fate of breast cancer cells. Breast Cancer Res. 2018;20(1):16-.

142. Stewart JM, Shaw PA, Gedye C, Bernardini MQ, Neel BG, Ailles LE. Phenotypic heterogeneity and instability of human ovarian tumor-initiating cells. Proceedings of the National Academy of Sciences of the United States of America. 2011;108(16):6468-73.
143. Nguyen-Ngoc KV, Cheung KJ, Brenot A, Shamir ER, Gray RS, Hines WC, et al. ECM microenvironment regulates collective migration and local dissemination in normal and malignant mammary epithelium. Proc Natl Acad Sci U S A. 2012;109(39):E2595-604.
144. Puls TJ, Tan X, Whittington CF, Voytik-Harbin SL. 3D collagen fibrillar microstructure guides pancreatic cancer cell phenotype and serves as a critical design parameter for phenotypic models of EMT. PloS one. 2017;12(11):e0188870.
145. Vellinga TT, den Uil S, Rinkes IHB, Marvin D, Ponsioen B, Alvarez-Varela A, et al. Collagen-rich stroma in aggressive colon tumors induces mesenchymal gene expression and tumor cell invasion. Oncogene. 2016;35(40):5263-71.
146. Talbot NC, Caperna TJ. Proteome array identification of bioactive soluble proteins/peptides in Matrigel: relevance to stem cell responses. Cytotechnology. 2015;67(5):873-83.
147. Perris R, Perissinotto D. Role of the extracellular matrix during neural crest cell migration. Mechanisms of Development. 2000;95(1):3-21.
148. Olsson L, Svensson K, Perris R. Effects of extracellular matrix molecules on subepidermal neural crest cell migration in wild type and white mutant (dd) axolotl embryos. Pigment Cell Res. 1996;9(1):18-27.
149. Bilozur ME, Hay ED. Neural crest migration in 3D extracellular matrix utilizes laminin, fibronectin, or collagen. Dev Biol. 1988;125(1):19-33.
150. Tosney KW, Dehnbostel DB, Erickson CA. Neural Crest Cells Prefer the Myotome's Basal Lamina over the Sclerotome as a Substratum. Dev Biol. 1994;163(2):389-406.
151. Flanagan LA, Rebaza LM, Derzic S, Schwartz PH, Monuki ES. Regulation of human neural precursor cells by laminin and integrins. Journal of neuroscience research. 2006;83(5):845-56.
152. Valentijn LJ, Koster J, Zwijnenburg DA, Hasselt NE, van Sluis P, Volckmann R, et al. TERT rearrangements are frequent in neuroblastoma and identify aggressive tumors. Nature Genetics. 2015;47(12):1411-4.
153. Chakrabarti M, Banik NL, Ray SK. Sequential hTERT Knockdown and Apigenin Treatment Inhibited Invasion and Proliferation and Induced Apoptosis in Human Malignant Neuroblastoma SK-N-DZ and SK-N-BE2 Cells. Journal of Molecular Neuroscience. 2013;51(1):187-98.
154. George J, Banik NL, Ray SK. Knockdown of hTERT and concurrent treatment with interferon-gamma inhibited proliferation and invasion of human glioblastoma cell lines. Int J Biochem Cell Biol. 2010;42(7):1164-73.
155. Liu Z, Li Q, Li K, Chen L, Li W, Hou M, et al. Telomerase reverse transcriptase promotes epithelial–mesenchymal transition and stem cell-like traits in cancer cells. Oncogene. 2013;32(36):4203-13.
156. Hu C, Ni Z, Li B-s, Yong X, Yang X, Zhang J-w, et al. hTERT promotes the invasion of gastric cancer cells by enhancing FOXO3a ubiquitination and subsequent ITGB1 upregulation. Gut. 2017;66(1):31.
157. Favrot MC, Combaret V, Goillot E, Lutz P, Frappaz D, Thiesse P, et al. Expression of integrin receptors on 45 clinical neuroblastoma specimens. Int J Cancer. 1991;49(3):347-55.

158. Carmeliet G, Himpens B, Cassiman JJ. Selective increase in the binding of the alpha 1 beta 1 integrin for collagen type IV during neurite outgrowth of human neuroblastoma TR 14 cells. J Cell Sci. 1994;107 (Pt 12):3379-92.
159. Qin Y, Tang B, Hu C-J, Xiao Y-F, Xie R, Yong X, et al. An hTERT/ZEB1 complex directly regulates E-cadherin to promote epithelial-to-mesenchymal transition (EMT) in colorectal cancer. Oncotarget. 2016;7(1):351-61.
160. Caramel J, Papadogeorgakis E, Hill L, Browne Gareth J, Richard G, Wierinckx A, et al. A Switch in the Expression of Embryonic EMT-Inducers Drives the Development of Malignant Melanoma. Cancer Cell. 2013;24(4):466-80.
161. Wu J, Cheng P, Huang Z, Tan Q, Qu Y. Nodal increases the malignancy of childhood neuroblastoma cells via regulation of Zeb1. Biofactors. 2019;45(3):355-63.
162. Horn S, Figl A, Rachakonda PS, Fischer C, Sucker A, Gast A, et al. TERT promoter mutations in familial and sporadic melanoma. Science (New York, NY). 2013;339(6122):959-61.
163. Naidoo K, Malindisa ST, Otgaar TC, Bernert M, Da Costa Dias B, Ferreira E, et al. Knock-Down of the 37kDa/67kDa Laminin Receptor LRP/LR Impedes Telomerase Activity. PloS one. 2015;10(11):e0141618-e.
164. Pugh TJ, Morozova O, Attiyeh EF, Asgharzadeh S, Wei JS, Auclair D, et al. The genetic landscape of high-risk neuroblastoma. Nature Genetics. 2013;45(3):279-84.
165. Trigg RM, Turner SD. ALK in Neuroblastoma: Biological and Therapeutic Implications. Cancers (Basel). 2018;10(4):113.
166. Rokita JL, Rathi KS, Cardenas MF, Upton KA, Jayaseelan J, Cross KL, et al. Genomic profiling of childhood tumor patient-derived xenograft models to enable rational clinical trial design. bioRxiv. 2019:566455.
167. Carpenter EL, Haglund EA, Mace EM, Deng D, Martinez D, Wood AC, et al. Antibody targeting of anaplastic lymphoma kinase induces cytotoxicity of human neuroblastoma. Oncogene. 2012;31(46):4859-67.
168. Berry T, Luther W, Bhatnagar N, Jamin Y, Poon E, Sanda T, et al. The ALK(F1174L) mutation potentiates the oncogenic activity of MYCN in neuroblastoma. Cancer cell. 2012;22(1):117-30.
169. Ueda T, Nakata Y, Yamasaki N, Oda H, Sentani K, Kanai A, et al. ALKR1275Q perturbs extracellular matrix, enhances cell invasion and leads to the development of neuroblastoma in cooperation with MYCN. Oncogene. 2016;35(34):4447-58.
170. Krytska K, Ryles HT, Sano R, Raman P, Infarinato NR, Hansel TD, et al. Crizotinib Synergizes with Chemotherapy in Preclinical Models of Neuroblastoma. Clin Cancer Res. 2016;22(4):948-60.
171. Wang H, Hara Y, Liu X, Reuben JM, Xie Y, Xu H, et al. Detection and enumeration of circulating tumor cells based on their invasive property. Oncotarget. 2015;6(29):27304-11.
172. Tadeo I, Berbegall AP, Castel V, García-Miguel P, Callaghan R, Påhlman S, et al. Extracellular matrix composition defines an ultra-high-risk group of neuroblastoma within the high-risk patient cohort. British Journal of Cancer. 2016;115(4):480-9.
173. Huang M, Weiss WA. Neuroblastoma and MYCN. Cold Spring Harb Perspect Med. 2013;3(10):a014415-a.
174. Goodman LA, Liu BC, Thiele CJ, Schmidt ML, Cohn SL, Yamashiro JM, et al. Modulation of N-myc expression alters the invasiveness of neuroblastoma. Clin Exp Metastasis. 1997;15(2):130-9.

175. Selmi A, de Saint-Jean M, Jallas A-C, Garin E, Hogarty MD, Bénard J, et al. TWIST1 is a direct transcriptional target of MYCN and MYC in neuroblastoma. Cancer Letters. 2015;357(1):412-8.
176. Planells-Ferrer L, Urresti J, Soriano A, Reix S, Murphy DGM, Ferreres JC, et al. MYCN repression of Lifeguard/FAIM2 enhances neuroblastoma aggressiveness. Cell Death & Disease. 2014;5.
177. Shankar V, Hori H, Kihira K, Lei Q, Toyoda H, Iwamoto S, et al. Mesenchymal stromal cell secretome up-regulates 47 kDa CXCR4 expression, and induce invasiveness in neuroblastoma cell lines. PloS one. 2015;10(3):e0120069-e.
178. Fraley SI, Feng Y, Krishnamurthy R, Kim D-H, Celedon A, Longmore GD, et al. A distinctive role for focal adhesion proteins in three-dimensional cell motility. Nature cell biology. 2010;12(6):598-604.
179. Meyer AS, Hughes-Alford SK, Kay JE, Castillo A, Wells A, Gertler FB, et al. 2D protrusion but not motility predicts growth factor-induced cancer cell migration in 3D collagen. J Cell Biol. 2012;197(6):721-9.
180. Curtin C, Nolan JC, Conlon R, Deneweth L, Gallagher C, Tan YJ, et al. A physiologically relevant 3D collagen-based scaffold-neuroblastoma cell system exhibits chemosensitivity similar to orthotopic xenograft models. Acta Biomater. 2018;70:84-97.
181. Fayzullin A, Sandberg CJ, Spreadbury M, Saberniak BM, Grieg Z, Skaga E, et al. Phenotypic and Expressional Heterogeneity in the Invasive Glioma Cells. Translational Oncology. 2019;12(1):122-33.
182. Szabó A, Melchionda M, Nastasi G, Woods ML, Campo S, Perris R, et al. In vivo confinement promotes collective migration of neural crest cells. Journal of Cell Biology. 2016;213(5):543-55.
183. McLennan R, Schumacher LJ, Morrison JA, Teddy JM, Ridenour DA, Box AC, et al. Neural crest migration is driven by a few trailblazer cells with a unique molecular signature narrowly confined to the invasive front. Development. 2015;142(11):2014-25.
184. Richardson J, Gauert A, Briones Montecinos L, Fanlo L, Alhashem Zainalabdeen M, Assar R, et al. Leader Cells Define Directionality of Trunk, but Not Cranial, Neural Crest Cell Migration. Cell Reports. 2016;15(9):2076-88.
185. Thomas LA, Yamada KM. Contact stimulation of cell migration. Journal of Cell Science. 1992;103(4):1211-4.
186. Mitchell CB, O'Neill GM. Rac GTPase regulation of 3D invasion in neuroblastomas lacking MYCN amplification. Cell Adh Migr. 2017;11(1):68-79.
187. Hughes CS, Postovit LM, Lajoie GA. Matrigel: a complex protein mixture required for optimal growth of cell culture. Proteomics. 2010;10(9):1886-90.
188. Attieh Y, Vignjevic DM. The hallmarks of CAFs in cancer invasion. European Journal of Cell Biology. 2016;95(11):493-502.
189. Neri S, Ishii G, Hashimoto H, Kuwata T, Nagai K, Date H, et al. Podoplanin-expressing cancer-associated fibroblasts lead and enhance the local invasion of cancer cells in lung adenocarcinoma. Int J Cancer. 2015;137(4):784-96.
190. Izar B, Joyce CE, Goff S, Cho NL, Shah PM, Sharma G, et al. Bidirectional cross talk between patient-derived melanoma and cancer-associated fibroblasts promotes invasion and proliferation. Pigment Cell Melanoma Res. 2016;29(6):656-68.
191. Puls TJ, Tan X, Husain M, Whittington CF, Fishel ML, Voytik-Harbin SL. Development of a Novel 3D Tumor-tissue Invasion Model for High-throughput, High-content Phenotypic Drug Screening. Scientific Reports. 2018;8(1):13039.

192. Smith HA, Kang Y. The metastasis-promoting roles of tumor-associated immune cells. J Mol Med (Berl). 2013;91(4):411-29.
193. Wei C, Yang C, Wang S, Shi D, Zhang C, Lin X, et al. Crosstalk between cancer cells and tumor associated macrophages is required for mesenchymal circulating tumor cell-mediated colorectal cancer metastasis. Molecular Cancer. 2019;18(1):64.
194. Dwyer AR, Ellies LG, Holme AL, Pixley FJ. A three-dimensional co-culture system to investigate macrophage-dependent tumor cell invasion. J Biol Methods. 2016;3(3):e49-e.